NORTHWESTERN UNIVERSITY

Structure and Thermodynamics of Model Catalytic Oxide Surfaces

A DISSERTATION

SUBMITTED TO THE GRADUATE SCHOOL

IN PARTIAL FULFILLMENT OF THE REQUIREMENTS

for the degree

DOCTOR OF PHILOSOPHY

Field of Materials Science and Engineering

By

Ann Norina Chiaramonti

EVANSTON, ILLINOIS

December 2005

ABSTRACT

Structure and Thermodynamics of Model Catalytic Oxide Surfaces

Ann Norina Chiaramonti

The atomic scale structure of crystalline surfaces plays an important role in the overall properties of materials systems, especially those relating to heterogeneous catalysis, thin film growth, and the increasingly miniaturized world of micro electrical mechanical systems (MEMS). Nanoscale engineering of materials has become commonplace and as technologies begin to emerge on smaller and smaller length scales, surface properties become increasingly more important relative to those of the bulk. Only through knowledge of the surface structure of materials can one truly understand the nature of the processes that play out on them. The research described in this manuscript involves a combination of computational (Direct Methods) and experimental (TEM) methods for the investigation of the surface structure and thermodynamics of two model heterogeneous catalytic oxides, α-Fe_2O_3 (the mineral hematite) and $SrTiO_3$.

A new flux system has been developed for the growth of single crystal α-Fe_2O_3. The effect of ion bombardment and annealing on the (0001) surface of hematite was investigated, and the differences between pure and impure samples are presented. Finally, methodologies are discussed for obtaining the "biphase" surface structure on a TEM-ready sample.

Several new reconstructions were observed on the (111) surface of $SrTiO_3$, including (3x3), ($\frac{9}{5}$x$\frac{9}{5}$), (6x6), and (4x4) unit cells. The structure of the (3x3) surface has been solved and it is proposed that all of the herein observed reconstructions will be scaleable structures from a general motif, with the different unit cell sizes being accommodated by differences in the occupancy of surface sites. The regions of phase stability have been accurately determined for the reconstructions in time, temperature and oxygen partial pressure, and a metastable surface phase diagram has been constructed. A region of metastable three-phase coexistence has been observed over a wide range of temperatures and oxygen partial pressures.

Approved by

Professor Laurence D. Marks

Department of Materials Science and Engineering

Northwestern University, Evanston, IL 60208, USA

Acknowledgements

First I would like to thank my advisors, Professors L.D. Marks and P.C. Stair, for their continuous support, encouragement, and genuine excitement for my work. One of the greatest lessons I learned from my advisors is to know the limits of your own knowledge and seek out the assistance of others when necessary. They have also taught me to think critically and question incessantly, and for that I am grateful. I would especially like to thank LDM for always telling me to, "JUST DO IT!" Had I not, I am certain I would have been here several more years.

I would like to thank the members of my committee, Professor K.R. Poeppelmeier, Professor M.C. Hersam, Professor M. Asta, and Professor M.J. Bedzyk, with whom I have had the pleasure and honor of frequent collaboration. Working with each of them has taught me to think about my research from a different perspective, which has made it more thorough and definitely more interesting. I would especially like to thank KRP, my "surrogate advisor", for encouraging me to think like a chemist. I'm still working on that.

This research project was funded by the EMSI program of the National Science Foundation and the U.S. Department of Energy Office of Basic Science (CHE-9810378) as well as the Chemical Sciences, Geosciences and Biosciences Division of

the Office of Basic Energy Sciences, Office of Science, U.S. Department of Energy (DE-FG02-03ER15457) at the Northwestern University Institute for Environmental Catalysis.

I am indebted to my predecessors, especially Dr. Jason D. Pless, Dr. Natasha Erdman, and Dr. Arun K. Subramanian, for their mentorship and friendship over the years. Withouht their knowledge transfer, I would not know how to use the floating zone furnace, prepare TEM samples, or operate SPEAR. I would also like to thank the past and present members of the Marks and Stair Groups (especially Ian Widlow, Dr. Edy Widjaja, Yingmin Wang, Chris Own, Arno Merkle, Courtney Lanier, Dr. Li Liu, and Jared Smit) for making my time in the lab a truly enjoyable experience. I would like to thank the past and present members of the Poeppelmeier Research Group for opening your lab and your soda pool to me. I would also like to thank two hardworking undergraduates, Jungyun Kim and Wen Tu, for their assistance in preparing some of the many TEM samples of $SrTiO_3$ needed over the course of this study.

I would like to thank the many wonderful people outside of my research group that I have had the pleasure of meeting at Northwestern for their friendship. The Materials Science and Engineering Department is full of interesting and entertaining characters who made taking classes and the drudgery of research day in and day out bearable. I would like to thank my friends Leta Woo and Chris Weyant for being ready to have a good time, any time, during the first year. Thank you Keith Dvorkin and Nelson Nunalee for keeping me entertained at the back of the

class when we should have been listening to the lecture—I have never met two people with such biting wit and great comedic timing. I would finally like to thank my lunch buddies, neighbors, and friends Duane Goodner and Stephan Gerstl for always being ready and willing to sit way too long at Garrett when we should have been doing other things.

I have to thank my wonderful parents, who have actively encouraged my scientific endeavors in all of their strange manifestations, from when I built a 6' high model of saturn and its rings, to when I decided to be a materials scientist and they had no idea what that meant, or if it would ever lead to a real job. Having a curious, mechanically inclined father and a strong willed, independent mother shaped who I am as a person and as a scientist. Thank you Dad for always wanting to hear about excited electrons and thank you Mom for teaching me how to explain an Angstrom to the lay person (yes, it really is that thin). I would also like to thank my two sisters, Victoria and Laura, for never letting me forget that there are still a lot of things I dont know much about.

I want to thank my husband John, for keeping me sane the past 5 years, for telling me that I *was* smart enough to do this, for encouraging me to embrace Unix, for making me laugh when I was discouraged, for keeping me from blowing every setback out of proportion, and for driving me to campus all those late nights and weekends to turn off the furnaces. Your encouragement and love has enabled me to persevere this sometimes difficult experience. Thank you from the bottom of my heart.

Finally, and most importantly, I must thank *National Geographic* magazine for their 1989 article entitled, "Advanced Materials–Reshaping our Lives," which captivated a 12 year old girl enough to declare, in the 7^{th} grade, that she would pursue materials science as a career.

Contents

List of Tables

List of Figures

CHAPTER 1

Introduction

The atomic scale structures of crystalline surfaces play an important role in the overall properties of materials systems, especially those relating to heterogeneous catalysis, thin film growth, and the increasingly miniaturized world of micro electrical mechanical systems (MEMS). Nanoscale engineering of materials has become commonplace and as technologies begin to emerge on smaller and smaller length scales, surface properties become increasingly more important relative to those of the bulk. The loss of coordination at the surface and the so-called dangling bonds that result increase the surface free energy and provide a driving force for the reconstruction of surfaces whose structure can not be predicted from bulk thermodynamic arguments. This inability to predict the structure of surfaces *a priori* has necessitated a field of study devoted entirely to experimentally determining the surface atomic structure of materials. Only through the complete knowledge of the surface structure of materials can one truly understand the nature of the processes that play out on them.

The most common techniques for studying the atomic scale crystal structure of surfaces in real space include scanning tunneling microscopy (STM), transmission electron microscopy (TEM) including high-resolution electron microscopy

(HREM), and scanning transmission electron microscopy (STEM). Several common reciprocal space techniques include low-energy electron diffraction (LEED), grazing incidence X-ray diffraction (GIXD), transmission electron diffraction (TED), and reflection high-energy electron diffraction (RHEED). Excellent comparative reviews of the above techniques have been written by Venables et al. (1987) and Cowley (1986), and reviews of their specific application to surface crystallography can be found in works by Jayaram et al. (1995) and Subramanian and Marks (2004a). Of the above-mentioned methods, high-voltage transmission electron microscopy methods (TEM, TED, HREM) have proven indispensable to the surface crystallographer as they allow for the capture of both real and reciprocal space crystallographic information from a single area of the specimen, nearly instantaneously, at sub-atomic scale resolution. Parallel data capture can lead to real-time investigation of surface phenomena and recently, these techniques have been used to extract not only surface atomic positions but also the surface charge density (Subramanian and Marks, 2004b). With the recent advent of so-called environmental cells (Boyes and Gai, 1997; Sharma, 2001) and aberration corrected TEMs (Haider et al., 1998), this technique has proven to be even more useful in the study of surfaces.

For the present work, we have chosen to employ primarily TEM-based techniques along with several complimentary techniques such as XPS, AFM, and ICP-MS in order to study the surface atomic structure of several model catalytic oxides

for the oxidation of simple organic compounds. The catalytic oxidation of hydrocarbons is a particularly interesting area of catalysis in that understanding this one type of reaction can reduce the environmental impact (solid, aerosol, and aqueous pollutants, energy consumption) of a broad range of industrial activities ranging from raw chemical production to energy generation from fossil fuels. When it is considered that the chemical industry in the U.S. alone produces over 100 million tons of chemical by-product waste a year (Rudd et al., 1981), the importance of this type of investigation cannot be understated.

A recent study by Jacobs and Somorjai (1998) points out that, "one of the central issues in catalysis is what determines a catalyst's surface structure and how this effects the reaction." Heterogeneous catalysis is site-specific and structurally dependent. Since the surface of a crystal is the stage on which the heterogeneous catalytic reaction occurs, understanding how the surface atomic structure, bonding, and redox properties of catalytic materials change as a function of reaction conditions is a fundamental unknown. In the case of metals, much headway has been made in understanding their surface atomic structure and this knowledge far surpasses what is known of oxide surfaces (Weiss and Schlögl, 2000).

Unfortunately, the understanding and study of the surface atomic structure of real-world oxide catalysts is a daunting problem complicated by several factors. One is that real catalysts are typically high surface area powders that are often used at high pressures, where the actual active crystallographic surface(s) and sites are largely unknown. For example, Bozso et al. (1977) found that the rate-limiting

step in ammonia synthesis varied over two orders of magnitude on the three low index faces ((001), (110), and (111)) of iron. Further complications arise because heterogeneous catalysts are often transition metal oxides whose cations can change valence and coordination under different conditions of atmosphere, temperature, and pressure. In addition, chemical reactions are dynamic processes and the transient states that exist during the catalytic cycle are difficult to probe experimentally. Finally, it is known that the mere presence of an adsorbate species can alter the surface atomic structure in some cases (Jacobs and Somorjai, 1998). Therefore, in order to make meaningful inroads into the surface structure/reactivity relationship, simplified model systems must be used in order to elucidate the factors which control activity and selectivity at the atomic scale. Practically, this means using high quality single crystals of a specific crystallographic orientation (face) reacted with very simple alkanes (methane, ethane, and propane, for example).

The scope of the current study is exactly that: to elucidate the surface structure of several simple model catalytic oxides, and attempt to correlate the structure to the reactivity observed in these systems. Our approach is to create surface reconstructions on different low-index faces of model oxides by high temperature annealing treatments in which the time, temperature, and atmosphere is varied. Once surface reconstructions are formed, they will be characterized using transmission electron microscopy (including imaging, diffraction, and high resolution imaging) combined with direct methods and various spectroscopic techniques. The goal is the following: to understand how oxide surfaces behave as chemical entities and to

be able to correlate the surface structures to observed patterns in reactivity. For example, it was recently discovered that the Fe_3O_4 terminated (0001) surface of α-Fe_2O_3 was active for methyl radical chemistry, while the so-called "biphase" and bulk terminated surfaces were not (Liu, 2005).

Two model heterogeneous catalysts will be discussed in the present work, α-Fe_2O_3 (the mineral hematite), and $SrTiO_3$, a prototypical perovskite. Hematite makes a good model system for heterogeneous catalysis studies because it is a simple oxide containing only one metal cation together with oxygen. Because iron can adopt one of several oxidation states (0^+, 2^+, and 3^+), it is an excellent candidate for redox chemistry and is known to be active in several catalytic reactions (see Chapter 3 for more details and specific examples). α-Fe_2O_3 has the corundum structure, which consists of a hexagonally close packed array of oxygen with Fe^{3+} filling $\frac{2}{3}$ of the octahedral sites. Hematite is isostructural with several other important corundum structure materials such as Al_2O_3 (alumina or sapphire), V_2O_3, Cr_2O_3, and $FeTiO_3$ (ilmenite). Some of those are catalytically active themselves, while others are used as a substrate for supported precious metal nanoparticle catalysts.

$SrTiO_3$ is an excellent candidate for model catalytic studies because it is a prototypical representative of a wide class of materials with ABO_3 stoichiometry known as perovskites, where the A site cation is typically an alkali or alkaline earth and the B-site cation is typically a transition metal (mixed fluorides such as $KZnF_3$ and $KNiF_3$ also adopt the perovskite structure). The perovskite structure

consists of a simple cubic lattice of the A-site cation with the B-site cation in the body center and oxygen at the face centers forming an octahedron in the unit cell center. Perovskites, and the related structure A_2BO_4, are representative of a wide class of materials whose bulk properties are extremely well characterized and where large databases of both chemical and physical properties exist. Perovskites are fascinating materials whose stoichiometry, valency, and B-site cation can all be varied while maintaining essentially the same structure. In addition, perovskites are perhaps the simplest example of a mixed-metal oxide, which are of particular interest in redox chemistry. Finally, and importantly, it is very easy to obtain large, high purity, high quality single crystals of $SrTiO_3$ which are needed for the present type of study.

The following chapters of this work will describe in detail the experimental equipment, processes, and parameters used (Chapter 2), and will discuss the results obtained in the study of α-$Fe_2O_3(0001)$ (Chapter 3) and $SrTiO_3(111)$ (Chapter 4). It will conclude with a summary and suggestions for future work (Chapter 5).

CHAPTER 2

Experimental Procedures, Techniques, and Specialized Equipment

This chapter will outline in detail the experimental techniques and procedures used in the present study, with particular focus on sample preparation methodologies unique to TEM observations of surfaces. This research utilized a host of techniques including transmission electron microscopy, electron diffraction, Direct Methods, X-ray photoelectron spectroscopy, inductively coupled plasma mass spectrometry (ICP), and X-ray florescence (XRF). It also made use of several pieces of specialized equipment including an optical floating zone furnace in the traveling solvent zone configuration as well as the Hitachi UHV-H9000 high resolution electron microscope and a UHV gas-treatment cell which are part of the in situ Sample Preparation Evaluation Analysis and Reaction (SPEAR) system.

2.1. TEM Methods

2.1.1. Sample Preparation

Standard TEM sample preparation methodologies were employed for both systems in this study, however particular care must be taken to ensure that every stage is

performed without introducing any foreign species into the system. This is particularly true of any contaminant species which could potentially act as an adatom on the surface of interest. High purity single crystals of $SrTiO_3(111)$ were purchased from MTI Corporation (99.9% pure) as 10 mm $\times$ 10 mm $\times$ 0.5 mm wafers EPI polished on one side. Single crystalline (0001) oriented α-Fe_2O_3 hematite substrates were obtained from various sources. Blocky massive mineralogical samples with naturally occurring specular faces (origin China, Brazil, Africa, and Russia) were obtained from Commercial Crystal Laboratories, Inc., Naples, Florida. The samples were purchased as 10 mm $\times$ 10 mm $\times$ 0.5 mm (0001) wafers polished on one side. Mineralogical "iron rose" samples (hereafter referred to as rosettes), which exist naturally as thin (0001) oriented platelets, were obtained from Ouro Preto Minas Gerias, Brazil. Synthetic hematite crystals were grown (see Chapter 3) using the optical floating zone furnace in the traveling solvent zone configuration (Chiaramonti et al., 2004) and were sliced into thin circular (0001) wafers measuring approximately 5 mm $\times$ 0.5 mm.

Standard TEM size 3mm discs were cut from the aforementioned wafers using a circular disc cutter (South Bay Technology Inc.). The discs were then mechanically thinned to approximately 100 μm using 600 grit SiC paper and then mechanically dimpled, leaving the center of the sample approximately 10 μm thick. To avoid contamination from oily residues, only water-based grinding and polishing slurries were used (e.g. water-based diamond and alumina). The commercially available water-based colloidal silica polishing media known as Syton was not used as it

has a tenancy to dry and leave a siliceous residue which is not easily removed. All samples were thoroughly cleaned with an ultrasonic cleaner following the mechanical thinning steps to remove any remaining residues. The discs were thinned to electron transparency using a Gatan Precision Ion Polishing System (PIPS) which uses 5 keV Ar^+ ions at angles of incidence in the range of 80-85 degrees *from the surface normal*.

Following ion bombardment, the surfaces and near-surface regions of the samples are non-stoichiometric, oxygen deficient, amorphous or severely disordered, under stress, and contain a wide variety of bulk defects. The extent to which these effects are manifested depends on the exact material under consideration. For example, after ion bombardment $SrTiO_3(111)$ diffraction patterns (Figure 2.1) very clearly show a diffuse ring denoting the presence of a relatively thick amorphous layer, while α-$Fe_2O_3(0001)$ patterns (Figure 2.2) show no diffuse ring and in fact in some cases (i.e. for impure samples) can actually have an ordered phase (Figure 2.3) at the near surface following Ar^+ bombardment. Nevertheless, for both of the systems investigated in this study, following ion bombardment the samples are under stress and show characteristic bend contours (extinction contrast) in the bright field images (Figure 2.4).

To reverse the damage inflicted from the ion beam source, restore surface stoichiometry, and obtain a flat reconstructed surface for observation, the oxide samples should be annealed *in the proper chemical potential of oxygen* at 0.3-0.5 T_m in

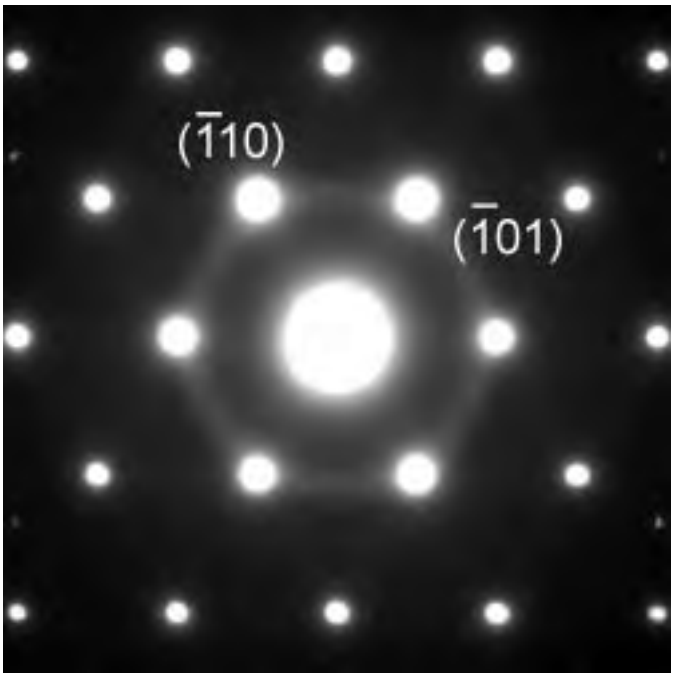

Figure 2.1. Diffraction pattern from $SrTiO_3(111)$ following Ar^+ ion bombardment. A diffuse ring can be seen around the {110} spots indicating disorder.

order to induce surface but limit bulk diffusion (this is in order to prevent coarsening which limits the usefulness of the sample for quantized diffraction and HREM study). This is typically done in a tube furnace (or in the high pressure cell of the gas treatment cell in SPEAR) and the soak time at the maximum temperature will vary depending on the specimen, its initial thickness, and the extent of the ion beam damage. For all of the samples examined in this study, the ramp –up and –down rates were kept constant at 5° per minute and 8° per minute, respectively, in order to prevent thermal shock to both the sample and the alumina furnace

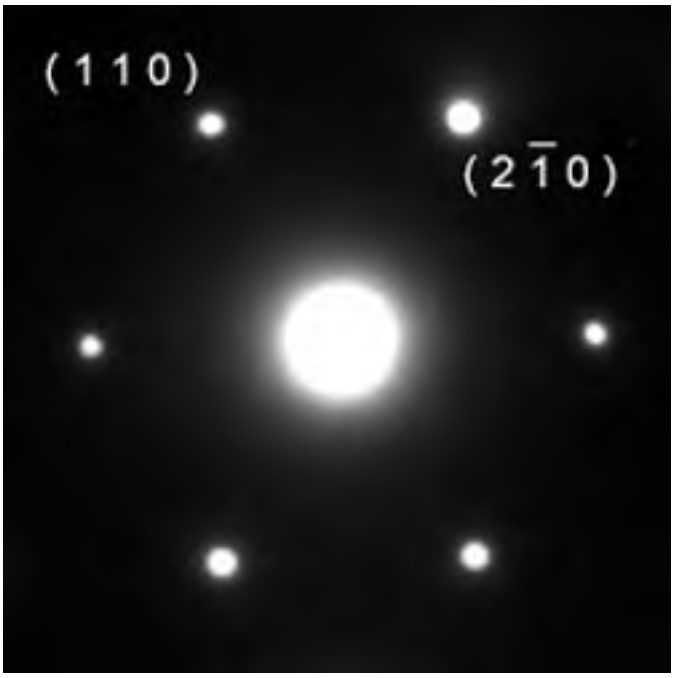

Figure 2.2. Diffraction pattern from a 100% pure sample of α-Fe_2O_3(0001) following Ar^+ ion bombardment.

components. In the case of $SrTiO_3$(111) crystals (T_m >2000 °C) the useful temperature range was between 850 and 1150 °C. Soak times varied from 30 minutes to 10 hours, however 5 hours was found to recover ion beam damage and lead to ordered reproducible surface structures. In the case of α-Fe_2O_3 (T_m in air ∼1500 °C), the useful temperature range is lower and varied from 800-900 °C and the soak time was never longer than two and a half hours to prevent significant coarsening and loss of thin region.

For the present work, a Carbolite STF 15/51/180 tube furnace with a maximum operating temperature of 1500 °C was used. The sample specimens are placed

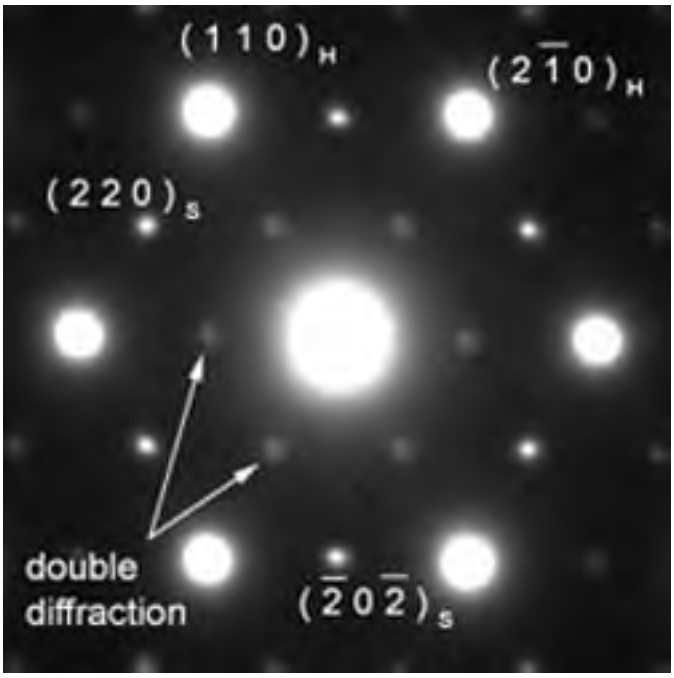

Figure 2.3. Diffraction pattern from mineralogical α-Fe_2O_3(0001) following Ar^+ ion bombardment.

inside of an alumina combustion boat which is then placed inside of a clean quartz tube which is then placed inside of the alumina furnace tube. The quartz tube can be sealed at each end and attached to a high purity gas tank, regulator, and flow meter which are used to regulate the partial pressure (typically of oxygen in the range of 10-100%) during annealing. In some cases, the tubes were left open and exposed to ambient air.

At this point it is useful to elaborate on the cleanliness issues that are encountered when preparing TEM samples of oxides for surface study. In order to minimize foreign specie contamination of the samples (including carbon as well as

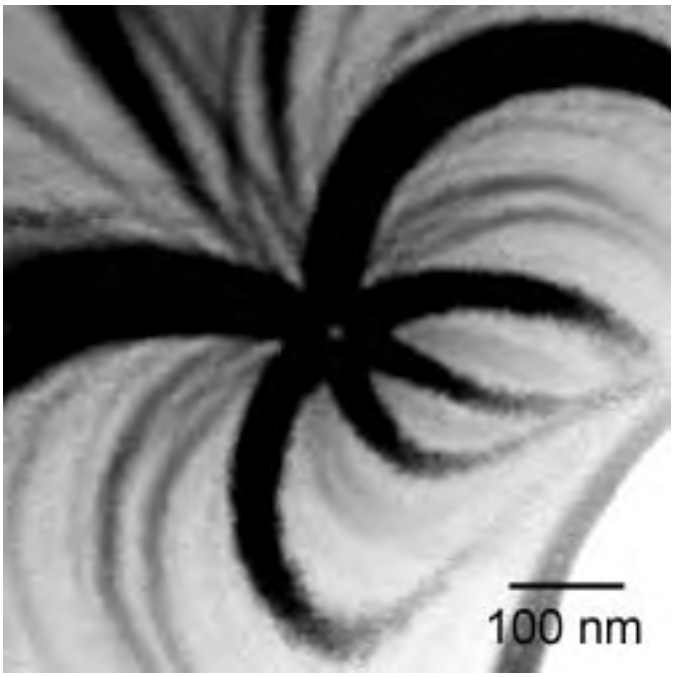

Figure 2.4. Bright field TEM image of the (111) surface of ion milled $SrTiO_3$ showing bend countours (stress). The images for hematite look very similar and show the same type of contrast.

alkaline earths and transition metals) everything that the sample comes into contact with must be kept *pristinely* clean. For the current work, treating the samples as if they were going to be used in both a UHV chamber and Class One clean room was found to be a useful mental exercise. In other words, the tweezers and boxes used to store the sample should be clean, dust free, and lined with a lint-free cloth or aluminum foil. The combustion boat and quartz tube that the samples are annealed in should be cleaned regularly with *aqua regia* (HCl + HNO_3), washed thoroughly with deionized water, and dried using acetone and methanol. Following this cleaning step, the carbonaceous residue should be burned out of the boat and

tube by a cleaning-anneal at 300 °C for one hour prior to use. In this study, separate tubes were used for each material investigated to prevent cross-contamination. Brand new powder-free latex gloves should be worn at all times when handling the sample or anything it comes in contact with. Even breathing on the sample should be minimized because carbonaceous residue can build up and hinder TEM imaging even for reconstructions which are air stable for long periods of time.

2.1.2. Extracting Surface Information from the TEM

When one thinks about experimental techniques for investigating surfaces, TEM is not the first thing to come to mind. In fact, for many years many traditional surface scientists did not even consider TEM a viable technique because by far the majority of all this work had been (and continues to be) performed to investigate bulk materials properties. The fact is, TEM is inherently surface sensitive and both experimental (Xu et al., 1994) and computational (Landree et al. 1997; Marks et al., 1998) methods have been developed that have proven quite robust for extracting useful information from the typically weak surface signal. Historically, the first true application of UHV TEM to surface studies was the investigation of the anomalous superstructure on (111)Au and Pd nucleus formation on (111)Ag surfaces by Yagi et al. (1979). Rather famously, TEM (TED) was used by Takayanagi et al. to solve the Si(111)-7x7 DAS surface structure and end the long dispute which existed among surface scientists (Takayanagi et al., 1985a, 1985b). Since the first forays into determining surface structure via TEM methods, many

systems have been investigated including semiconductors (Collazo-Davila et al., 1997), metals on semiconductors (Grozea et al., 1998; Marks and Plass, 1995), and oxides (Erdman et al., 2002; Subramanian and Marks, 2004b).

In the TEM, a wide variety of techniques exist from which a host of properties can be explored. Surface morphology, surface unit cell dimension, surface atomic positions, and finally near-surface valence charge density can all be obtained from a transmission electron microscope experiment.

Determination of surface morphology is a relatively simple experiment. In fact, this type of experiment was one of the first investigations of surfaces via TEM when Cherns (1974) looked at atomic-level steps on the (111) surface of gold. The standard low-resolution TEM diffraction contrast imaging modes (BF/DF) in plan-view can be employed with great success, revealing surface step bunching, terrace formation, and faceting. Indeed, these modes can also reveal the condition and quality of the surface being investigated, as one can easily distinguish defects such as dislocations, voids, and bending in the sample foil.

If higher resolution is needed, weak-beam darkfield and phase contrast (HREM) techniques can be used to effectively image surface topography. In the weak beam method, images are formed using a first order reflection while the bright Kikuchi line lies outside of the third order reflection (Edington, 1974) and have higher resolution than conventional DF imaging. Lehmpfuhl and Warble (1986) used this technique to image atomic surface steps on the surface of MgO platelets with great success. Focus-dependent phase contrast (HREM) imaging is also useful for

imaging surface morphology, where atomic level steps can also be readily distinguished. Surface contrast can be enhanced by tilting the sample off-zone, as first demonstrated experimentally by J.P. Zhang (1989) on the (111) surface of gold and further corroborated with experiment and simulation of the (111) surface of Si (Marks et al., 1992).

Like LEED, transmission electron diffraction can easily be used in order to determine the surface unit cell dimensions. Again, this is a relatively simple experiment in which a reasonably thin specimen is examined using either standard selected-area diffraction (SAD) or even focused probe diffraction. Due to dynamical effects when the specimen is aligned along a crystallographic zone axis, often in order to record the relatively weak surface spots, the specimen must be tilted far off the zone axis to a more kinematical diffraction condition, as Takayanagi did to resolve the Si(111)-7x7 spots. This benefits the extraction of surface crystallographic information in two ways. First, due to the truncation of bulk rel-rods in reciprocal space (Xu et al., 1993), tilting off zone results in an increase in the intensity of the surface signal relative to that of the bulk. When it is considered that surface signals are typically on the order of 10^4 weaker (Xu and Marks, 1992) than bulk signals, any enhancement is beneficial. Second, tilting off the zone axis reduces dynamical effects which can complicate the quantitative analysis of diffraction patterns for phase recovery via direct methods, which work best in the kinematical approximation (Giacovazzo, 1998).

Knowledge of the surface unit cell dimensions is the first step in determining the surface atom positions. This is accomplished with a combination of surface diffraction analysis (Section 2.1.4) and Direct Methods (Section 2.1.5), which are often augmented by HREM, DF imaging, and associated spectroscopic techniques such as Auger electron spectroscopy and XPS.

Very recently the TEM has proven itself, yet again, as a novel surface technique when Subramanian and Marks (2004b) were able to *experimentally* refine valence charge density from TED data in order to extract the surface charge density of the MgO(111)-$\sqrt{3}$ x $\sqrt{3}$ R30° reconstruction . This represents the first time that valence charge density has been determined experimentally from TED data, and the results agree well with empirical bond-valence estimations.

2.1.3. Surface Imaging Modes

Most reviews on the subject classify imaging into one of two modes based on the orientation of the sample relative to the electron beam. In the interest of consistency the same will be done here.

Plan-view imaging is the name of the technique when samples are viewed parallel to the surface normal direction, the transmitted beam having interacted with the entirety of the sample. Surface information is relatively easy to obtain (and interpret) in this configuration, and all standard imaging modes including bright-field (BF), dark-field (DF), and HREM can be used. When viewing surfaces in conventional HREM mode, whether on or tilted off zone, the bulk lattice constant

dominates the contrast, top-bottom effects occur, and image processing is required. However, after careful processing surface structure can be often resolved with great detail. In fact, the dimers in the third layer of the Si(111)-7x7 DAS structure have been resolved using conventional HREM in plan-view mode (Bengu et al., 1996).

High-resolution DF mode, in which an image is formed by putting a small objective aperture around a set of bulk-forbidden diffracted beams, is useful for obtaining information about surface domain and terrace structure.

Profile imaging is the name given to the technique of viewing atomic columns parallel to the surface of interest, or side-on. First used to study the Au(110)-2x1 surface (Marks, 1983) and small particles (Marks and Smith, 1983), this technique has been successfully extended to semiconductors (Lu and Smith, 1991; Mishima and Osaka, 1998), and superconductors (Zhou et al., 2000). Imaging in this mode must be done carefully, as the surfaces under observation may not be thermodynamically equilibrated or representative of extended two-dimensional structures. In addition, Fresnel effects can complicate interpretation and the proper conditions of defocus are required (Marks, 1984). If these drawbacks are understood, however, this mode is extremely useful as it is a way to get 3-dimensional information (relaxations along the surface normal) from a TEM experiment.

In this work, the Hitachi H-8100 200 keV W filament machine in the Electron Probe Instrumentation Center (EPIC) and the Hitachi UHV-H9000 300 keV LaB_6 filament microscopes were used for imaging.

2.1.4. Surface Diffraction Analysis

Selected area (SA) diffraction using a small aperture in the first image plane below the objective lens has severe limitations when it comes to quantifying a diffraction pattern for intensity analysis. In this mode, regions outside of the aperture may actually contribute to the image due to microscope imperfections such as spherical aberration of the objective lens (Hirsch et al., 1977) as well as user error, where the objective lens is not focused on the specimen plane (Williams and Carter, 1996). In contrast, focused probe (or microdiffraction) is a more accurate way of obtaining diffraction information from a small volume of the specimen, because it limits erroneous contributions from adjacent areas as well as minimizes the diffuse scattering background signal near the zero-order beam. In this mode, a smaller diffraction probe is formed using a small condenser aperture combined with a small probe size.

A series of negatives with exposure times varying between 0.5 and 120 s were recorded for a particular $SrTiO_3$ reconstruction in the UHV-H9000 electron microscope at Northwestern University (Collazo-Davila et. al., 1995) operated at 300 keV. An exposure series is required in order to record the full dynamic range present in surface diffraction patterns, since the intensity of these spots span a range of 2-4 orders of magnitude (Xu and Marks, 1992). In the case of $SrTiO_3$(111), the low radiation fluxes used in the diffraction experiment (as compared to the high fluxes typical of a high resolution experiment) did not appear to damage the specimen

over the time used to record the images, however as a precaution the negatives were not recorded in order of increasing exposure time but were varied in series. Diffraction patterns thus acquired were digitized to 8 bits at 25 μm per pixel using an Optronics P-1000 microdensitometer. Under the exposure conditions used, the intensity readout from the microdensitometer is linearly proportional to the true intensity of the diffraction spots. These intensities were then measured for each negative in turn using a cross-correlation technique (Xu et al., 1994) implemented within the SEMPER image processing language. The measurements from the exposure series were then reduced (collated) to yield a single list of intensity and error for every measured spot. This list is then symmetry averaged to yield a list of symmetry independent beams, their intensity, and their measurement errors.

2.1.5. Direct Methods

Although real space high resolution imaging provides information at the atomic scale, for surfaces the signals are poor and this method is rarely sufficient to solve a structure alone. A more reliable and robust method of obtaining the surface structure information is found in a set of techniques for diffraction phase recovery called direct methods (DM). In a diffraction experiment, the phases of the diffracted beams are lost since only the intensity, or $|F|^2$, can be measured. This is known as the "phase problem" in crystallography, and is a fundamental tenet of diffraction. If both the phases and amplitude (or the square root of the measured intensity) of diffracted beams were known, then the structure factor would be

completely described and a simple Fourier inversion of the data would yield a scattering potential map. It is *only* with the combination of both phase and amplitude information that the data can be inverted and a scattering map obtained.

A full-blown theoretical explanation of electron DM techniques for surfaces is beyond the scope of this work, however a brief overview will be given here. Starting out with a TED pattern, the intensities of the surface diffraction spots can be measured easily and consistently (see section 2.1.4 above). DM serve to approximate the missing phases by exploiting a-priori probability relationships which must exist when scattering comes from atom-like features. Together with the measured amplitude, these approximated (recovered) phases can be used to create maps of the scattering potential (charge density for X-rays and electrostatic potential for electrons). The a-priori relationships make no assumption of the scattering potential but only insist in various ways that it must come from atom-like features, must be positive, and finally must be localized to the near-surface region. These methods have proven extremely powerful and the list of surface structures solved using DM is quite extensive.

In the case of the $SrTiO_3(111)$ surface reconstructions, however, this technique was useful in identifying only part of the structure due to the limitation in surface diffraction analysis that not all beams can be measured. Those which overlap with bulk spots, or those which have contribution from more than one domain are two examples. In this case, the structure completion (refinement) was performed using various techniques including Fourier-difference methods and projection-based

methods (Cowley, 1986) within the Peaks2D refinement code implementation. The structure determined from this step can be further refined using a conventional R-factor or χ^2-type goodness of fit measure, in this case defined as:

$$R = \Sigma|I_{meas}I_{calc}|/\Sigma I_{meas} \tag{2.1}$$

$$\chi^2 = 1/(N-M)\Sigma((I_{meas} - I_{calc})/\sigma)^2 \tag{2.2}$$

where I_{calc} is the calculated intensity, I_{meas} is the measured intensity, N the number of data points, M the number of variable parameters in the refinement, and σ the measurement error.

2.2. Supplementary Characterization Techniques

Two supplementary characterization techniques were regularly employed in the present study and are mainly chemical in nature, aimed at investigating the purity of TEM bulk samples.

2.2.1. Inductively Coupled Plasma Spectroscopy

Inductively coupled plasma atomic emission spectroscopy (ICP-AES) is used for elemental analysis of most metals, sulfur, and phosphorus to concentrations in the ppb level (Payling, 2003). In this destructive technique, the specimen of interest is dissolved in a suitable solvent (acid) and a peristaltic pump delivers a constant

flow of analyte liquid to a nebulizer. The nebulizer turns the liquid into a fine mist which is then carried via inert gas (Ar) into an RF generated IC plasma. Once in the plasma, atoms are excited into both atomic and ionic states, which provide for a rich variety of spectra. The intensity of the characteristic lines, when compared with calibrated standards, give a very accurate measure of impurity concentrations in the prepared samples. Because the type of species to be examined must be known a-priori, ICP-AES is not a useful survey technique (like X-ray fluorescence, see below) but is quite well suited to give very accurate quantitative information once the specific impurity species present are known to an approximate degree.

For the present work, a Thermo Jarrell Ash Atomscan 25 Sequential ICP Spectrometer was used in the Analytical Services Lab of the Department of Chemistry. This machine is equipped with vacuum optics and can cover a spectral range between 160 and 850 nm. ICP-AES was used to determine the ratio of Ca:Fe in synthetic α-Fe_2O_3 crystals grown via the optical floating zone technique as well as to determine the numerical purity of mineralogical specimen of known impurity species determined via other methods.

2.2.2. X-ray Fluorescence

X-ray fluorescence (XRF) is a non-destructive technique and is useful in performing survey scans in order to determine quantitatively which contaminant species may be present in a bulk sample. The detection limit is approximately 0.1% and the depth analyzed is less than 0.1 mm. In this work, un-calibrated bulk standards were

used, sodium concentrations were neglected, samples were analyzed for oxides only, and concentrations were normalized to 100 percent. In this case, the observations are only semi-quantitative, but give a quick, rough, and useful estimate of the impurity species present and their approximate concentration.

In an XRF experiment, a bulk sample is irradiated by a primary X-ray source. When the incident photon is absorbed (rather than scattered), and an inner-shell electron (photoelectron) is ejected, another inner-shell electron falls in to fill the vacancy left by the ejected photoelectron. During this decay, a characteristic photon is emitted in a process called fluorescence, and its energy can be analyzed to identify the element from which it originated. Since the fluorescence spectra from each element are unique, this serves to identify the atomic species present. Their relative amounts can be determined from an analysis of peak intensities.

In the present work, a Bruker S4 Explorer X-ray spectrometer (in the J.B. Cohen Diffraction Facility) was used in order to identify the contaminant species and their approximate amounts in mineralogical α-Fe_2O_3 samples.

2.3. SPEAR System

The Sample Preparation Evaluation Analysis and Reaction (SPEAR) system is an integrated sample introduction, transfer, treatment, and analysis system operated in UHV conditions. The cornerstone of the entire system is the Hitachi UHV-H9000 300 kV LaB_6 thermal emission high resolution transmission electron microscope. This microscope is based on a traditional Hitachi H-9000 instrument

but has been redesigned to be fully UHV compatible and bakeable to 200 °C. It is interfaced via UHV sample transfer to several other components. Currently, there are four side chambers and these include the (1) load lock, (2) SINBAD, (3) analytical chamber, and (4) gas treatment cell.

The load lock is used for sample introduction and removal into the system. It has a gate valve separating it from the rest of SPEAR so that the entire chamber does not have to be baked each time samples come in or out. SINBAD is a chamber used for quasicrystalline thin film growth and contains a DC magnetron sputtering system. The analytical chamber contains a Perkin-Elmer dual-anode X-ray source and PHI spherical capacitance energy analyzer for performing XPS studies, a PHI duoplasmatron microbeam ion source, a Kimball Physics LaB_6 electron gun, a FEI schottky field-emission scanning electron gun, and a secondary electron detector (Channeltron).

The gas treatment cell (McAllister Technical Services, Coeur dAlene, Idaho) is a sample treatment chamber integrated into the SPEAR system for in situ preparation and treatment of TEM samples of oxides and other catalytic materials (Figure 2.5). The gas cell has capability for annealing samples in pressures ranging from UHV (main chamber) to 1 atm (high pressure cell). Currently the cell is equipped with two specimen heaters: a pBN heater capable of reaching temperatures of 600 °C in 1 atm of oxygen, and a non-reactive high purity alumina heater (Heave-Wave Labs, Watsonville, California) capable of reaching temperatures of 1200 °C in nearly any atmosphere. Reactant gasses can be backfilled into the chamber,

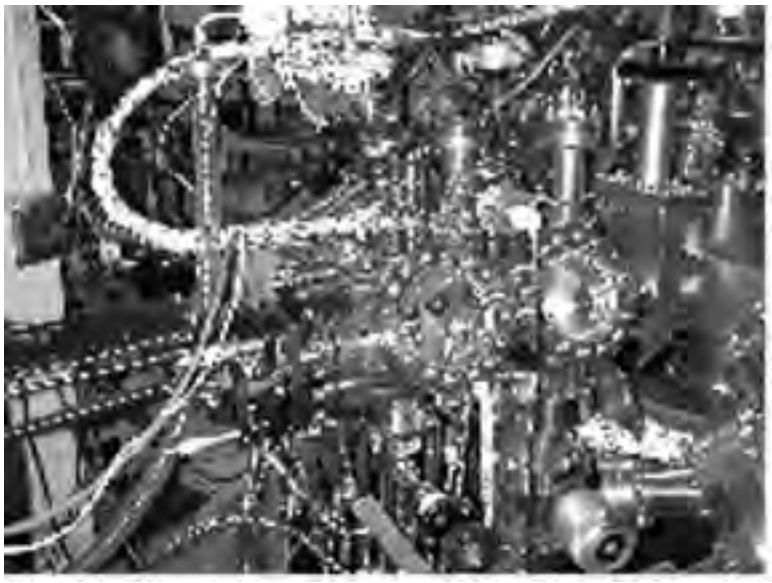

Figure 2.5. The gas treatment cell component of the SPEAR system for in situ treatment of oxides and other environmentally sensitive materials.

and currently the system is equipped with O_2, N_2, and forming gas (7% H_2 balance N_2) sources. The chamber also contains an innovative sapphire-tube-based thermal cracker (courtesy of Professor Peter C. Stair), which can be used to dose samples with a highly focused stream of atomic oxygen or methyl radical (from thermal cracking of nitrous oxide and azomethane, respectively).

2.4. Optical Floating Zone Furnace

Single crystal growth of α-Fe_2O_3 was carried out in a Crystal Systems, Inc. (Japan) optical image furnace (Figure 2.6) in the traveling solvent zone configuration (model number CSI FZ-T-10000-H-VI-VP). Optical floating zone growth is a unique process by which single crystals are nucleated from a molten zone

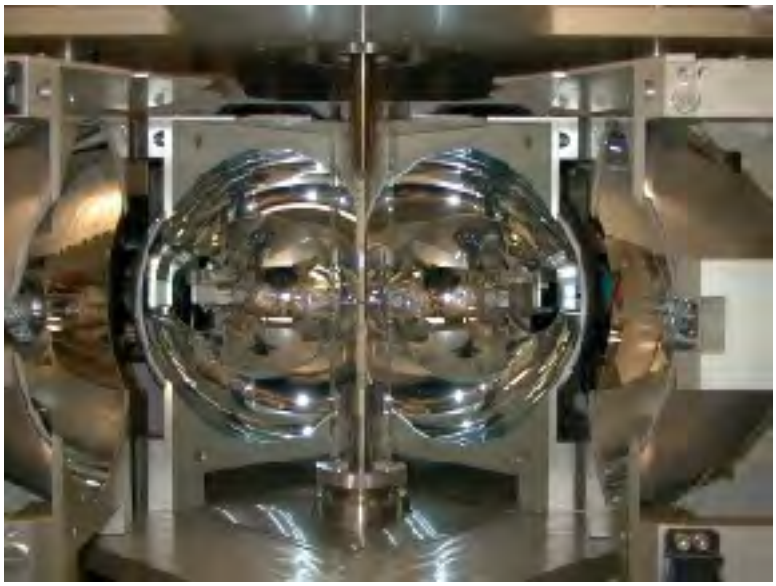

Figure 2.6. Photograph of the optical floating zone furnace in the laboratory of Professor K.R. Poeppelmeier. Two of the four elliptical mirrors can be seen, as well as the quartz tube, and support and feed rods.

which is created at the focus of a set of halide lamps and held via surface tension between polycrystalline "feed" and "support" rods. Growth proceeds by the upward translation of the focusing lamps and mirrors (and hence the liquid zone); as single crystal material nucleates on the lower solidification front, melting is simultaneously occurring on the upper liquidous front to replenish the liquid zone and maintain a dynamic steady state (Pless et al., 2003). In this way, single crystals of many compounds can be grown including peritectic compounds (Revcolevschi and Jegoudez, 1997) and solid solutions of fixed composition which can not be grown any other way (Kimura and Kitamura, 1992).

The optical floating zone furnace used here resides in the laboratory of Professor K. R. Poeppelmeier of the Department of Chemistry at Northwestern University and is a central user facility of the MRSEC Program at the Materials Research Center. The furnace is equipped with four 300 W tungsten halide lamps focused by four polished elliptical mirrors. The growth rates used varied from 0.15 to 0.12 mm/h, and the rods were counter-rotated at 18 rpm to provide for a thorough mixing of the solvent zone. An overpressure of 8 bar of oxygen was applied during the crystal growth in order to prevent reduction of the iron cation. In order to accommodate this pressure, the Teflon seals on the top and bottom rotation arms had to be replaced with elastomer spring-in-cup-type seals. Four of these seals were used; two were placed on the top rotation rod, and two were placed on the bottom.

CHAPTER 3

Surface Studies of α-Fe_2O_3 (Hematite) (0001)

3.1. Background

The alpha phase of Fe_2O_3, also commonly known as the mineral hematite, has a wide variety of applications due to its unique chemical and physical properties. It is an active and selective heterogeneous catalyst, and is reported as the active phase in the oxidative dehydrogenation of ethylbenzene to styrene (Wang et al., 1998). Hematite has been investigated as a photocatalyst for the degradation of aminophenol (Bandera et al., 2001) and is also believed to catalyze photochemical oxidation of SO_2 in the atmosphere (Toledano et al., 2001). It has also been shown to be moderately active in the oxidation of ammonia to nitrous oxide (Sadykov, et al., 2000).

In addition to its use in heterogeneous catalysis, iron oxides (including hematite) are ubiquitous in soils and sediments and play an important role in many global geochemical cycles (Maurice et al., 1995). For example, the oxidation of ferrous crustal minerals has a profound influence on the composition of the Earth's atmosphere, soils, waters, sediments, and sedimentary rocks (Hochella and White,

1990). Also, the redox chemistry that occurs in modern environments (i.e. weathering of iron bearing soils, acid mine drainage, etc.) can affect the biogeochemical cycle of many elements, including iron.

Finally, iron oxides are technologically important in ceramic pigments and colors, magnetic recording media, chemical and gas sensors, iron and steel refinement, corrosion, alumina production, and drinking water purification.

Bulk hematite has the corundum structure (a=5.035 Å, c=13.7489 Å), which consists of a hexagonally close packed array of oxygen atoms with Fe^{3+} in $\frac{2}{3}$ of the octahedral sites. This arrangement leads to a surface unit cell size of 5.03 Å (Figure 3.1). The oxygen anions within the basal (0001) plane deviate slightly from the ideal arrangement and form distorted octahedra with an average oxygen-oxygen interatomic distance of 2.91 Å in the bulk.

Stacking along [001] can be described in terms of alternating layers of ($\cdots$ Fe-Fe-$O_3\cdots$), where the subscript denotes the number of atoms within a surface unit cell. Here, the distance between adjacent iron layers is only 0.64 Å, and so the structure is also commonly described in terms of the stacking of alternating ($\cdots$ Fe_2-$O_3\cdots$) layers. As a result, three distinct bulk-like surface terminations are possible. The singly Fe-terminated (nonstoichiometric) (0001) plane is (electrostatically) nonpolar whereas the oxygen-terminated and double iron-terminated surfaces bear a finite dipole moment (Noguera, 2000).

Hematite has received much attention in recent years due to the rich and varied reconstructions that form on its surface following argon ion (Ar^+) bombardment

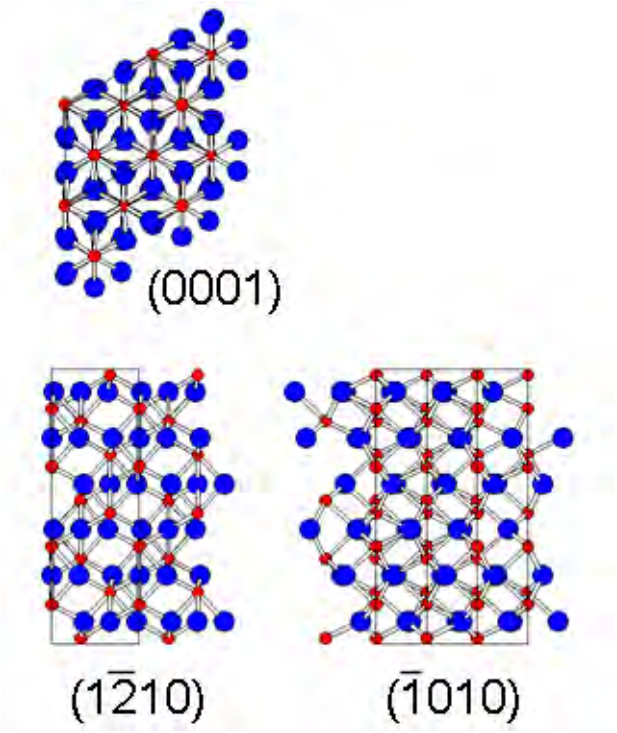

Figure 3.1. Ball and stick model of the hematite structure showing three orthogonal low-index planes. Oxygen atoms are the larger, darker spheres while the iron atoms are the smaller, lighter spheres. The subject of the current work is the basal (0001) plane.

and annealing treatments. Previous experimental studies have reported iron or oxygen terminated (1x1) (Ketteler et al., 2001a; Lad and Henrich, 1988; Shaikhutdinov and Weiss, 1999; Wang et al., 1988), Fe_3O_4 (Condon et al., 1994; Lad and Henrich, 1988), and so-called "biphase" selvedges (Condon et al., 1995; Ketteler et al., 2001; Shaikhutdinov and Weiss, 1999) on the (0001) surface of hematite after ion bombardment and annealing in the appropriate combination of temperature and oxygen partial pressure (Table 3.1). There have been several previous studies

on the surface of as-deposited thin film hematite samples in which the full surface structures have been determined by dynamical LEED tensor analysis (Chambers et al., 2000; Ketteler et al., 2001a) and intermediate-energy X-ray photoelectron diffraction (Thevuthasan et al., 1999). However, due to the dissimilarity of these thin film samples which have not been milled to the samples used in the present work, they will not be discussed in detail here.

Although there seems to be a wide body of work on this surface, it is surprising to note that none of the above studies has performed a full-blown surface structure calculation on a surface following ion bombardment and annealing and in some cases the results are very much open to interpretation. For example, the work by Condon et al. (1995) describes the formation of the biphase structure after annealing a mineralogical hematite sample at 827 °C and 7x10^{-7} Torr O_2. The STM images of this structure show what appear to be two coexisting, ordered phases and the LEED patterns are consistent with a large 40 Å supercell. Based on the LEED pattern and the periodicities observed in the STM images, the authors posit that this structure consists of coexisting islands of FeO_{1-x} (3 Å periodicity observed) with an unknown termination and Fe_2O_3 (5 Å periodicity observed) with an oxygen termination. The periodicities of the Fe and O sublattices in FeO_{1-x} (wustite), a rock salt oxide, are identical at 3.04 Å; hence indistinguishable. The periodicities of the Fe and O sublattices in hematite are 5 and 2.91 Å, respectively. The paper claims that the termination of the hematite islands is consistent with measuring O atoms at the surface, however they "can not rule out a contribution

from Fe atoms," thus leaving the structure of the biphase surface unresolved. In another example of the ambiguity in the hematite literature, Ketteler et al. (2001b) found that annealing in conditions of $3.75\text{x}10^{-5}$ Torr oxygen for 30 minutes at 727 °C produced *all of the following structures*: (1x1) α-Fe_2O_3 structure, the biphase structure of coexisting islands of FeO and hematite, and yet another biphase structure, this one consisting of coexisting islands of FeO and Fe_3O_4.

There have been several recent theoretical papers investigating the possible surface terminations of hematite, however they are all limited to the study of (1x1) bulk-terminated surfaces. The spin density functional theory (sDFT) calculations using the generalized gradient approximation (GGA) as the exchange-correlation functional of Wang et al. (1998) predict stability of both single-iron (Fe–O_3–Fe$\cdots$) and oxygen terminated (O_3–Fe–Fe$\cdots$) surfaces. The (Fe–O_3–Fe$\cdots$) surface is found to be the most stable under "typical experimental conditions", and the (O_3–Fe–Fe$\cdots$) surface was found to be stable only at very high oxygen pressures. This classically electrostatically polar surface is found to be stabilized by both huge out of plane relaxations and in-plane rotations of the surface oxygen of up to 10° (without breaking the surface symmetry). Warschkow et al. (2002), using atomistic models, similarly calculated large out of plane relaxations of a (1x1) termination however did not find the (O_3-Fe-Fe$\cdots$) surface to be stable (Warschkow, 2003).

It is because of this apparent lack of convincing information, and the desire to correlate recent reactivity studies (Liu, 2005) with the structure of these surfaces, that the present study was undertaken.

Table 3.1. Previous Studies of the α-Fe_2O_3(0001) Surface. All pressures are in Torr of O_2.

Reference	Preparation Methods	Observed Surface	Methodology
Lad(1988) mineral	775 °C, 30 min, 10^{-6} 900 °C, 30 min, 10^{-6} 900 °C, 60 min, 10^{-6}	Fe_3O_4 FeO (misinterpreted Biphase) (1x1)Fe_2O_3	LEED, XPS
Condon(1995, 1998) mineral	727 °C, UHV 827 °C, 7x10^{-7}	Fe_3O_4 Biphase	LEED, STM
Wang(1988) thin film	827 °C, 10 min, 7.5^{-4}	Fe and O term. (1x1)	LEED, STM sDFT
Shaikhutdinov(1999) thin film	810 °C, 1x10^{-5} 810 °C, 8x10^{-6} 810 °C, 7.5x10^{-7}	Fe and O term. (1x1) Fe term. (1x1) Biphase	LEED, STM
Ketteler(2001 a) thin film	827 °C, 10^0 827 °C, 8x10^{-6}	O term. (1x1) Hydroxy term.	LEED
Ketteler(2001 b) thin film	727 °C, 30 min, 3.75x10^{-5}	(1x1) or Fe_3O_4 Biphase or $\sqrt{3}$x$\sqrt{3}$R30°	LEED, STM

3.2. Impurity Analysis and Early Results

Early in the present study, TEM analysis was performed on specular mineralogical samples obtained from various sources including China, Russia, and Brazil. These samples were prepared in the standard way, as outlined in Chapter 2. Considering the literature as a starting point, and knowing that additional time must be given after TEM sample preparation to restore the surface stoichiometry, nucleate a reconstruction, and allow it to grow, the hematite samples were annealed at temperatures ranging from 800 to 930 °C for between 1 and 2.5 h. This is a much longer time than typically seen in the hematite surface literature (which is usually on the order of 30 min), but in our case the artifacts of the sample preparation process need to be annealed out and this requires a finite period of time. Annealing times less than one hour did not show evidence of a well-ordered surface, while those longer than 2.5 hours showed significant coarsening.

After Ar^+ ion bombardment, all of the samples showed diffraction patterns similar to those seen in Figure 3.2. Specifically, the bulk-allowed spots for the hematite structure are present along with a set of extra spots that correspond to a spinel-like layer in the near-surface region (when double diffraction is taken into account). In other words, they all exhibit a ferrite spinel-type phase near the surface. From the diffraction patterns, it is evident that this spinel phase forms epitaxially on the hematite substrate and is rotated 30° with respect to the hematite surface unit cell. The exact space group of the spinel near-surface phase

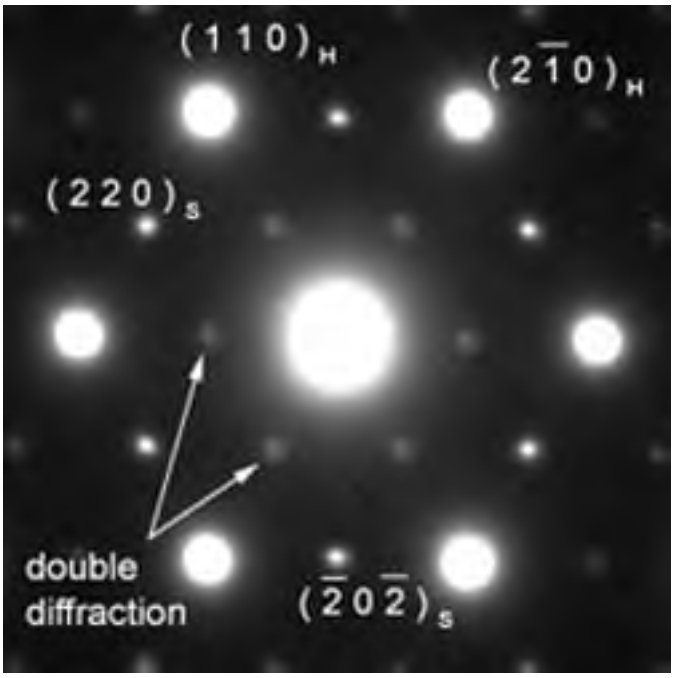

Figure 3.2. TEM diffraction pattern of a mineralogical hematite sample containing impurities. In addition to the bulk-allowed spots for the hematite structure, extra spots corresponding to the spinel phase are present.

can not be known from a single diffraction experiment in this orientation. It is possible that the spinel phase can be indexed to any number of spinel or spinel-like space groups. For example, all of the spots present in the pattern can be indexed to a defect spinel space group ($p4_132$). Alternatively, all of the spots can be indexed to an inverse spinel-type space group (fd3m) if double diffraction is taken into account. In order to determine which type of spinel phase is present on the surface of the impure hematite samples, and to rule out the presence of a hematite surface reconstruction, a test for double diffraction was performed as outlined in Edington

(1974). If a specimen is carefully tilted far off (∼10 degrees) the zone axis to a more kinematical diffraction condition, any spots arising from double diffraction will decrease in intensity or disappear altogether. This test was performed on the impure hematite samples, as seen in Figure 3.3. The spots suspected of arising from double diffraction were no longer visible on the pattern once tilted off the zone axis, thus proving that the spinel-like phase on the surface is similar in structure to Fe_3O_4 (magnetite, an inverse spinel of fd3m type, with {220} spots present along with those arising from double diffraction). A tilting experiment of this kind also proves that the spinel phase is in fact a near-surface phase and not a reconstruction of hematite, as spots arising from a surface reconstruction grow *more intense relative to the bulk* when the sample is tilted off the zone axis (Xu and Marks, 1993) due to the truncation of bulk rel-rods in reciprocal space.

From the transmission electron diffraction patterns it is obvious that the out of plane epitaxial relationship between the hematite (corundum) substrate and the ferrite spinel overlayer is that of $\{111\}_S \| \{0001\}_H$. The in-plane epitaxial relationship is impossible to determine unambiguously from this single diffraction experiment, but we believe based on the orientation relationship displayed in the diffraction pattern and previous studies (Heizmann et al., 1981) it is likely $\{110\}_S \| \{100\}_H$.

While all of the diffraction patterns appeared to the be the same (with a single exception; on one sample a (2x2) diffraction pattern was observed), the surface morphologies observed on the annealed mineralogical hematite samples varied

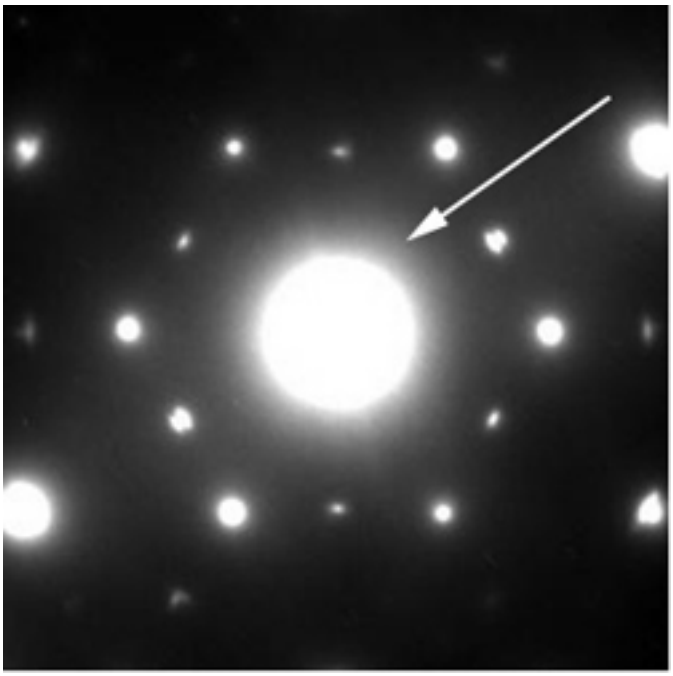

Figure 3.3. Off-zone axis TEM diffraction pattern of contaminated hematite. Note that the spots arising from double diffraction are no longer present (at arrow).

widely from specimen to specimen. For example, there appeared to be no repeatability from sample to sample in terms of temperature, atmosphere, and time. Figure 3.4 shows a bright-field TEM image of a mineralogical surface after annealing at 830 °C in oxygen flow for 2.5 h. Compare this with that of Figure 3.5, which shows a different sample annealed under similar conditions. Figure 3.6 shows a bright field TEM image of a mineralogical hematite sample containing what appear to be plate– or needle–like precipitates projecting out of the sample into the vacuum. Figure 3.7 shows a specimen containing either voids or inclusions which have faceted upon annealing. Typically in our group, previous work on

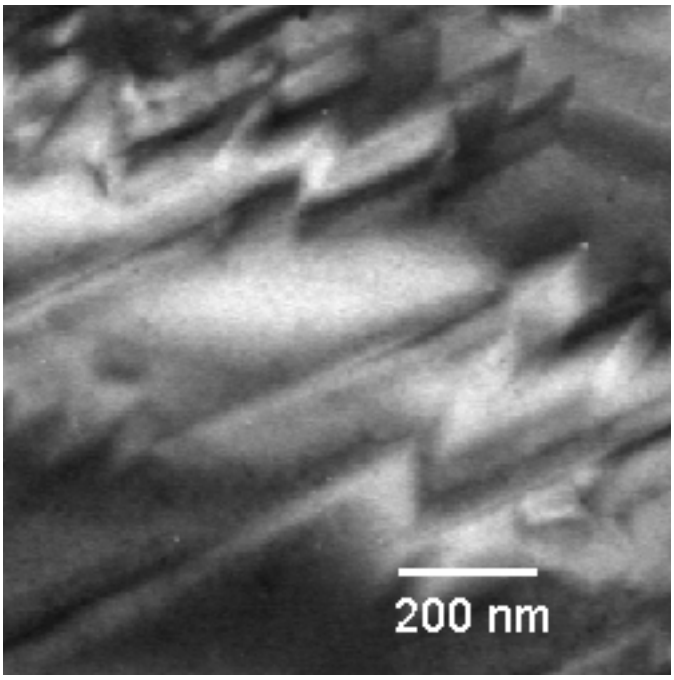

Figure 3.4. TEM BF image of mineralogical hematite following annealing at 830 °C for 2.5 h in oxygen flow.

oxides had been done using commercially available synthetic materials (Erdman, 2002), whose purity is guaranteed and consistent. Observations of the above mentioned defects appeared to be unique to mineralogical hematite. The appearance in the TEM images of these unexpected "phases" and the irreproducible surface morphologies prompted an examination of the purity of the mineralogical samples, with the suspicion that impurity species were responsible for the observed variation from sample to sample. In fact, Junta-Rosso and Hochella (1996) found for the specular mineral samples in their study that the (0001) surface "in all cases is contaminated with adventitious material and/or secondary phases."

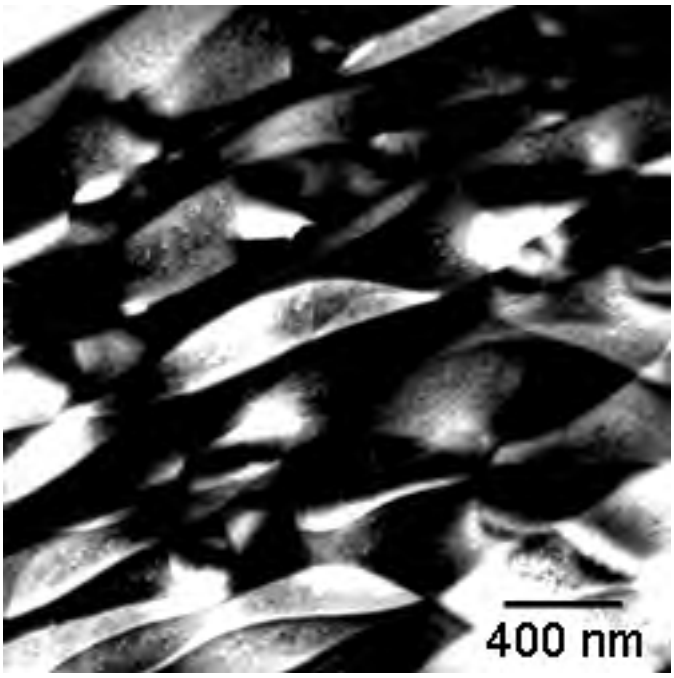

Figure 3.5. TEM BF image of mineralogical hematite following annealing at 930 °C for 2 h in oxygen flow.

In fact, this proved to be the case. Impurity analysis was performed on over 20 different hematite specimens using the methodologies outlined in Chapter 2. Not every crystal was tested using every methodology available; instead each crystal was tested for purity in at least one way. In these experiments, we were not concerned with obtaining the *exact* impurity profile of each sample but rather needed to know if any impurities could be detected by common means and if so, what were the major contaminating species. It was found that the actual atomic species present and their relative amounts varied drastically from crystal to crystal.

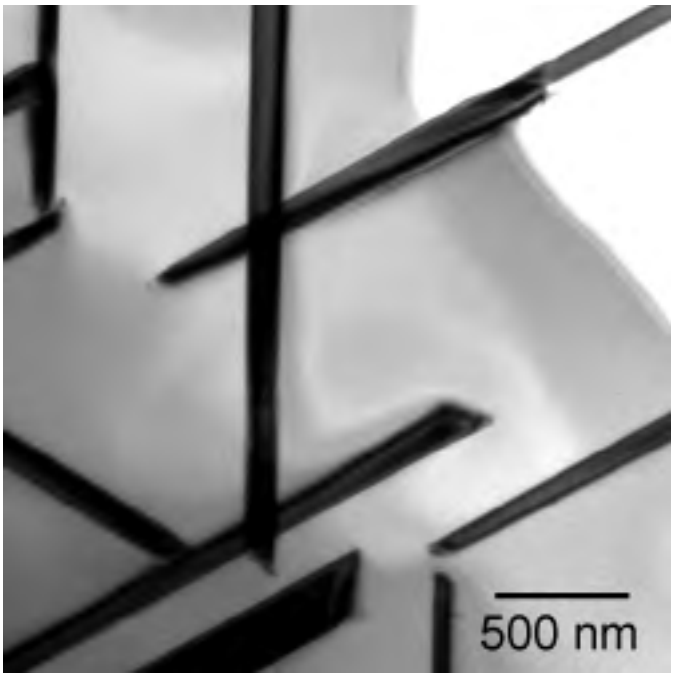

Figure 3.6. TEM BF image of an impure hematite sample showing needle– or plate–like precipitates.

As seen in Table 3.2, on average the specular hematite samples proved to be quite contaminated, with a large variation in contaminants. Impurity concentrations of these samples ranged from 0.5 wt. percent up to ∼10 wt. percent with an average of approximately 2 wt. percent. In all we examined the chemical composition of over 15 different samples of this type, primarily by XRF and XPS. XRF was chosen because it is a quick, easy, non-invasive test that does not require UHV and can be quantitative (although there are large errors associated with this technique). Considering the above observations, an effort was undertaken to grow the pure α-Fe_2O_3 required for reproducible surface science study.

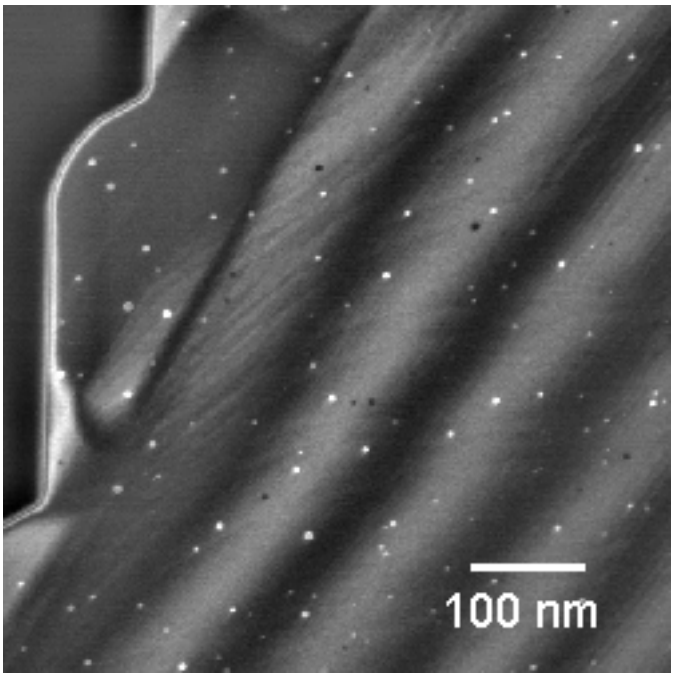

Figure 3.7. TEM DF image of impure hematite sample showing small faceted features believed to be inclusions of impurity species or voids which are artifacts from the sample preparation process.

Sample	Purity	Major Impurities	Minor Impurities
1	95 %	Mg, Mn, S, Si	Ca, Cl, Cr, Ti,
2	95 %	Al, Cd, Cr, Mg	As, Co, Cu, Mn, Pd, Si
3	99 %	Cr, Co, Si	Al, Cd, Mg, Mn, P, S, Sr, Zr
4	99 %	As	P, Si, Sr, Y

Table 3.2. Four representative XRF results for specular mineralogical hematite samples showing wide variety of contaminant species. Na was neglected, and data were normalized to 100%.

3.3. Single Crystal Growth

The properties of hematite are known to be sensitive to the type and concentration of impurities, preparation methodology, and thermal history (Sorescu

et al., 1999; Tasaki and Iida, 1963). For example, naturally occurring and synthetic α-Fe_2O_3 have been reported to have differences in their magnetic properties (Flanders and Remeika, 1965; Lin, 1961).

For the present work, single crystal samples are preferred (over large grained polycrystals) in order to perform studies on a simplified model system. Large single crystals can be cut to present practically any crystallographic plane, allowing one surface (or direction) at a time to be studied, so that fundamental information can be obtained from an otherwise complex system. For example, in heterogeneous catalysis, differences in reactivity between two surfaces of the same material may be caused by differences in the geometrical configuration of atoms on the different crystallographic planes (Jacobs and Somorjai, 1998). From a practical standpoint, single crystal samples also need to be large enough to facilitate mounting and manipulation in an analysis chamber. While thin film samples of hematite meet some of these requirements, there is often a need to mitigate the effects of a substrate and thermal history on these types of samples.

The synthesis of bulk single crystal α-Fe_2O_3 has been reported using various techniques including sol-gel, hydrothermal, vapor transport, and flux methods. Crystals grown using sol-gel (Nishino et al., 1998) or hydrothermal methods (Sahu et al., 1997) are small with an average grain size of typically a few microns. Likewise, crystals grown via vapor transport are typically small in size or exist only as thin platelets of [001] orientation (Gennari and Pasquevich, 1996; Sanchez et

al., 1986). The disadvantage of thin platelets (of any size) is that their thin nature precludes obtaining samples of a different crystallographic orientation from a single specimen. Hematite growth by flux methods are reported as early as 1854 and an extensive review can be found in Elwell and Scheel (1975). Wanklyn and co-workers (Garton et al., 1972; Wanklyn, 1970) have systematically studied a variety of flux systems for the growth of single crystal hematite, however the resulting crystals were relatively small in size, basal plates or of variable and unpredictable orientation, or as in the case of any crystal grown using flux techniques, may contain material incorporated from the flux (impurity concentrations are not reported in many cases). Barks and Roy (1967), employing the flux technique, were able to grow relatively pure large single crystals (averaging 0.1 at. percent potassium and 10 mm in size) using a $K_2B_4O_7$ flux, however these were thin basal-plane oriented platelets.

In contrast to the flux methods, growth in an optical floating zone furnace produces crystals that are large in three dimensions from which large samples of specific orientations can be obtained. This technique has been successfully employed to grow the related iron oxides wustite ($Fe_{1-x}O$) (Berthon et al., 1979) and magnetite (Fe_3O_4) (Kimura and Kitamura, 1992) in atmospheres of N_2 and CO_2 respectively, in order to control the oxidation state of iron. Nonetheless, in each case the resulting crystals required post growth annealing in order to obtain the desired stoichiometry, as the oxidation state of iron is known to be extremely atmospherically sensitive (Garvie and Buseck, 1998; Kimura and Kitamura, 1992).

In the following subsections the single-step growth of a large, extremely high purity, single crystal rod of α-Fe_2O_3 using a hemicalcic ferrite ($CaFe_4O_7$)-based solvent in the optical floating zone furnace in the traveling solvent zone configuration will be presented.

3.3.1. Experimental Details

3.3.1.1. Crystal Growth. The feed material was high purity α-Fe_2O_3 powder (Alfa Aesar, 99.998% pure). The solvent, $CaFe_4O_7$, was synthesized by calcining Fe_2O_3 (Alfa Aesar 99.998%) and CaO (Alfa Aesar 99.999%) in a 2:1 molar ratio in a platinum crucible in air at 970 °C for 24 h with several intermittent grindings. Both the feed and solvent materials were mixed with 10% by volume aqueous polyvinyl alcohol (Alfa Aesar 98-99%, hydrolyzed low molecular weight) in order to facilitate densification. It has been shown that the quality of the starting rods (density and uniformity, for example) directly influence the quality of the crystal grown in the optical floating zone furnace (Pless et al., 2003) and that, in some cases, binder is needed to facilitate the formation of high quality rods. The rods were formed by packing the powder with binder in a cylindrical rubber sleeve 6 mm in diameter by 90 mm long which was then evacuated, sealed, and hydrostatically pressed at 70 kPa. In contrast to the common methodology of forming a small solvent disk which is then attached to the support rod, in this study the entire support rod was formed from the solvent material. In order to form dense polycrystalline rods, the packed and pressed rods were sintered in air. The α-Fe_2O_3 feed rod was sintered at

1400 °C for 3 h and then at 1475 °C for an additional 3 h. The $CaFe_4O_7$ support rod was sintered at 1200 °C for 24 h, and powder X-ray diffraction (PXRD) showed it was a two-phase mixture of Fe_2O_3 and $CaFe_2O_4$ which is consistent with the fact that $CaFe_4O_7$ is not stable below 1170 °C (Millon et al., 1986). The feed rod was suspended from the upper shaft of the floating zone furnace using a platinum wire, while the support rod was rigidly affixed to the bottom shaft using steel wire. Growth was carried out in an optical image furnace (CSI FZ-T-10000-H-VI-VP, Crystal Systems, Inc., Japan) equipped with four 300 W tungsten halide lamps focused by four polished elliptical mirrors. The growth rates ranged from 0.15 to 0.20 mm/h, and the rods were counter-rotated at 18 rpm to provide for thorough mixing of the solvent zone. An overpressure of 8 bar of oxygen was applied during crystal growth to prevent reduction (see Section 3.3.3, below).

3.3.1.2. Crystal Characterization. Phase identification was performed by PXRD using a Scintag XDS 2000 diffractometer, CuKα radiation, and a nickel filter at room temperature. Data were collected at 0.02°/s at $10° < 2\theta < 80°$. Transmission electron microscopy (TEM) analysis and Laue diffraction were employed in order to determine the growth direction and crystalline quality of the as-grown rod. In order to prepare a TEM size sample, the rod was sliced into 500 μm thick wafers perpendicular to the growth direction. A 3mm diameter disk was cut from the center of each wafer and then mechanically thinned to 100 μm using SiC paper and then polished with 0.5 μm alumina paste. Next, the sample was mechanically dimpled to approximately 10 μm in the center and thinned to electron transparency

(denoted by the presence of a small hole) by 5 keV Ar^+ ions in a Gatan Precision Ion Polishing System (PIPS) operated at 20 μA. TEM analysis was carried out on a Hitachi UHV-H9000 TEM equipped with a double tilt stage and operated at 300 kV. Purity of the crystals was examined by inductively coupled plasma-atomic emission spectroscopy (ICP-AES) on a Thermo Jarrell Ash Atomscan 25. Spatial chemical mapping was performed using a Princeton Gamma Tech X-ray detector on a Hitachi S-3500N VP scanning electron microscope (SEM) operated at 12 kV.

3.3.2. Results

Initial growth attempts were made with a feed rod composed of 99.8% pure α-Fe_2O_3 (Alfa Aesar). The crystal was grown at a rate of 0.15 mm/h for approximately 205 hours. The resulting crystal measured 4 mm in diameter by 31 mm in length (Figure 3.8). The smooth rod revealed the shiny grey luster characteristic of hematite and did not develop facets during the growth. Upon cutting, the crystal was determined to be composed of small polycrystalline grains ($3mm^2$ approximate grain size in cross section) at the beginning of the growth which coarsened to a very large grained polycrystal near the end of the growth. The largest single crystal grain measured approximately $30mm^2$ in cross section and persisted for several mm along the length of the rod. Laue and TEM analysis of the large single crystal grains revealed the [001] direction in the hematite corundum structure to be parallel to the rod growth direction to within 1° (the resolution limit of a back reflection Laue experiment in the J.B. Cohen facility at Northwestern University).

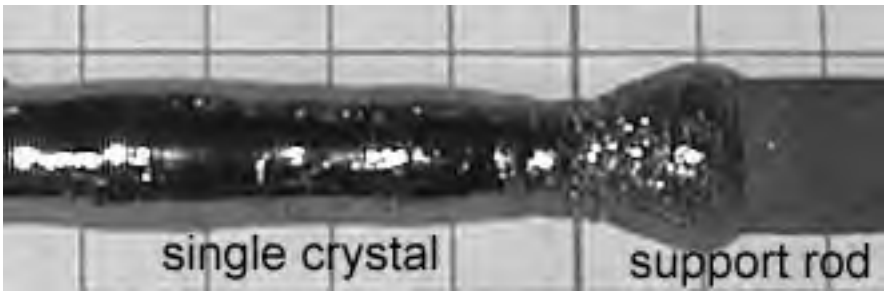

Figure 3.8. Synthetic polycrystalline hematite rod (left6 mm on end not shown), from 99.998% pure starting material and 0.15 mm/h growth rate. Each line represents 5 mm. The $CaFe_4O_7$ support rod is to the right side, only the first few mm are shown.

PXRD analysis confirmed the presence of α-Fe_2O_3 and no contaminating phases (Fe_3O_4, $Fe_{1-x}O$, $CaFe_4O_7$, etc.), while ICP-AES revealed the Ca:Fe ratio to be 0.005. There was no evidence of a Ca-rich second phase by optical microscopy, TEM, or EDX (spatial X-ray mapping) and it is therefore assumed that the CaO is in solid solution.

The highest quality and largest crystal was successfully grown using 99.998% pure α-Fe_2O_3 powder at a growth rate of 0.2 mm/h for approximately 162 h (Figure 3.9). This rod measured approximately 5 mm in diameter by 33 mm in length. The total growth time was limited by the length of the feed rod prepared. Again, the crystal was determined to grow along the [001] direction by both Laue and TEM methods and had the shiny grey luster characteristic of hematite. This crystal did not display any continuous faceting but did exhibit five rings where the diameter of the rod was larger and more constant than the other areas. While a change in operating conditions can not be ruled out (lowering of the feed rod by the operator

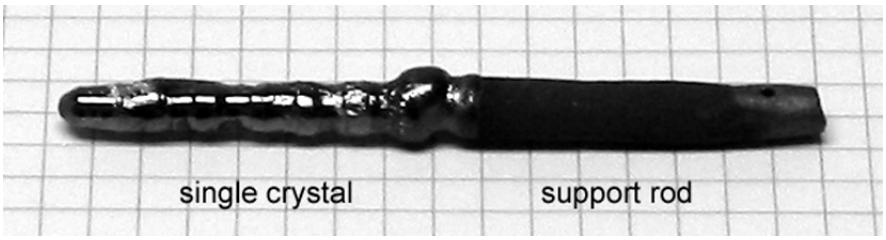

Figure 3.9. Synthetic single crystal hematite rod, from 99.9998% pure starting material and 0.2 mm/h growth rate. Each line represents 5 mm. The support rod is on the right hand side, and the single crystal is to the left.

would cause more material to melt and hence increase the diameter of the growing rod), this maybe due to facets presenting the $r(10\bar{1}1)$or $n(22\bar{4}3)$ faces which are common beveling forms in hematite (Hurlbut, 1971). In this case, the entire rod was a single crystal (meaning no grain boundaries) except for the initial 3 mm of growth which was polycrystalline. The Ca content of the as-grown crystal was below the 0.5 μg/L (ppb) detection limit for calcium in the Thermo Jarrell Ash Atomscan 25 ICP-AES.

TEM analysis was performed on several representative samples of each of the crystals grown and revealed the crystalline quality of the rods to be excellent. Imaging (bright and dark field) as well as diffraction techniques did not provide any evidence of twinning, stacking faults, or dislocations in the as-grown crystal. In addition, there was no evidence of twinning, voids, inclusions, or cracks by optical microscopy.

3.3.3. Analysis and Discussion

Based on the work of Kimura and Kitamura for the growth of single crystal Fe_3O_4 (Kimura and Kitamura, 1992), the optical floating zone method has been shown to *behave as a closed system* (even though it is operated at constant oxygen pressure and is therefore an open system) for the preparation of iron oxides, meaning that the path of equilibrium crystallization follows the isopleth at the relevant composition. In the closed binary Fe-O system, hematite melts congruently to form liquid oxide at approximately 1575 °C (Muan and Osborn, 1965). For a system of this type, one should be able to obtain hematite directly from a melt of equal composition.

Initial attempts to grow hematite directly from the melt at oxygen pressures ranging from atmospheric to 5 bar failed, as the samples reduced to magnetite and the accompanying oxygen release formed bubbles which destabilized the molten zone. Magnetite could be detected with a common magnet and was confirmed by PXRD. As expected the growth of hematite (in contrast to magnetite) from the melt in the optical floating zone furnace at moderate pressures does behave as an *open system*, which it is, where the path of equilibrium crystallization is constrained to follow the relevant oxygen isobar. In order to avoid the magnetite-hematite two phase region of the binary phase diagram in an open system, pressures approaching 50 atm are needed (Phillips and Muan, 1960) in order to congruently melt and cool hematite directly. This is corroborated by the work of Balbashov

et al. (1985), who demonstrated hematite growth directly from a melt of equal composition at oxygen pressures above 35 atm and in a specially modified floating zone furnace (Balbashov and Egorov, 1981) which could accommodate the high pressure required. The maximum total pressure in the image furnace (Crystal Systems, Inc., Japan) is limited because the growth takes place inside of a sealed quartz tube which can safely hold approximately 9 bar of pressure when it is in good physical condition. In addition, the quartz tube is subject to devitrification when exposed to temperatures above 1150 °C. Devitrification, which can weaken the mechanical integrity of the tube, and therefore its ability to hold high gas pressures, can lead to failure and explosion. Thus the furnace is equipped with a poppet valve which limits the attainable pressure to 9 bar; even so the system should be monitored continually to ensure the integrity of the tube.

Considering these observations, we attempted to grow hematite employing a solvent which would form a stable liquid phase that would not reduce under the pressures safely attainable in the traveling solvent zone furnace. The use of a solvent in the optical floating zone furnace may seem like a contradiction because one of the main advantages of the system is that it is crucible free and therefore mitigates contamination. However, with the present configuration (meaning maximum attainable safe operating pressure of 8-9 bar), hematite can not be directly grown from the melt.

In order to find a suitable solvent for use in an optical floating zone furnace, several additional considerations were taken into account compared to those for a

flux assisted growth in a crucible. First, the solute and solvent must form a liquid phase with enough surface tension to sustain a molten floating zone between the two rods during the growth process (Kimura and Kitamura 1992). Preferably the solvent should not penetrate deeply into the feed rod by capillary action along grain boundaries, thereby causing an unstable growth condition. In addition, the solvent chosen must have a low vapor pressure in the liquid phase such that it will not evaporate during the course of the growth. If the solvent of choice was volatile and evaporated during the course of the growth, the liquid composition would change constantly and effect the establishment of the dynamic equilibrium needed for continuous growth of a crystal of constant composition. Early growth attempts using V_2O_5 and WO_3-based solvents failed because of severe penetration and solvent volatility, respectively.

Hematite was grown successfully using a hemicalcic ferrite ($CaFe_4O_7$)-based solvent which serves to both lower the temperature at which hematite solidifies from the melt compared to the binary Fe-O system and prevent hematites reduction to magnetite. As mentioned previously, reduction to magnetite was observed in the Fe-O binary system at the growth conditions achievable in the optical floating zone furnace. $CaFe_4O_7$-based solvent was chosen because the Ca^{2+} ion (1.0 Å with 6-fold coordination) is larger than the ferric iron ion (with 6-fold coordination, 0.645 Å in the high spin configuration, 0.55 Å in the low spin configuration) (Shannon, 1976), because CaO is nonvolatile in the temperature regimes used for single crystal growth of hematite (the vapor pressure at 2337 °C is only 1.013 mbar (Brewer,

1953)), and because it lowers the temperature at which hematite solidifies from a melt by 350 °C compared to pure hematite (Hillert et al., 1990).

$CaFe_4O_7$ ($2Fe_2O_3 \cdot CaO$) is a high temperature phase which is metastable below 1170 °C. In the true binary system, $CaFe_4O_7$ undergoes a peritectic reaction at 1250 °C, decomposing to hematite and liquid. The two phase mixture (hematite plus liquid) then melts to form a single liquid phase of $CaFe_4O_7$ composition at approximately 1375 °C. Relating to single crystal growth in the traveling solvent zone furnace, this means that once the top of the support (solvent) rod is fully melted and a liquid of $CaFe_4O_7$ composition is formed, hematite will nucleate onto the support rod because of the dynamic steady state and large temperature gradients present. As hematite is precipitated from the melt, and therefore in order to *prevent* so-called zone leveling (Pfann, 1966) from occurring (in which the equilibrium would continue down the liquidus line to the peritectic point and establish a Ca-rich steady state melt composition thereby depositing solid $CaFe_4O_7$), α-Fe_2O_3 needs to be replenished via the feed rod to maintain a constant Fe-rich liquid composition. This is analogous to the "push-pull" method of single crystal growth developed by Nelson for growth of germanium (Nelson, 1956), by which the liquid composition is held constant by continuously adding material (of the same composition) as the growing rod. If the equilibrium liquid composition at the solidification front remains Fe-rich, then only hematite, what is commonly known as the first grown material, will be deposited (Figure 3.10a). Note that this

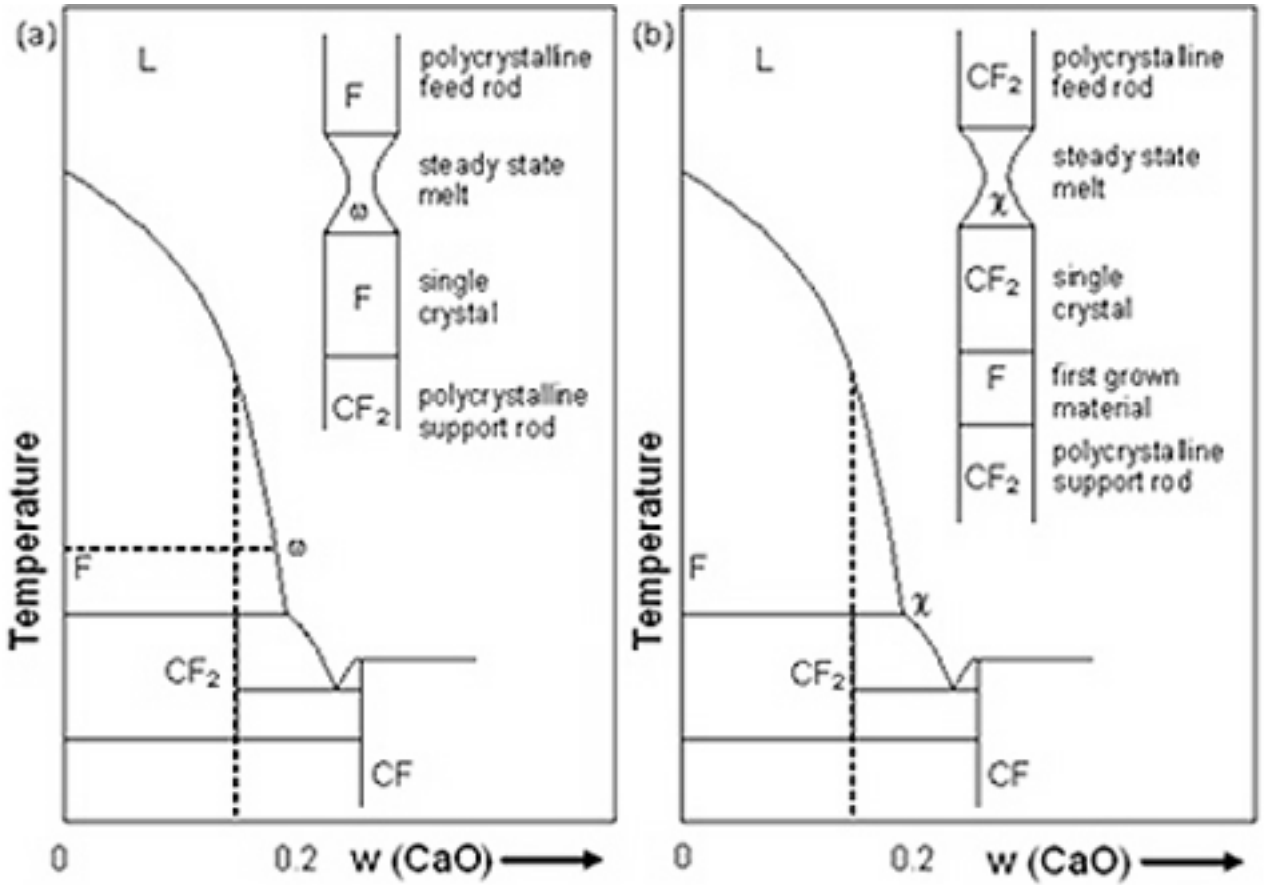

Figure 3.10. Schematic view of crystal growth in a peritectic system. F=Fe_2O_3, C=CaO, and CF2=$CaFe_4O_7$. (a) Growth of a congruently melting compound (F) from an incongruently melting compound (CF2). This is a schematic of Fe_3O_3 growth from $CaFe_4O_7$. (b) Growth of an incongruently melting compound. This is a schematic representation of the growth of $CaFe_4O_7$ from the melt.

procedure is different from the case of other peritectic systems in which zone leveling and deposition of the incongruently melting phase is desired. In the case for growth of $Mg_3(VO_4)_2$ (Pless et al., 2003), $Y_3Fe_5O_{12}$(YIG)(Kimura and Kitamura 1992), and high T_c cuprates (Revcolevschi and Jegoudez 1997) for example, both the support (or solvent disk, as the case may be) and feed rods are composed of the incongruently melting material and in these cases, zone leveling occurs and after a brief period where what is known as the first grown material is deposited, crystallization of the incongruently melting phase commences (Figure 3.10b). In fact, the optical floating zone furnace in the traveling solvent zone configuration is unique in its ability to handle such peritectic phase transitions and grow single crystals of incongruently melting materials.

Experimentally there are several considerations to address in employing the $CaFe_4O_7$-based solvent. First is that the CaO-Fe_2O_3 system is not a true binary system in realistically attainable pressure regimes. In fact, at 1 atm of O_2 there is a small magnetite (Fe_3O_4) and magnetite plus liquid stability region above 1400 °C and 0.93 wt. percent Fe (Phillips and Arnulf, 1958). We have found that the formation of magnetite at any stage is detrimental to the single crystal growth, because the resulting liberation of oxygen destabilizes the molten zone which can not be recovered. Therefore, even though upon cooling any magnetite formed would transform to hematite according to the equilibrium phase diagram, growth in this regime must be avoided entirely. This can be accomplished by maintaining the oxygen pressure as high as safely attainable to minimize this magnetite phase

regime, being careful in the initial stages of growth to melt only a small amount of the hematite feed rod (the amount of which will vary with the diameter of the rods and the growth rate), and by using the minimum power necessary in the heating lamps. Practically, we found that this meant using the lowest power lamps that will melt the support and feed rods completely (we found 1000 W lamps worked best) and also heating the rods until they are just melted through but no more. Employing this solvent system and taking into account the above considerations, a stable molten zone was obtained and the growth proceeded in the normal way, that is to say the molten zone traveled along the length of the feed rod while α-Fe_2O_3 crystallized onto the support rod from solution due to a dynamic steady state.

As mentioned above, in order to prevent reduction to magnetite and resulting release of gaseous oxygen, which destabilizes the molten zone, an overpressure of 8 bar O_2 was applied for the duration of the growth. The standard Teflon seals at the top and bottom of the quartz tube in the imaging furnace had to be replaced with spring-in-cup seals in order to maintain this high pressure over the long time period (the floating zone furnace is not designed for elevated pressure). In this manner the furnace was able to maintain the required pressure with only momentary fluctuations of less than 1 bar.

Additionally, we found that the successful growth of hematite at oxygen pressures near 8 bar in the optical floating zone furnace is directly dependent on when, in the start up procedure, that pressure is applied to the system. The stability of the molten zone and quality of the resulting crystal were found to be directly

dependent on the pressure of oxygen inside the quartz tube. In order to prevent bubbling (release of gaseous oxygen accompanying a reduction of Fe^{3+} to Fe^{2+}), a pressure of approximately 6 bar must be applied before the lamps are turned on and melting of the support charge begins. When the furnace is pressurized in this manner, the molten zone is not reduced, yet the gas pressure in the furnace can accommodate the additional increase in pressure caused by the gas expansion upon heating. As soon as the $CaFe_4O_7$ support rod is melted the balance of the pressure is applied and then the two rods are joined. This process could be simplified by the addition of a back-pressure regulator which allow the furnace to be backfilled to 8 bar before the lamps are turned on. In this case, the back-regulator would release gas as needed during the heating procedure to ensure that the furnace did not exceed a safe working pressure. When growth was attempted by first melting the rods in air and then applying the pressure, the molten zone was not stable, collapsed after several hours, and could not be reformed again as the flux had flowed down the edge of the support rod.

It should be noted that using the optical floating zone furnace in the traveling solvent zone configuration with this type of flux system is a new methodology for growing single crystals of atmospherically sensitive materials. Unique to the growth of hematite, we have used the peritectic reaction to our benefit in thermally decomposing an incongruently melting material in order to grow a large single crystal of an entirely different phase. There is no solvent that exists in the binary Fe-O system. As previously mentioned, in contrast to the quite common method

of employing a solvent from within the system of interest (for example, in the case of YIG (Kimura and Shindo, 1977) and high T_c cuprates (Takekawa and Nozaki, 1988)), we have used a solvent which contains a species which is wholly undesirable in the final product. While this is not the first time that a foreign species has been introduced as a solvent in this type of furnace configuration, it is the first time that it has been used in this way and resulted in a 100% pure, entirely single crystal rod in a single-step growth which required no post-growth annealing. ZnO was grown in the optical floating zone furnace using V_2O_5+B_2O_3 and V_2O_5+MoO_3 fluxes (Oka et al., 2002), however the growth required the "twice scanning" technique, contained residual V or Mo contamination, and was polycrystalline.

3.4. Impurity Stabilized Near-Surface Phase on Ion Bombarded α-Fe_2O_3

The high purity single crystals obtained from the optical floating zone growth proved to behave differently following ion bombardment than the mineralogical samples observed previously. In fact, only when pure crystals became available was a comparison able to be made between the two which highlighted this difference. The following sections describe these observations.

3.4.1. Experimental Details

In contrast to impure samples (Section 3.2), following Ar^+ ion bombardment nominally pure hematite samples do not show any evidence in the transmission electron

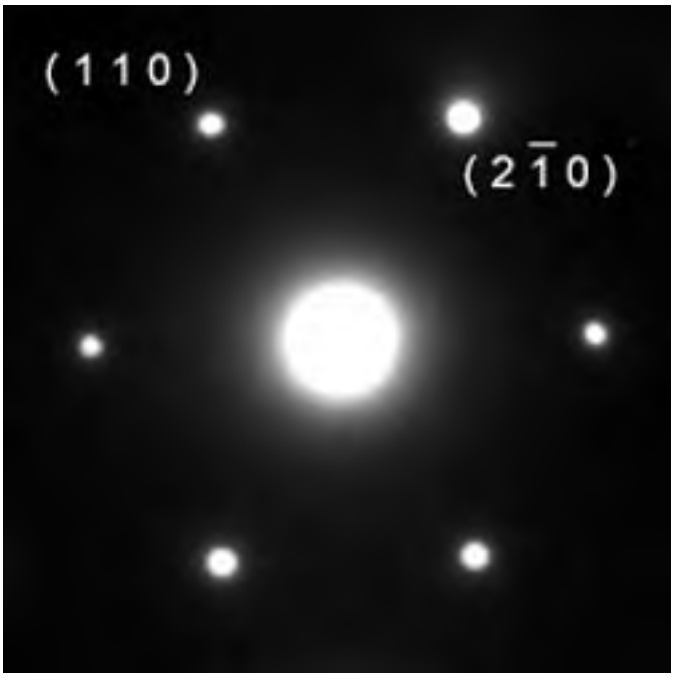

Figure 3.11. TEM diffraction pattern from a pure hematite sample following ion bombardment. Note the absence of spots from a spinel phase. Only the bulk-allowed spots for the corundum structure are seen.

diffraction pattern of a near-surface spinel phase (Figure 3.11). In fact, the ion milled TED patterns of these samples show only bulk-allowed spots for the corundum structure (space group 167, R$\bar{3}$c). Invariant of purity (Figures 3.12 and 3.13), all hematite samples annealed in a flow of oxygen at 830-930 ° for 2 to 2.5 h the hematite show (1x1) diffraction patterns indicative of a bulk-terminated surface.

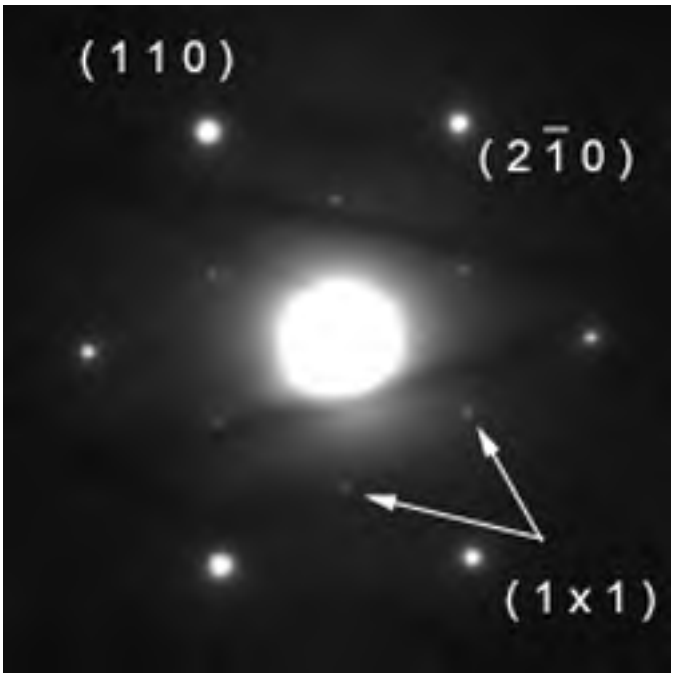

Figure 3.12. TEM diffraction pattern from an impure hematite sample following annealing. Note the presence of (1x1) spots in the pattern as well as faint Kikuchi lines indicating the sample was relatively thick.

3.4.2. Results and Discussion

It is well known that Ar^+ ion bombardment drastically modifies the surface stoichiometry of oxide samples and that significant disorder and reduction can occur. Previous studies (Chuang et al., 1978; Lad and Henrich, 1988) which examined the ion bombarded surface of hematite using LEED and XPS found significant contribution to the Fe2p peaks from Fe^{2+} in the XPS spectra and absence of a LEED pattern after only 50 s of milling at 1 kV (Brundle et al., 1977). Another study using conversion-electron Mössbauer spectroscopy and small angle x-ray diffraction

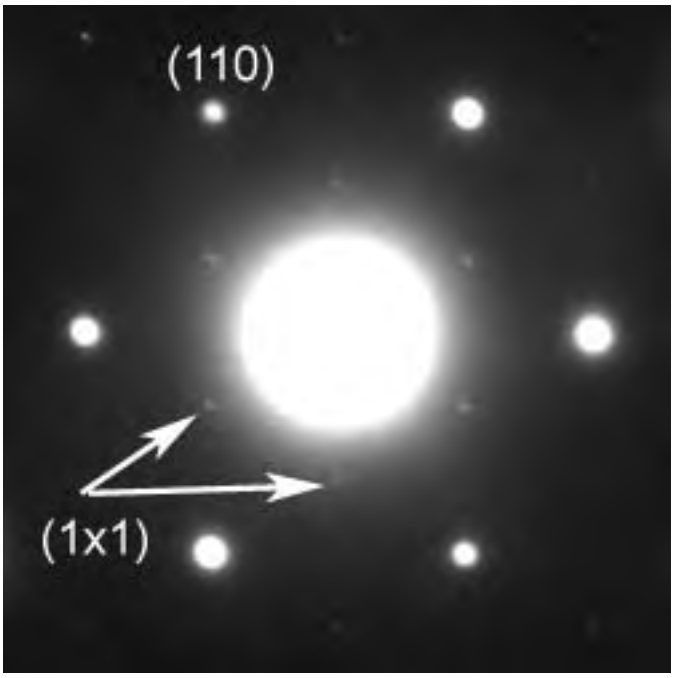

Figure 3.13. TEM diffraction pattern from a pure hematite sample following annealing. Note the presence of (1x1) spots in the pattern.

(Joshi et al., 1989) found that α-Fe_2O_3 reduced readily to sub oxides (Fe_3O_4 and FeO) following bombardment in doses of 1.0×10^{16} ions/cm^2 and above.

The disadvantage to using LEED for this type of work is that it cannot penetrate past the disordered surface layer to "see" any crystalline phases which may lie below. In contrast, the TEM is uniquely suited to this type of study by virtue of the transmission geometry which can penetrate through the entire depth of the specimen. If a crystalline near-surface phase is present which lies beneath a disordered outer layer, hidden from the LEED probe, it will nonetheless be present in the transmission electron diffraction pattern.

Therefore, based on the previous studies of this system and our own results, we believe the morphology of these ion milled surfaces to be the following: all samples, whether or not they contain impurities, are covered in a disordered layer following Ar^+ ion bombardment in which there is some fraction of the original Fe^{3+} reduced to Fe^{2+} and even Fe^0. Further, we believe that impure samples have an epitaxial ferrite spinel layer lying beneath this disordered layer. In contrast, the pure hematite samples do not have the ferrite spinel phase and are simply disordered and reduced on the surface.

The idea of having a spinel layer present (as opposed to a surface reconstruction of hematite) agrees well with the intensity ordering of the spots observed. More specifically, the {220} spinel spots in Figure 3.2 are quite bright and the double diffraction spots are slightly weaker than those, which is consistent with the fact that it is a surface phase with double diffraction and not a reconstruction. In a transmission electron diffraction pattern, spots arising from a surface reconstruction are typically four orders of magnitude weaker than bulk spots. If the spots in this pattern had come from a surface reconstruction, the intensity of the spots would be much reduced. Furthermore, due to the truncation of bulk rel-rods and elongation of surface rel-rods at a surface in reciprocal space, any spots arising from a surface reconstruction become *stronger* when the specimen is tilted off of the zone axis (Xu at al., 1993). This is in direct contradiction to our observations (Figure 3.3) where as the samples are tilted, the spots arising from double diffraction disappear entirely. The above analysis is also consistent with

the interpretation of similar LEED patterns on hematite surfaces seen in the work of Lad and Henrich (1988), Condon et al. (1994), Barbieri et al. (1994), and Weiss et al. (1993).

Upon annealing *in an oxygen-rich environment* all samples, regardless of their impurity content, show (1x1) diffraction spots characteristic of a bulk-truncated hematite surface. XPS spectra of impure annealed hematite samples show the persistence of the impurity species indicating that they did not appreciably diffuse away from the surface. The XPS spectra also indicate that there is no significant surface segregation of impurity species upon annealing. This indicates that under the present annealing conditions, hematite is the stable phase and can accommodate these impurities in its structure as point defects (Barbieri et al., 1994; Muan and Osborn, 1965; Park and Kim, 1999).

The stoichiometry of spinel (AB_2O_4) and inverse spinel ($B(AB)O_4$ —generally $(A_{1-x}B_y)(A_xB_{2-y})O_4$) materials is such that they have a higher cation to anion ratio than a given corundum material containing the same constituents. For example in the case of iron and oxygen containing compounds, the Fe:O ratio in hematite is 0.66 while the ratio in magnetite is 0.75. Charge neutrality in a spinel is accommodated by a reduction of the cation oxidation state. In the case of the inverse spinel Fe_3O_4, charge neutrality is maintained when some of the iron on the octahedral sites exists in the Fe^{2+} oxidation state. Therefore, to reduce Fe_2O_3 to a spinel, there needs to be a net loss of oxygen and a compensating reduction of Fe^{3+} to Fe^{2+}.

This loss of oxygen and reduction to Fe^{2+} could also be achieved by the incorporation of impurity species into the hematite lattice, which must be accompanied by a charge-compensating lattice defect in order to maintain overall charge neutrality of the crystal. For example, the substitution of a higher valent ion for Fe^{3+} will lead to a reduction to Fe^{2+} whereas the substitution of a lower valent ion will lead to a charge compensating oxygen ion vacancy. In fact, this has been shown experimentally in a study by Park and Kim (1999).

Our results indicate that the impurity species found in hematite along with their charge neutrality maintaining defects must accelerate or stabilize the formation of a ferrite spinel upon *further* reduction via Ar^{+} ion bombardment. In other words, it is not hard to form a ferrite spinel from hematite when many of the "ingredients" (including oxygen deficiency, and Fe^{2+}, or even in some cases a 'B' cation) are already present. This is not surprising when it is considered that many of the common impurity elements found in hematite crystals readily form stable ferrite spinel compounds on their own. For example, the spinel group contains compounds such as magnesioferrite (Fe_2MgO_4), ulvospinel (Fe_2TiO_4), franklinite ((Zn, Fe,Mn)(Fe,Mn)$_2O_4$), chromite ($FeCr_2O_4$), and a host of others containing iron along with V, Al, Ge, Ni, Co, and Cu.

It must be stated that oxygen deficiency and presence of Fe^{2+}, while possibly necessary, are not a sufficient condition to form a stable crystalline spinel phase upon ion milling. If that was the case, then the epitaxial layer would also show up on the surface of the pure hematite samples where we argue that there is also

reduction to Fe^{2+} and loss of oxygen (although to a much lesser extent). This points to the fact that either the impurity species themselves play a role in the stabilization of the spinel phase, or that when they are present their associated charge compensating defects are present in numbers much higher than one could get from ion milling alone.

Interestingly, the formation of the ferrite spinel phase does not depend on the type of contaminant present in the samples—it does not appear necessary to have a "spinel-forming" element present in the sample. We attribute this again to the fact that practically any type of impurity must have an associated charge compensating defect (oxygen vacancy or reduction of Fe^{3+} to Fe^{2+}). A good example of this is the hematite crystal containing calcium which itself is not normally thought of as a spinel-forming element but nevertheless helped to stabilize the spinel phase.

The above result points to an interesting observation: it appears that the relative amount of impurity has no effect on the formation of the spinel phase, at least in the quantities that we have measured. As mentioned above, the presence of even 0.2 at. percent Ca was enough to stabilize the formation of the near-surface spinel phase. While it maybe true that the cutoff for impurity concentration will vary from element to element, our experiments have shown that even a very small amount of impurity species is enough to stabilize the formation of the spinel surface phase.

3.4.3. Comparitive Low Pressure Annealing Results

In order to compare our results more directly to the literature, and explore a wider range of applicability for the surface science community studying hematite, an impure ion milled hematite sample (milled at 5 keV, 15 mA in the PIPS for 2 h and having no LEED pattern) was treated at 900 °C for 30 min in 1×10^{-6} Torr of oxygen in order to reproduce the so-called biphase structure discussed in Lad and Henrich (1988), Condon et al. (1995), and Shiakhutdinov et al. (1999) and observed with LEED (Liu and Chiaramonti, 2004). When treated this way, the impure specimen showed the persistence of the spinel phase after annealing in conditions where the biphase structure has been observed to form. The LEED pattern was consistent with an Fe_3O_4–type (impurity stabilized spinel) termination. As a control, and to verify that we can indeed observe the biphase structure under these annealing conditions, several different mineralogical and thin film specimen (known to contain impurities) were ion-milled using more traditional surface science approaches, namely Ar^+ bombardment at 10 mA emission current, 0.8 μA sputtering current for 30 min (as compared to several h in the previous cases) at nearly normal incidence angle. After milling, these specimen showed no LEED pattern. Following treatment at the same temperatures and pressures stated above, the unique and characteristically floreted biphase LEED pattern was observed (see ref. Condon et al., 1995). These results indicate that the relative amount (as dictated by the time, beam energy, and momentum transfer, e.g. degree of incidence)

of ion bombardment prior to annealing has an effect on the resulting surface structure in impure samples and that care must be taken when cleaning them prior to surface science study.

Under partial pressures of oxygen ranging from 0.2-1.0 (with a total pressure of approximately 1 atm), the spinel-like phase appears to be transient and does not have an effect on the resulting surface structure. However, for impure samples treated in lower partial pressures, the extent of reduction prior to annealing has an effect on the resulting surface structure. In this study, we have observed the stability of this spinel phase under a broader range of oxygen partial pressures than have been previously seen in the literature. While we can not rule out the fact that the spinel phase may *not* form under the bombardment conditions used in more traditional surface science experiments, it is nevertheless important for those attempting this kind of study to be aware of the fact that in impure specimens (either mineralogical in origin or doped to enhance conductivity for scanning tunneling microscopy), this impurity-stabilized spinel phase can and does form under certain bombardment conditions and may be easily confused with an Fe_3O_4 termination (reconstruction) of hematite.

3.5. Biphase Structure

Recent temperature programmed desorption (TPD) studies (Liu, 2005) on α-Fe_2O_3(0001) found that methyl radical chemistry occurred on the Fe_3O_4 terminated surface but not the biphase terminated surface. In order to understand

the difference in reactivity between these two surfaces, one must know the surface structure. The atomic structure of Fe_3O_4-terminated surfaces as a function of annealing conditions is relatively well agreed upon (Ahdjoudj et al., 1999; Barbieri et al., 1994; Condon et al, 1994, 1997; Lennie et al., 1996; Ritter and Weiss, 1999). As mentioned previously, however, the atomic structure of the biphase surface is not. The following sections outline an attempt to duplicate the biphase structure on hematite samples prepared for TEM analysis (in order to solve the structure via TED and Direct Methods) as well as discuss the results as they apply to correlating surface science studies to those performed on a TEM sample in the gas treatment cell.

3.5.1. Sample Preparation

Two pure (0001) oriented mineralogical hematite TEM samples (no evidence of a surface spinel phase) were prepared using the techniques outlined in Chapter 2. One of these samples was pre-annealed in a 50 ccm flow of oxygen (1 atm total pressure) at 830 °C for 1 h, the other remained in the as-milled state. Both samples were then introduced into the SPEAR system and treated to produce the biphase structure. The samples were annealed in $1x10^{-6}$ Torr of oxygen at 830 °C (± 30 °C) for 20 minutes in the gas treatment cell. The mass spectrometer pressure was calibrated against the ion gauge in the SPEAR transfer chamber. In order to prevent thermal shock to the alumina heater, the samples were ramped up at approximately 250 °C per h and cooled at approximately 350 °C per h.

3.5.2. Biphase Results and Discussion

When put into the UHV-H9000 microscope for analysis following treatment, the as-milled sample was pulled out of the specimen cartridge by the microscope objective lens pole piece (a large electromagnet), indicating it was magnetic. The sample pre-annealed in oxygen was not. Unexpected experimental issues prevented the acquisition of TEM diffraction patterns or images from either of the samples.However, it is a fact that the as-milled sample is magnetic and the pre-annealed sample is not. Both of these samples were cut from the same crystal so any differences in purity can be ruled out.

The fact that one of the samples is magnetic indicates that it had transformed, at least to some degree, into Fe_3O_4 (magnetite) which is ferromagnetic. The difference between the two samples appears to be the the pre-annealing step. It is well known that following argon ion bombardment, hematite samples are oxygen deficient and the Fe^{3+} has reduced to some extent to Fe^{2+}. Based on these observations, it appears that even for clean samples, where there is no impurity stabilized spinel phase present before annealing, the amount of reduction due to the ion bombardment is enough to prevent the sample from obtaining the biphase structure. In other words, the as-milled sample was already too far reduced. It follows that in order to duplicate the biphase structure in a TEM sample, it must be pretreated in oxygen before it is annealed in order to reoxidize the surface following argon ion bombardment.

This is not the case in traditional surface science experiments where samples are routinely ion milled and then annealed in the above mentioned conditions to produce the biphase structure. Since the same type of samples have been used in both studies, the differences between the two must be because of differences in the ion milling step. In fact, there are several differences between the two types of ion bombardment and these include the angle of incidence, the energy of the impinging ions, and the typical milling times. In traditional surface science experiments the angle of incidence is nearly normal, the ion beam energies are lower (500 eV), and the times are short (1/2 h). When preparing TEM samples, although the angle of incidence is much lower (80° to the normal) the beam energy is typically much higher (5 keV) and also the milling times are an order of magnitude longer. This may account for the differences observed between traditional surface science and TEM-based experiments on oxides.

CHAPTER 4

Surface Structure, Morphology, and Thermodynamics of Reconstructions on $SrTiO_3$(111)

4.1. Introduction

$SrTiO_3$ is a prototypical representative of a large class of materials known as perovskites. Perovskites have a stoichiometry of ABO_3, where A represents an alkali or alkaline earth and B represents a transition metal. Perovskites and the related structure A_2BO_4 are important technologically in a wide range of fields and together represent one of the most frequently studied and well characterized oxide systems. $SrTiO_3$ itself has application in photoelectrolysis (Lo and Somorjai, 1978), as a channel layer in metal-insulator-semiconductor field effect transistors (Shibuya et al., 2004), and as a substrate for growth of high T_c superconducting thin films (Agrawal et al., 1992) and nonvolatile random access memories (Zurbuchen et al., 2001). Additionally, it is used as a model system for other oxides of the perovkite structure, which have application in heterogeneous catalysis (Misono and Mizuno, 1997), optoelectronics, and magnetic storage (Asthagiri et al., 2003).

Bulk $SrTiO_3$ is an elegant structure consisting of a simple cubic lattice (a=3.09 Å) of strontium with a titanium in the body center and oxygen at the face centers, forming an octahedron in the center of a unit cell (Figure 4.1). Stacking along [111]

can be described (Figure 4.2) as alternating layers of SrO_3^{4-} and Ti^{4+}, where the subscript denotes the number of atoms in the surface unit cell and the superscript denotes the charge on each layer, assuming an ionic model.

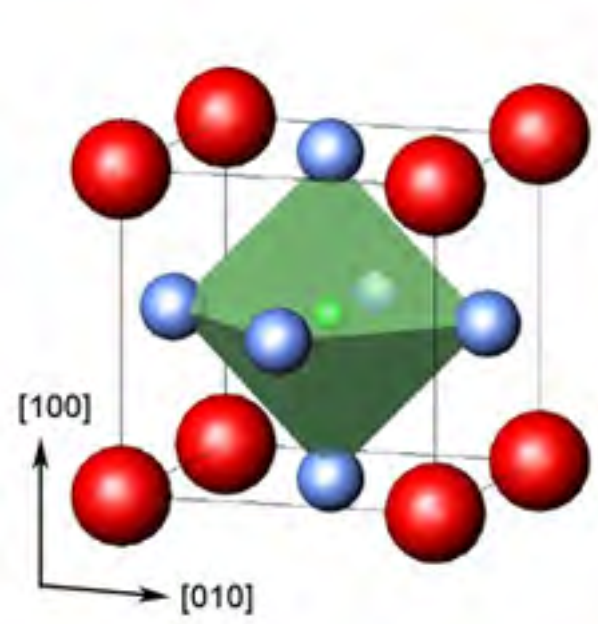

Figure 4.1. Bulk structure of the perovskite $SrTiO_3$; the Ti octahedra is shown.

$SrTiO_3(111)$ is considered by classical electrostatic arguments to be a polar surface and therefore unstable due to the diverging electrostatic surface energy from the presence of a non-zero dipole moment in all of the repeat units of the structure along [111] (Pojani, 1999). Nevertheless, these surfaces have been obtained experimentally and therefore the macroscopic dipole moment must be stabilized by

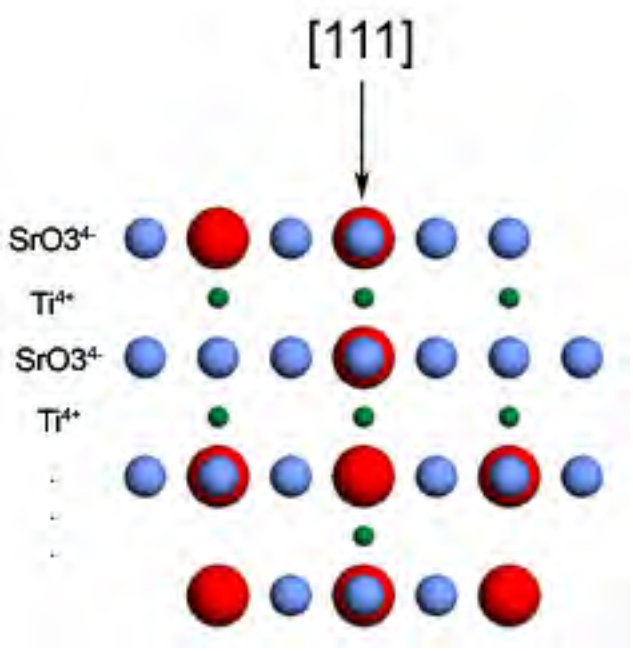

Figure 4.2. Stacking along the [111] direction of $SrTiO_3$ can be described as alternating layers of SrO_3^{4-} and Ti^{4+}.

one of the following mechanisms (Noguera, 2000), depending on the preparation conditions:

- Change in surface stoichiometry—One or more layers has a stoichiometry differing from that of the bulk, which leads to reconstruction or faceting (depending on how the surface atoms order).
- Adsorption of charged adatom—Adsorbed foreign atoms or ions, usually residual from the experimental setup, provide charge compensation.

- Modification of the surface electronic structure—On stoichiometric surfaces, electron redistribution in response to the polar electrostatic field may result in charge compensation.

A wide body of both theoretical and experiment work has focused on the nature of the (001) and (110) surfaces (to a lesser extent) under a wide range of preparation and treatment conditions, but a comparatively small amount of study has been directed at the (111) surface. As seen in Table 4.1, only morphologies, surface unit cell periodicities (not structures), and bulk-terminated structures have been observed on this surface. There has been no full structure solution published on a $SrTiO_3$(111) surface reconstruction.

In the work by Tanaka and Kawai (1996), a $\frac{\sqrt{6}}{2}$a (0.48 nm, approximately $\frac{\sqrt{3}}{2}$ of the (1x1) spacing) surface periodicity was observed after annealing for 1 min at 1180 °C in UHV (1x10^{-8} Torr oxygen). Following annealing at 1200 °C for 1 min, a structure with periodicity of $(\frac{2}{3})\frac{\sqrt{6}}{2}$a coexisting with $\frac{\sqrt{6}}{2}$a was observed, however this appears to be transient and annealing at 1220 °C for 1 min in UHV again produces a structure with the $\frac{\sqrt{6}}{2}$a spacing. Based on step-height measurements in the STM, a bulk-like termination of Ti was assigned to the structure annealed at 1220 °C and a bulk-like termination of SrO_{3-x} was assigned to the structure annealed at 1180 °C. There is no postulation as to the termination of the transient structure annealed at 1200 °C.

In the study by Sigmund et al. (1997), samples were annealed at 950 °C for 2 h in UHV (7.5x10^{-9} Torr total pressure) and exhibited LEED patterns with

Table 4.1. Previous Studies of the $SrTiO_3$(111) Surface.

Reference	Preparation Methods	Observed Surface	Methodology
Tanaka (1996)	1180 °C, UHV, 1 min 1200 °C, UHV, 1 min 1220 °C, UHV, 1 min	$\frac{\sqrt{3}}{2}$ w/ SrO_{3-x} outerlayer $(\frac{2}{3})\frac{\sqrt{3}}{2}$ $\frac{\sqrt{3}}{2}$ w/ Ti outerlayter	STM, RHEED
Sigmund (1997)	950 °C, 7.5x10^{-9} Torr, 2 h	2-fold periodicity, weak 6 fold Ti-terminated	STM, LEED, AES
Sekiguchi (1998a,b) Nb-doped	1000 °C, O_2 flow, 10 h 1000 °C, air, 5 h 1000 °C, Ar flow, 10 h	(1x1) Trench structure Sierpinski gasket (1x1) SrO_x islands	RHEED, AFM

"pronounced 2-fold and weaker 6-fold periodicity." The authors posit that the surface in this case is Ti-terminated based on AES measurements but there has been no complete surface structure calculation.

The thorough AFM morphological studies by Sekiguchi et al. (1998a, 1998b) are the most similar to the conditions used to prepare the samples in the present work so particular attention will be paid to their results. After annealing single crystals at 1000 °C for 10 h in a flow of oxygen, a so-called (1x1) trench structure was observed where triangular "dents" initially formed (1 h) and then coalesced (5 h) until their sides aligned along a straight line (10 h). In the case of annealing in a flow of Ar at 1000 °C for 10 h, a (1x1) structure with a morphology of wide triangular terraces was observed, however these terraces were observed to be much flatter than those observed following oxygen flow. The structure coarsened with time, and after 5 h the final structure was reached and was proceeding to grow. Following annealing at 1000 °C in air, a complex morphology of self-similar triangles similar to the fractal known as Sierpinski's gasket was observed after 5 h of annealing. The fractal dimension of this phase appears to coarsen with time, and this paper conjectures based on the observed morphology that two kinds of nucleation must have occurred on this surface.

The motivation of the present work is to investigate the surface of $SrTiO_3(111)$ in a series of carefully controlled experiments aimed at determining the atomic structure, morphology, and thermodynamic properties following ion bombardment

and annealing treatments. We hope to be able to extend the observations on $SrTiO_3$(111) to other perovskite systems and possibly to polar surfaces in general.

4.2. Sample Preparation and Surface Morphology

TEM samples were prepared as outlined in Chapter 2. Annealing temperatures ranged from 800-1150 °C. All of the samples where diffraction data was collected (for use in Direct Methods) were annealed for 5 h. Samples undergoing a second anneal were annealed between 2-5 h to prevent coarsening and loss of electron transparent regions. In order to investigate the kinetics of the surface phase transitions, one sample was annealed for only 0.5 h and another was annealed for 10 h. Samples were annealed in a tube furnace which was exposed to ambient air or sealed and supplied with a continuous flow of 50 sccm (as output by flowmeters and detected with an oil bubbler) gas. The atmosphere inside of the tube furnace ranged from 100% O_2 flow to 100% Ar flow and points in-between. Ambient air was simulated using 20% O_2 with a balance of either Ar or N_2, and it was found that the system behaved the same in all three cases (real air, oxygen balance argon, or oxygen balance nitrogen).

The sample annealed at 800 °C for 5 h in air showed only bulk-allowed diffraction spots (there were only very faint reconstruction spots) and the morphology of the sample was rounded in nature and did not have flat terraces or the familiar microfaceted edges typically seen in $SrTiO_3$(001) and (110) samples that have equilibrated (Erdman 2002; Subramanian 2005). A second annealing treatment of

the same sample at 850 °C for 2.5 h again showed faint reconstruction spots in the TEM diffraction pattern. The surface morphology (Figure 4.3) was indicative of a sample that had not yet recovered from ion beam damage, however diffuse thickness fringes appeared indicating that the surface was on its way to that point. Surface recovery is indicated by the disappearance of bend contours which are replaced by flat terraces, step bunching, and microfaceting near the edge. A fresh

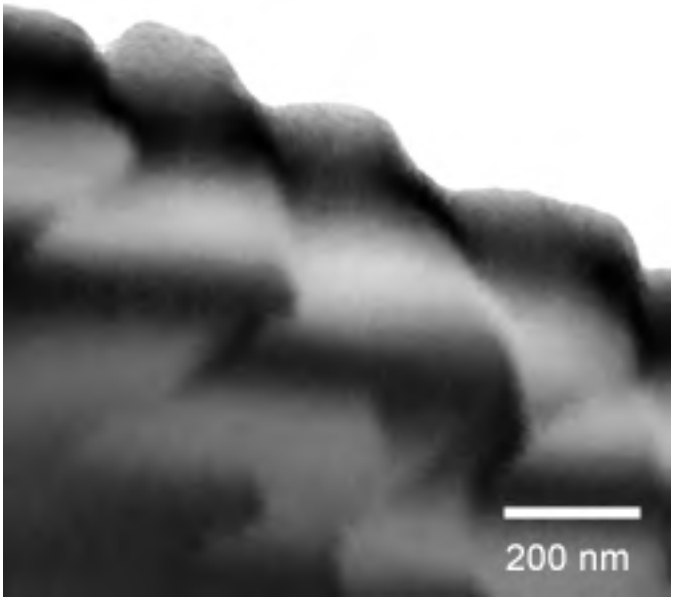

Figure 4.3. Morphology of $SrTiO_3$(111) sample after annealing at 800 °C for 5 h followed by annealing at 850 °C for 2.5 h in air.

sample which was annealed at 850 °C for 5 h in air showed bright surface spots, indicating that a minimum temperature for recovery of ion beam damage and formation of a surface reconstruction on $SrTiO_3$(111) is near 850 °C.

Samples annealed at temperatures of 850 °C and higher for 5 h in any of the atmospheres mentioned above showed clear indication of surface reconstruction as seen in the TEM diffraction patterns. All of these surfaces showed similar morphologies of large flat terraces, step bunching along [110], and microfaceting near the sample edge, however the size and shape of the facets and terraces varied somewhat from sample to sample. Unlike in the work of Sekiguchi et al. (1998a, 1998b), we did not observe a clear trend of surface morphology with annealing atmosphere. For example, Figure 4.4 shows nearly perfectly triangular shaped terraces, and Figure 4.5 shows the 60 and 120° terraces which are typical of the other samples observed (which are likely a result of the coarsening of triangular shaped terraces which join together). It is our belief that in the present work, the exact shape of the terraces is an artifact of the sample preparation process (how long the sample was ion milled) as well as the sample miscut (which is a combination of the native miscut of the as-received crystal as well as the miscut introduced in the dimpling process), and this is why the morphology of each sample is slightly different. In other words, samples which have large flat areas may show triangular facets while those with steeper shapes will show terraces similar to Figure 4.5. The overarching trend, nevertheless, is consistent in all the samples. The terraces observed have edges showing 60 or 120 ° degree angles which are consistent with faceting along <110> which is the direction of closest contact of atoms in the (111) plane. In contrast to the morphology of the hematite samples,

which were quite inconsistent (Chapter 3), the morphology of the $SrTiO_3$ samples are consistently similar within a very narrow range of shape constraints.

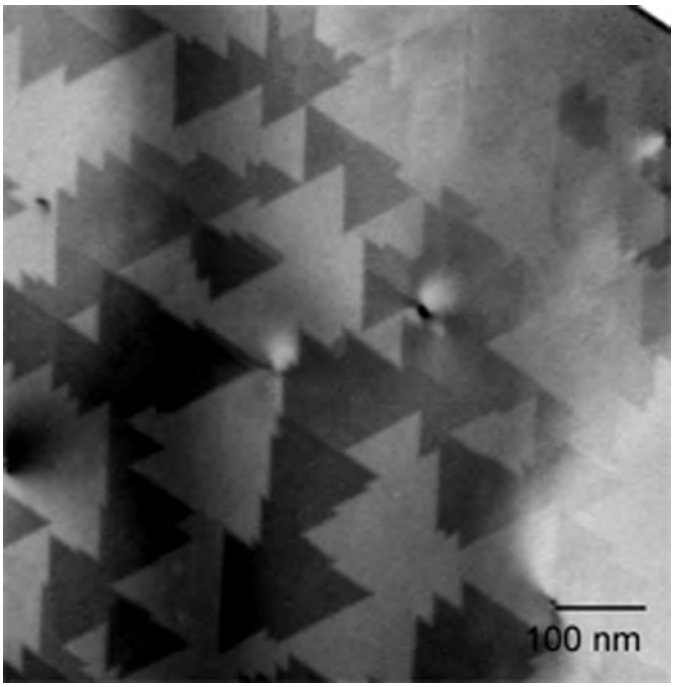

Figure 4.4. Morphology of $SrTiO_3$(111) sample after annealing in air. Large triangular terraces can be seen, however it is impossible to tell from this image if the terraces protrude above or below the surface of the sample. Note: the sample is relatively flat in the viewing window presented.

Although the morphology of the $SrTiO_3$(111) surfaces appears to be invariant of annealing atmosphere, the surface crystal structures observed on these samples are not. In fact, the surface reconstructions obtained following argon ion bombardment and annealing treatments are directly dependent on the annealing time, temperature and oxygen (partial) pressure. In the next several sections a variety

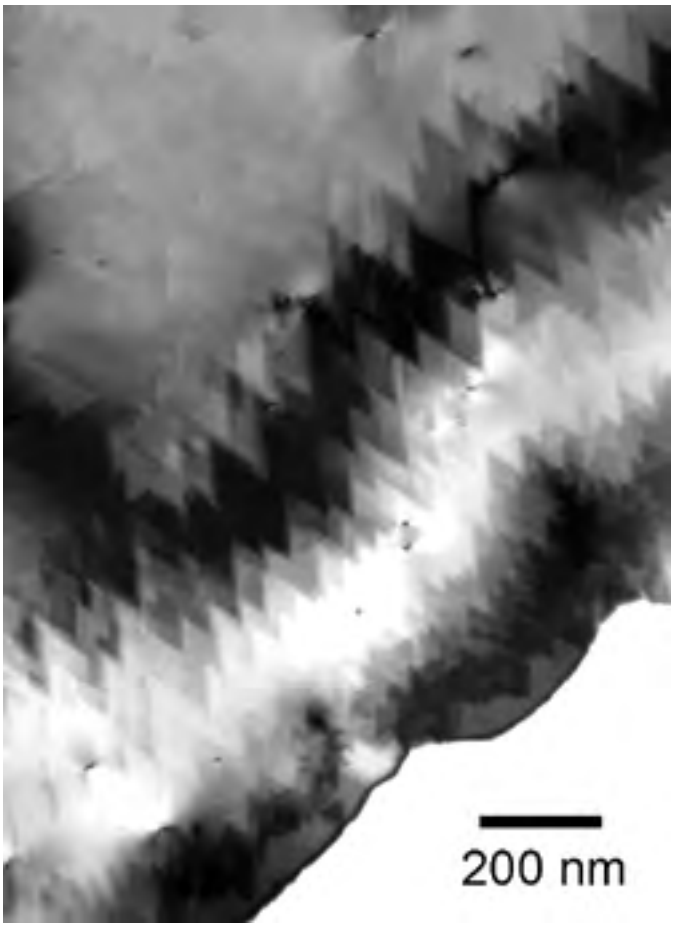

Figure 4.5. Morphology of $SrTiO_3$(111) sample after annealing in air. This is more typical of the morphologies observed, with large irregularly shaped terraces populating the sample surface. These terraces show faceting along the ¡110¿ directions hence the prominent 60 and 120° angles observed.

of surface reconstructions observed in this system will be discussed in detail, including the (3x3), $\frac{9}{5}$x$\frac{9}{5}$, (6x6), and (4x4). In addition to their crystal structure, the reconstructions will be discussed in terms of their thermodynamic stability and also the reaction kinetics of their phase transformations.

4.3. $SrTiO_3$(111)-3x3 Surface

The $SrTiO_3$(111)-(3x3) reconstruction was solved using diffraction data from a sample annealed at 1050 °C for 5 h in air. As clearly seen in the TEM diffraction pattern (Figure 4.6), the (3x3) surface diffraction spots are present along with another set of spots (arrowed) which can be indexed to a ($\frac{9}{5}$x$\frac{9}{5}$) reconstruction. Based on the arrangement of spots in the diffraction pattern (Figure 4.7), a two domain structure consisting of ($\frac{9}{5}$x1) and (1x$\frac{9}{5}$) domains is ruled out.

These ($\frac{9}{5}$x$\frac{9}{5}$) spots are unique in that they are not coincident on a $SrTiO_3$ (1x1)-type spot until the 3rd repeat of the (1x1) unit cell. This implies that this reconstruction is incommensurate on $SrTiO_3$(111). Interestingly, however, the spots from the (3x3) and ($\frac{9}{5}$x$\frac{9}{5}$) reconstructions are coincident on a rather prominent set of spots which for clarity sake will be termed alpha, or "α" spots. The $SrTiO_3$(111)-(3x3) spots are coincident with the alpha spots at repeats of 5, while the ($\frac{9}{5}$x$\frac{9}{5}$) are coincident with the alpha spots at repeats of 3. In other words, the $SrTiO_3$(111)-(3x3) reconstruction can also be thought of as a (5x5) reconstruction of the α phase, while the $SrTiO_3$(111)-($\frac{9}{5}$x$\frac{9}{5}$) spots can be thought of as a (3x3) reconstruction of the α phase:

$$(3x3)_{STO} \equiv (5x5)_{\alpha}$$
$$(\tfrac{9}{5}x\tfrac{9}{5})_{STO} \equiv (3x3)_{\alpha}$$

The $SrTiO_3$(111)-(3x3) TEM diffraction patterns *always* show both the (3x3) and ($\frac{9}{5}$x$\frac{9}{5}$) spots. There has never been a case in this study where one was observed

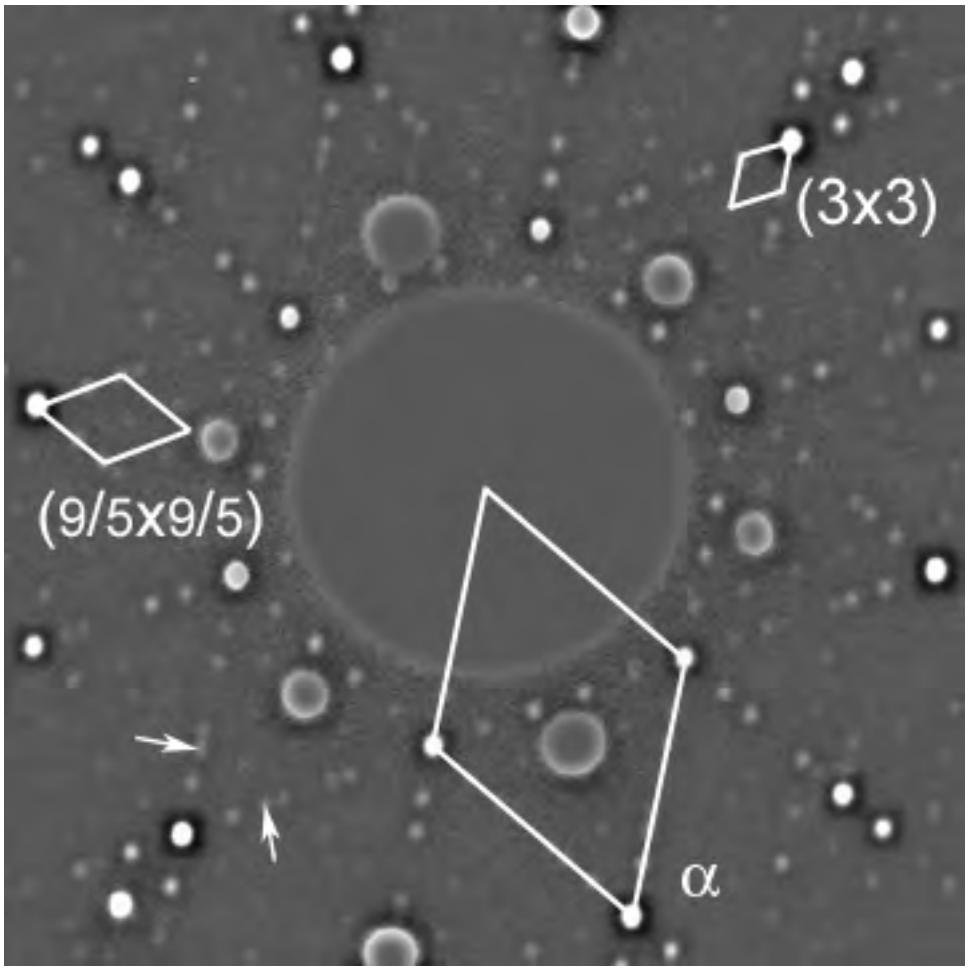

Figure 4.6. Diffraction pattern from the $SrTiO_3$(111)-(3x3) reconstruction. The (3x3) unit cell is indicated along with the unit cell of the ($\frac{9}{5}$x$\frac{9}{5}$) reconstruction, which is always coexisting. The α phase unit cell is also shown.

without the other. While it is possible that the two sets of spots are actually representative of a large supercell, there is experimental evidence in the literature to support the fact that the spots are from two different phases. The studies by Sekiguchi et al. (1998a, b) found that annealing in air for 5 h produced a surface

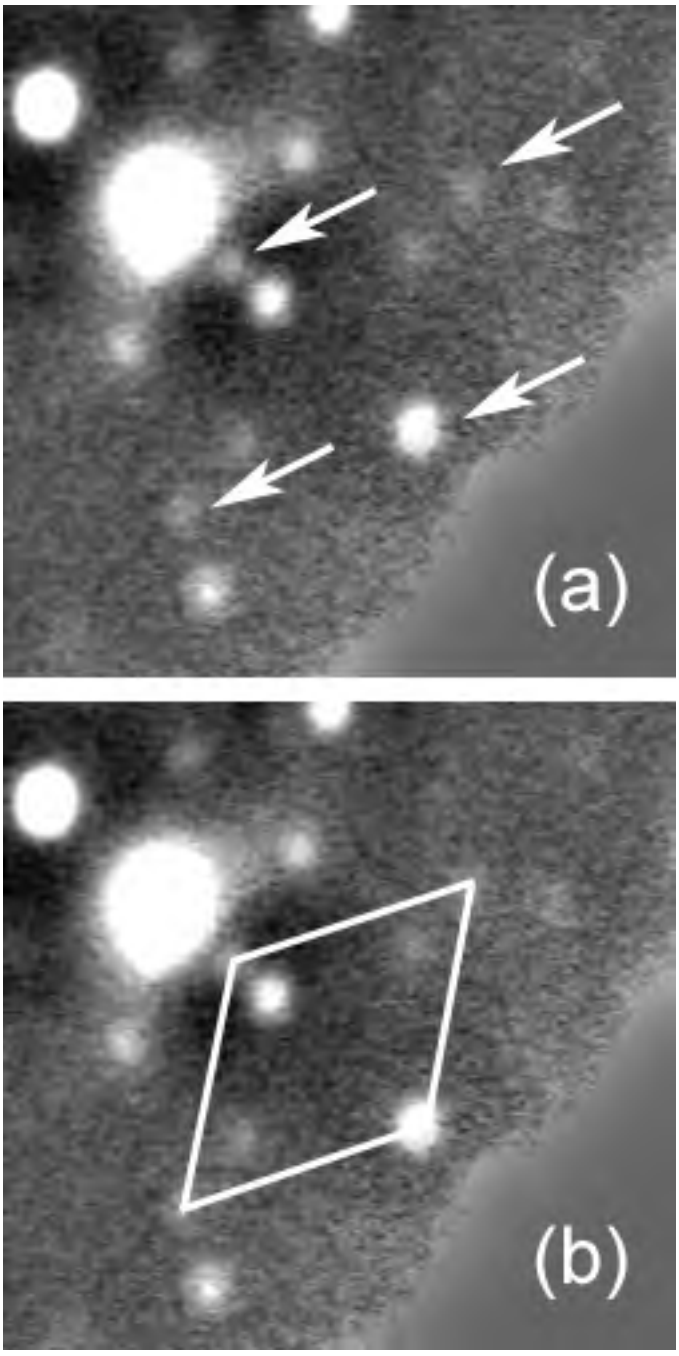

Figure 4.7. Inset of the $SrTiO_3$(111)-(3x3) pattern in Figure 4.6 showing the ($\frac{9}{5}$x$\frac{9}{5}$) spots (arrowed) more clearly. The presence of all four of the spots denoting a single ($\frac{9}{5}$x$\frac{9}{5}$) unit cell indicates this is not a supercell or otherwise multi-domain structure.

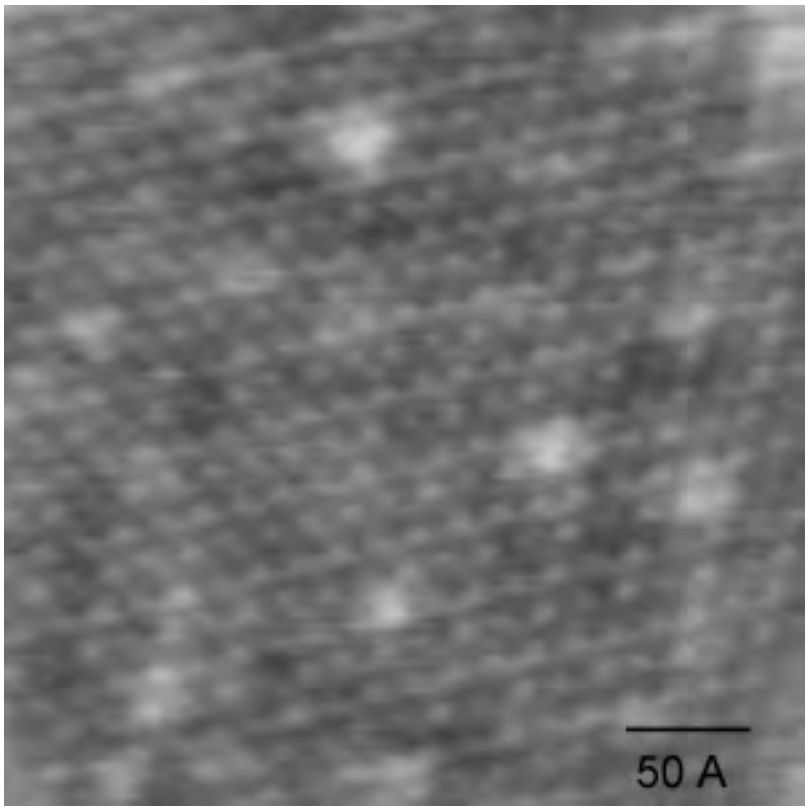

Figure 4.8. DF image of the $SrTiO_3$(111)-(3x3) surface. The image has been Wiener and high pass filtered to remove random noise and enhance contrast. The 16.56 Å (3x3) unit cells can clearly be resolved.

where two kinds of nucleation must have occurred. In other words, there are two phases on the surface. In additon, there is no TEM evidence of what would be 50 Å domains (and therefore very easy to resolve in a DF image) from a supercell in any images taken of this surface. In contrast, the 16.56 Å (3x3) domains are readily observed in a DF image of this surface (Figure 4.8).

4.3.1. $SrTiO_3$(111)-(3x3) Structure Solution

Surface diffraction data from the (3x3) reconstruction contained 64 independent reflections (to 1.0 Å resolution) in *p6mm* (Patterson) symmetry. Direct Methods analysis was performed on this data set and the best resulting scattering potential map is shown in Figure 4.9a. The map shows only a partial surface structure, which is typical of surface data due to missing measured reflections (reflections are not measured when they overlap with the bulk or another domain), measurement error, and dynamical scattering. Subsequent refinement within the Peaks2D program, employing difference map techniques, were able to complete the structure (Figure 4.9b) giving an R-factor of 0.24 and a χ^2 value of 1.69.

In two dimensions, the (3x3) reconstruction is an elegant structure consisting of what appear to be "truncated octahedra" (half of an octahedral unit from the parent $SrTiO_3$, viewed along the [111] direction–see Appendix B) and rather straight lines of alternating Ti-O along the <110> directions, with large triangular pits of Ti and O vacancies tiling the structure in a regular pattern. Interestingly, triangular pits were found to stabilize the polar ZnO (0001) surface (Kresse et al, 2003), and were energetically more favorable than isolated vacancies for a given stoichiometry. When the structure is depicted with the half-octahedra visible, as in Figure 4.10, it resembles a fractal image of self-similar triangles known as Sierpinski's gasket. The Sierpinski's gasket motif (Figure 4.11) was observed as a

morphology on samples annealed in air for 5 h (Sekiguchi et al., 1998a, 1998b), which is incidentally the same conditions used to obtain the (3x3) reconstruction.

This (3x3) structure, when considered in 2-dimensions (not bonded to the bulk), is non-stoichiometric and slightly oxygen rich, with 18 Ti atoms and 22 O atoms per 2-d surface unit cell. It is interesting to note that there is no strontium in the surface reconstruction, which is consistent with other observations in this system (Erdman 2002, Subramanian 2005) on samples prepared in a similar way. Considering the surface as an isolated entity for purposes of calculating coordination, bonding, and stoichiometry is not realistic. The accurate way of evaluating those parameters is to consider how the (3x3) surface reconstruction would be bonded to bulk $SrTiO_3$(111).

4.3.2. Registry on the Bulk

There are four ways in which to bond the (3x3) surface reconstruction to the bulk $SrTiO_3$ lattice, where (s) denotes a surface layer and (b) denotes a bulk layer stacked along the [111] direction:

(1) Stacking the surface layer onto the bulk with opposing sequential layers and a Ti termination (Figure 4.12a). This leads to a stacking sequence of $\cdots SrO_3$(b)-Ti(b)-O(s)-Ti(s)

(2) Stacking the surface layer onto the bulk with opposing sequential layers and O termination (Figure 4.12b). This leads to a stacking sequence of $\cdots$ Ti(b)-SrO_3(b)-Ti(s)-O(s)

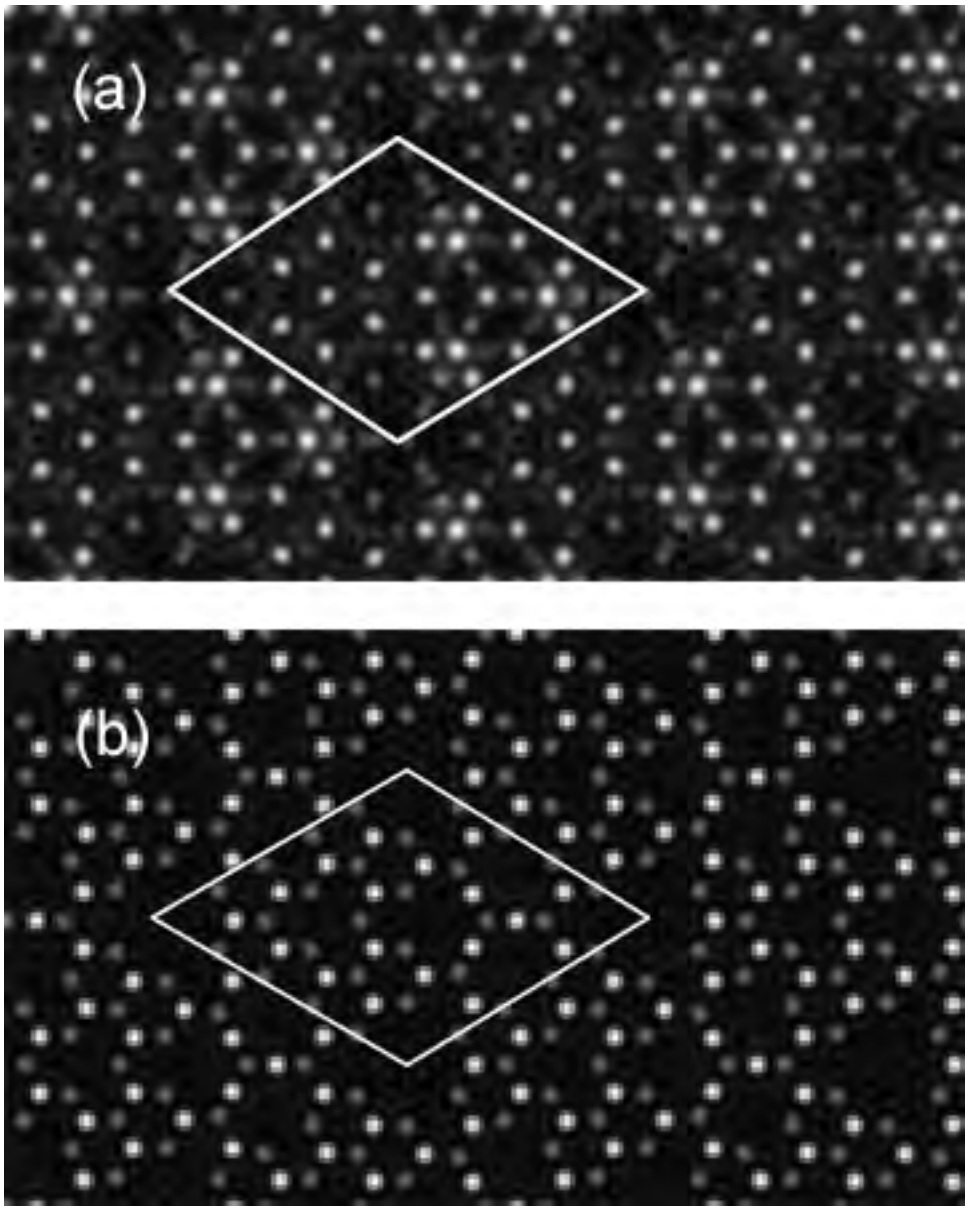

Figure 4.9. $SrTiO_3$(111)-(3x3) surface structure solution; a single (3x3) unit cell is shown. (a) Direct methods scattering potential map. (b) Structure solution following structure completion and refinement. In map (b), the bright spots represent Ti atoms, and the dim spots represent O atoms.

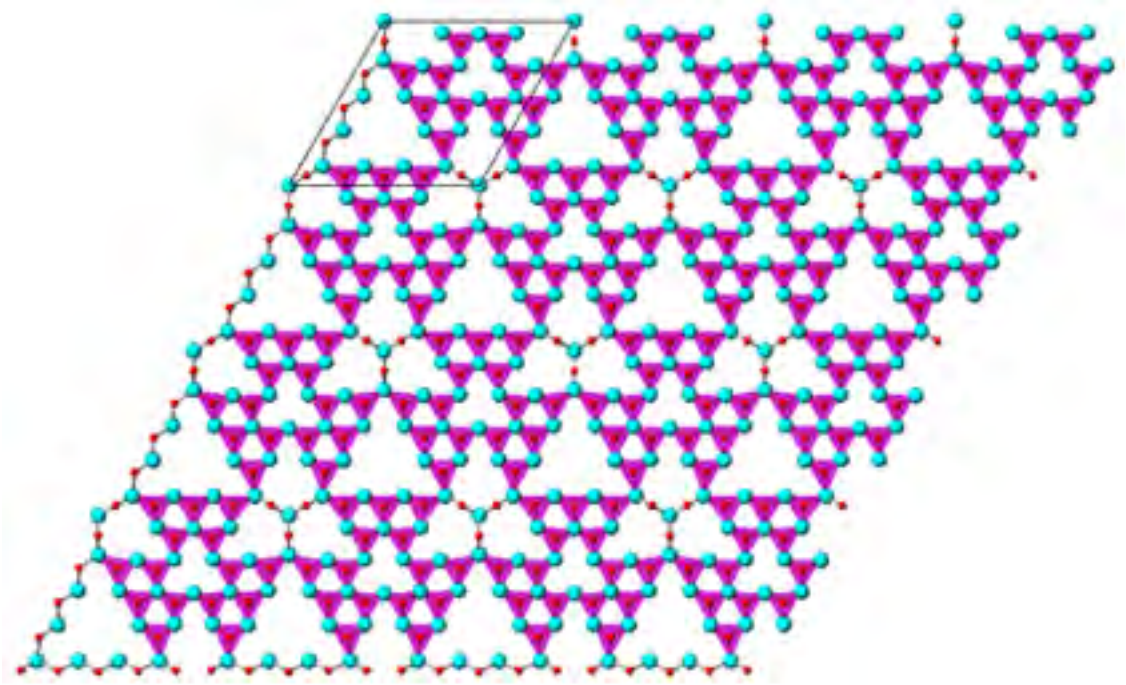

Figure 4.10. The 2-dimensional (3x3) structure viewed with the Ti octahedra shown. The structure resembles the fractal known as Sierpinski's gasket.

(3) Stacking the surface layer onto the bulk with adjacent like layers and a Ti termination. This leads to a stacking sequence of

$\cdots$Ti(b)-SrO_3(b)-O(s)-Ti(s)

(4) Stacking the surface layer onto the bulk with adjacent like layers and an O termination. This leads to a stacking sequence of

$\cdots$$SrO_3$(b)-Ti(b)-Ti(s)-O(s)

Of these four possibilities, options (3) and (4) do not make intuitive "chemical sense" because each has adjacent like-layers (Ti-Ti or O-SrO_3), where realistic

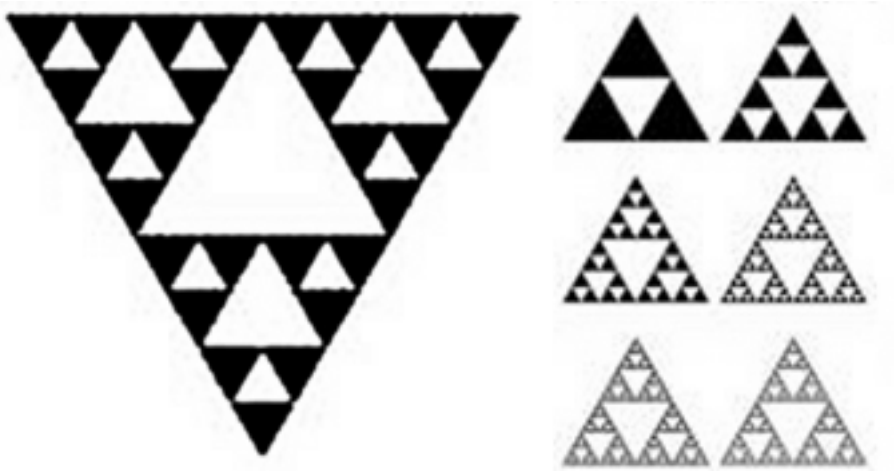

Figure 4.11. Fractal image known as Sierpinski's gasket which consists of a regular pattern of self-similar triangles.

bonding and coordination constraints can not be satisfied. Only structures with alternating layers, options (1) and (2) above, will be considered further.

The Ti-terminated (option 1) surface is a complicated structure where of 18 surface titanum, three are 2-coordianted and the rest are 3-coordinated (truncated octahedra). Of the nine bulk titanium (in a (3x3) unit cell) bonded to surface oxygen, three are 5-coordinated forming a distorted square pyramid, three form tetrahedra, and the remaining three form very distorted octahedra. In contrast, the oxygen terminated (option 2) surface is a simpler solution. In this case, all of the surface titanium are tetrahedrally coordinated and all of the bulk titanium retain their octahedral coordination (they are bonded to bulk oxygen layers above and below). What appeared to be truncated octahedra or octopolar units on the surface in a 2-dimensional projection are in fact in 3-dimensions corner sharing

tetrahedra viewed on end, when the bonding to the bulk is considered. In this (3x3) structure, the surface titanium atoms are sitting nearly on top of a bulk oxygen atom. This is not a problem because truncated octahedra, truncated octopolar units, and tetrahedra viewed on end all appear similar in projection (Appendix B). In other words, what first appeared (in 2-dimensions) to be octahedrally coordinated bulk-like titanium atoms are in fact tetrahedrally coordinated titanium at the surface. Viewing the structure as it is bonded to the bulk with the Ti tetrahedra filled in (Figure 4.13) reveals that 13 of the 18 surface titanium are corner sharing tetrahedra with the 3-fold axis in the plane of the surface, 2 are in slightly tilted edge sharing tetrahedra, and the remaining 3 are in nearly 90° rotated corner sharing tetrahedra. Preliminary DFT (Wein2K) refinements of the O terminated structure showed the out of plane structure becoming more planar, with the outermost Ti and O layers compressing relative to the bulk interlayer spacing (Figure 4.14). A more accurate DFT refinement of the oxygen terminated structure is currently ongoing and is the subject of future work.

In order to determine the (unknown) oxidation state of the surface titanium atoms, a technique known as the Ewald sum (Ewald, 1921) is employed. It is the accepted technique for counting electrostatic charge in a periodic system. In an Ewald summation, the charge in an individual layer is split in two and half is combined with that of the layer below. This new spatial arrangement of positive and negative charges is then treated as a single crystallographic element surrounded by like copies of itself. The entire system is then neutral. This implies for the case

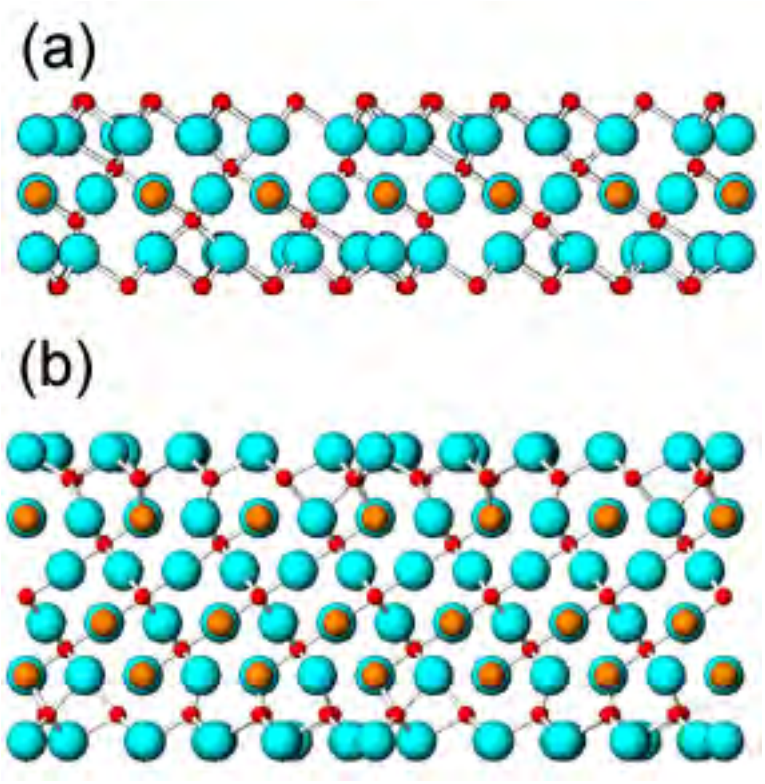

Figure 4.12. Two chemically realistic stacking sequences for bonding the (3x3) reconstruction to the bulk. (a) Stacking sequence with a Ti outer layer. (b) Stacking sequence with an O outer layer.

of the Ti terminated surface, summation of the charge from the surface titanium, the surface oxygen, and one half of the next bulk titanium layer must equal zero. Since a single (3x3) unit cell covers the same area as nine bulk unit cells, the bulk stoichiometry will be enumerated with a larger unit cell. The Ti terminated surface (option 1, Figure 4.12a) stacking can be written as

$$\cdots 9(SrO_3)\text{(b)-9Ti(b)-22O(s)-18Ti(s)}$$

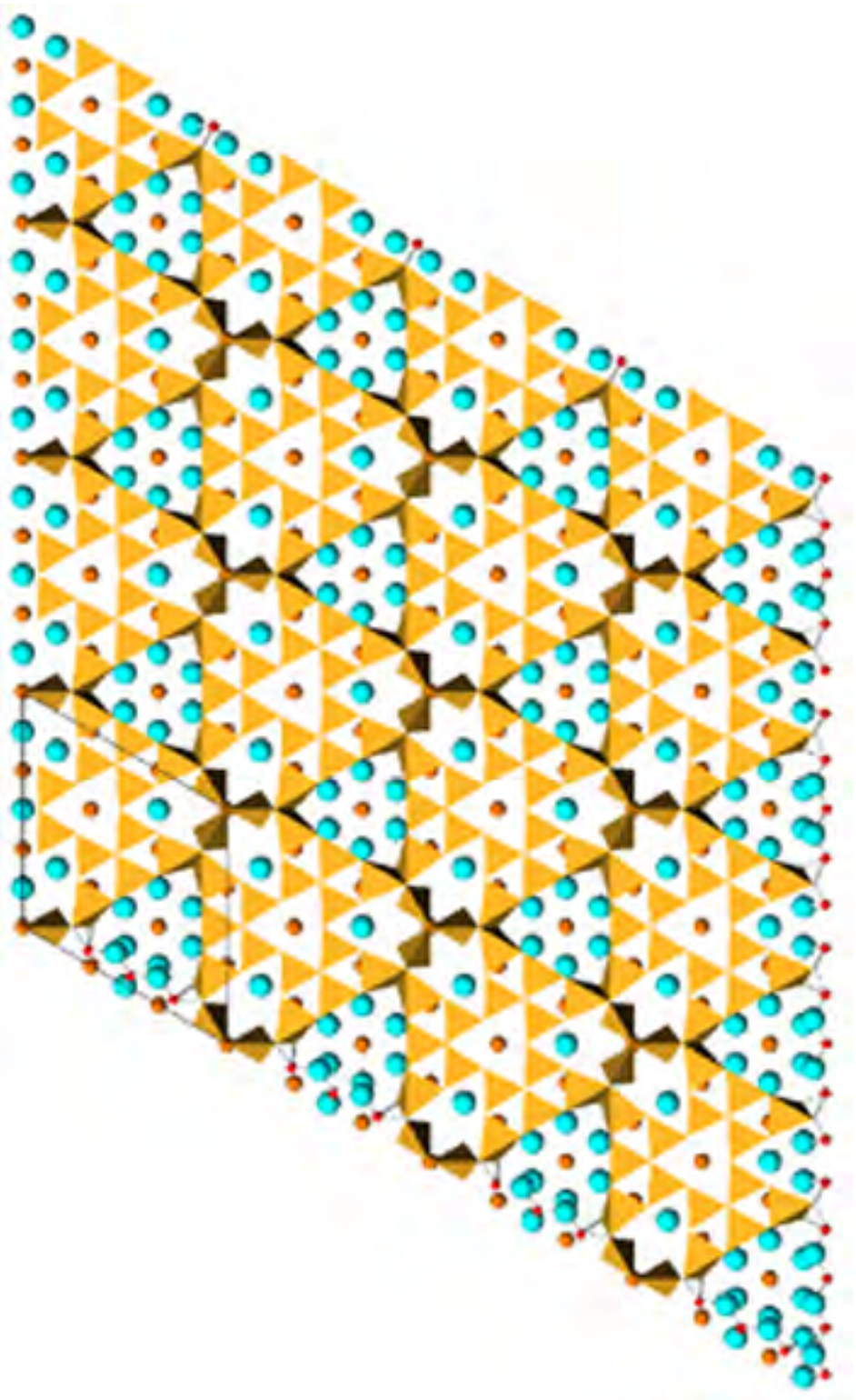

Figure 4.13. The full 3-dimensional (3x3) structure viewed with the surface tetrahedra shown. This is the structure when bonding and coordination to the bulk (SrO_3 layer below is shown) are considered.

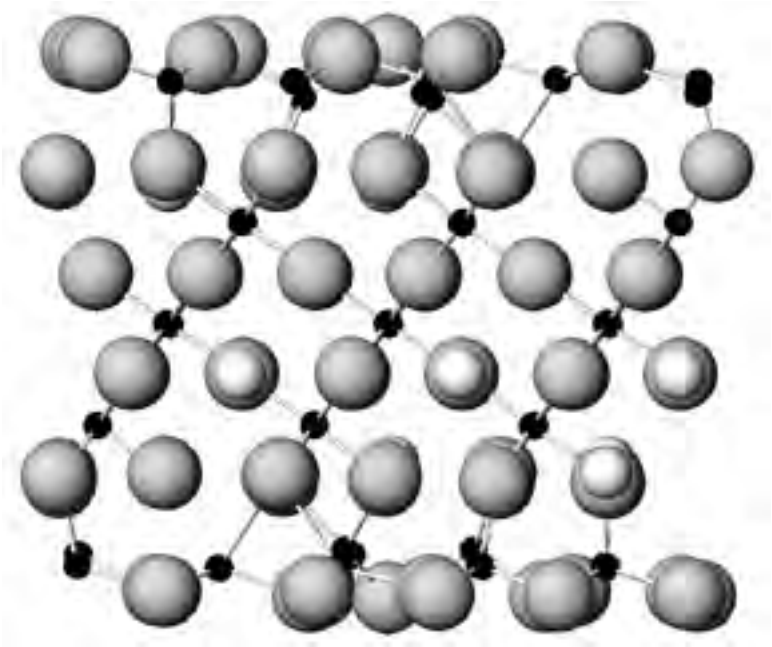

Figure 4.14. The oxygen terminated surface following preliminary structure refinement using the Wein2K code. The distance between the Ti and O layers in the reconstruction has decreased relative to the bulk interlayer spacing.

Let x be the (unknown) oxidation state of the surface Ti atom. According to the Ewald sum,

$$18(x) + 22(2^-) + \frac{1}{2}(9)(4^+) = 0$$

Here x, the oxidation state of the surface titanium in the titanium-terminated structure is equal to +1.44 in a simple valence charge analysis. Alternatively, the calculated values of the Mulliken and Bader charges for bulk Sr, Ti, and O (Carrasco et al., 1995) can be used to determine the oxidation state of the surface titanium in the (3x3) structure. For the Mulliken charge analysis, the oxidation

state is +1.95, where the Bader charge analysis gives +1.93. In any case, the surface Ti is significantly reduced from its bulk value of +4.0 which is not likely under the experimental conditions used here (Reed, 1971). The O terminated surface (option 2, Figure 4.12b) stacking can be written as

$$\cdots 9\text{Ti(b)-}9(\text{SrO}_3)\text{(b)-}18\text{Ti(s)-}22\text{O(s)},$$

where summation of the charge from the surface oxygen, surface titanium, and one half of the next bulk SrO_3 layer must equal zero:

$$22(2^-) + 18(x) + \frac{1}{2}(9)(2^+) + \frac{1}{2}(9)(3)(2^-) = 0$$

In this case, the Ewald sum for simple valence charge analysis gives an oxidation state of +3.44 for the surface titanium. If Mulliken or Bader charges are used, the value rises to +3.98 or +3.93, respectively. The oxidation state of the surface titanium in the oxygen terminated surface is closer to the values observed experimentally under annealing conditions similar to those used here (Adachi et al., 1999; Göman et al., 2005; Lo and Somorjai, 1978). Therefore, the oxygen terminated surface is determined to be correct for this structure.

4.3.3. α Phase Structure Solution

Considering the postulation that the $SrTiO_3$(111)-(3x3) reconstruction consists of two domains which can be thought of as a (3x3) and (5x5) reconstruction of some

phase we call α ($d_{1\times1}$=3.03 Å), the question remains: what is this α phase and does it make sense within the context of the known (3x3) structure?

The alpha-phase spots in the TEM diffraction pattern are consistent with TiO_y ($a \sim 4.29\mathring{A}$), which is a nonstoichiometric compound with rock salt structure and a (1x1) spacing of 3.3 Å in the (111) plane. Direct Methods analysis of this structure is not a good way to proceed; there are only two symmetry independent reflections and the phases can be worked out essentially by hand by making use of the triplet invariant (Giacovazzo, 1998; Marks 2004). In this case, the structure is essentially an octopolar unit (a titanium surrounded by 6 atoms in projection), consistent with our interpretation that the α phase is similar to TiO_y of the rock salt structure. Further evidence that this interpretation is meaningful is that the titanium and oxygen lattices in the (3x3) structure map approximately to those in the rock salt structure, with the regular array of missing Ti and O accounting for the larger unit cell. If the missing Ti and O in the (3x3) structure were filled in, the resulting lattice would have TiO stoichiometry and the rock salt structure. Fittingly, the smallest commensurate lattice between TiO_y(111) and $SrTiO_3$(111) is a (5x5), which is exactly the relationship indicated in the diffraction pattern.

The (3x3) structure can be thought of as an reconstructed interface where the diffraction pattern in Figure 4.6 is from a multilayer structure. The $SrTiO_3$(111)-(3x3) is a way to interface two different structures: Ti-rich rock salt, where the octopolar units are corner sharing, and $SrTiO_3$, where the octahedral units in a layer do not touch. Since the $(3x3)_{STO}$ can be equivalently indexed to a (5x5)

reconstruction of TiO_y, this interfacial layer is commensurate with both structures. We propose that the multilayer structure consists of bulk $SrTiO_3$ with a (3x3) surface reconstruction which is covered in some small areas with a (mono)layer of either TiO_y which is reconstructed (Figure 4.15a) to TiO_y(3x3) or simply a (mono)layer of the TiO_y(111)-(3x3) (Figure 4.15b). The TiO_y(3x3) is the $SrTiO_3$-($\frac{9}{5}$x$\frac{9}{5}$) phase and this hypothesis explains why it is incommensurate on $SrTiO_3$—because it is not bonded to $SrTiO_3$ directly. We suspect the areas of TiO_y are small because we have not been able to image them. We suspect that they are monolayers because the $\frac{9}{5}$x$\frac{9}{5}$ spots are faint in the diffraction pattern and there is no evidence of double diffraction coming from a thick layer. It is impossible to tell directly from the diffraction pattern if any unreconstructed TiO_y exists on the surface because the strong TiO_y spots displayed in the diffraction pattern can also be accounted for by the recurring structural motif of truncated octahedra or octopolar units displayed by the reconstructions (n.b. a truncated octopolar unit of rock salt looks the same as a truncated octahedra in projection–see Appendix B). Nevertheless, if any TiO_y was present, the (111) surface is polar so it will be reconstructed. With or without it, in any case, the argument is the same. Currently, we have no direct experimental evidence as to where and why these small areas of TiO_y form. One supposition could be small fluctuations in the surface composition as a result of ion milling lead to segregation. Another could be that the TiO_y phases form near step edges or at other high energy sites. Yet another is that the TiO_y is an electron irradiation induced phase that forms inside of the microscope during the course of

examination. There are several examples in transition metal oxides where phases similar to TiO_y that are not otherwise stable in the bulk have been observed to grow epitaxially on surfaces under electron irradiation (Buckett, 1991). In other words, it may be that the $(\frac{9}{5}x\frac{9}{5})$ is an electron radiation induced phase and not a result of thermal annealing. One question to answer would be after very long annealing times (15 h, 24 h), higher temperatures, or even longer times under the electron beam does the TiO_y phase stay the same, disappear, grow thicker, or increase in fractional coverage? Is the intensity ordering of the beams the same or different, which would indicate a change in composition?

4.4. $SrTiO_3$(111)-6x6 Surface

The $SrTiO_3$(111)-(6x6) reconstruction for which diffraction data were collected and analyzed was obtained by annealing samples in a 50 ccm flow of oxygen for 5 h at 1050 °C. The TEM diffraction pattern of this structure, unlike that of the (3x3), has no extra spots and consists of only spots showing (6x6) periodicity (Figure 4.16). This reconstruction has a large 33.12 Å unit cell which can readily be resolved in a dark field image (Figure 4.17). In *p6mm* symmetry, this structure has 244 *symmetry independent* reflections (1 Å resolution) and so the data set for this structure is quite large. Direct Methods analysis is ongoing however based on the maps that have been observed so far, we can say that this structure appears very similar to the (3x3) in that the surface titanium are surrounded by 3-fold symmetric oxygen forming a truncated octahedra in 2-dimensions (or tetrahedron viewed on

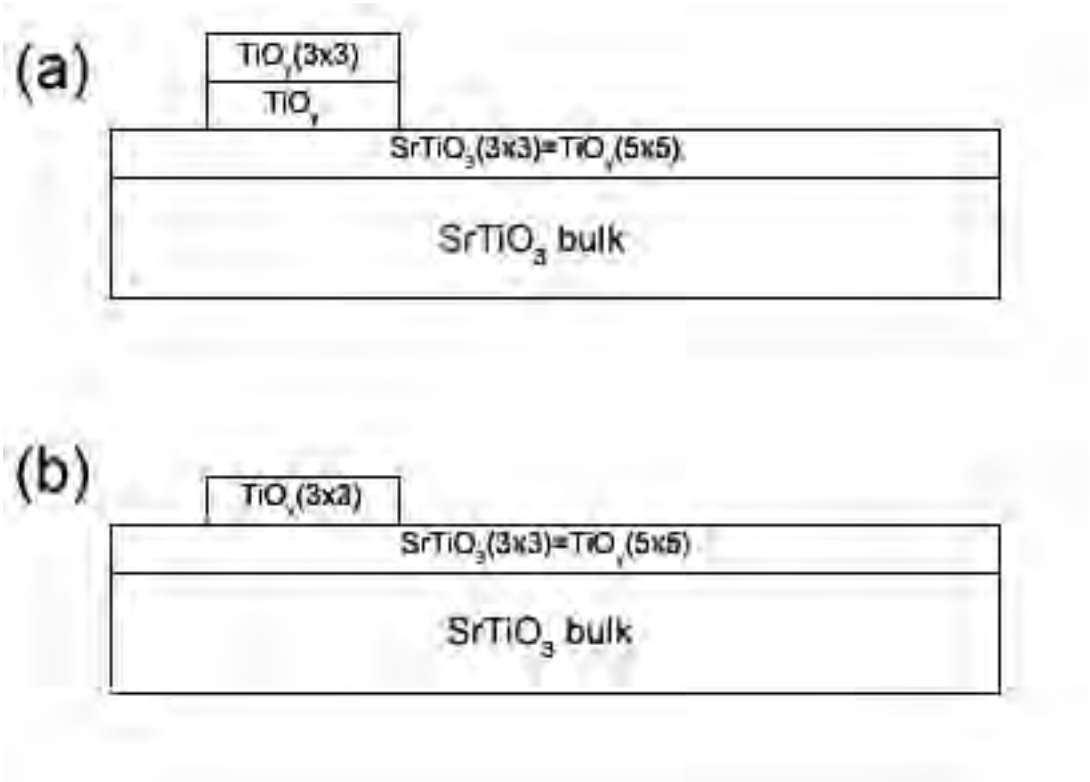

Figure 4.15. Schematic representation of the proposed $SrTiO_3$ "multilayer" surface. Bulk $SrTiO_3$(111) is covered in a (3x3) reconstruction everywhere. It is topped with either (a) a TiO_y layer which has itself reconstructed (it is a polar surface) or (b), simply a (3x3) reconstruction of TiO_y.

end, in 3-dimensions). Like the (3x3), we believe that the (6x6) may also be a reconstruction of TiO_y. Looking carefully at the diffraction pattern from the (6x6) structure, it is apparent that the bright 5(h,k)-type TiO_y spots which were present in the (3x3) are present also in the (6x6) (Figure 4.16, arrowed). This means that in the same way that the $SrTiO_3$(111)-(3x3) can be looked at equivalently as a

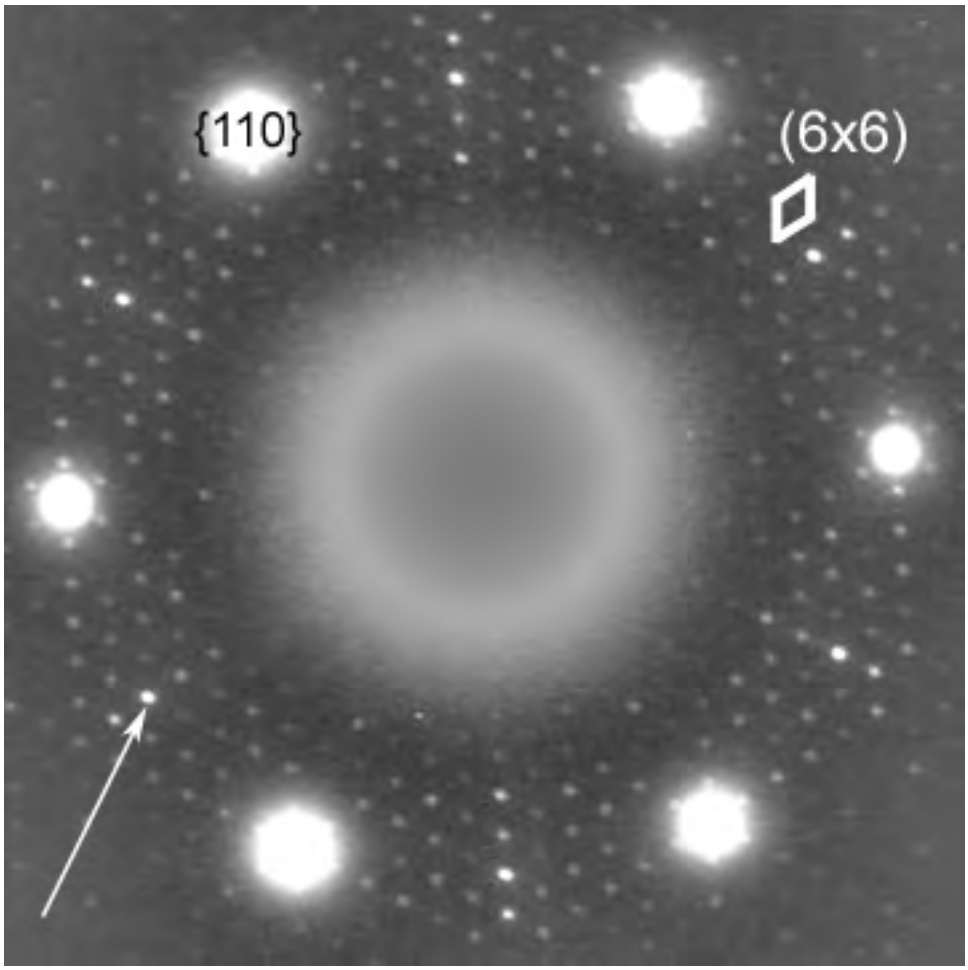

Figure 4.16. Diffraction pattern of the $SrTiO_3$(111)-(6x6) reconstruction. A bright α-type spot is arrowed.

(5x5) reconstruction of TiO_y, the $SrTiO_3$(111)-(6x6) can be looked at as a (10x10) reconstruction.

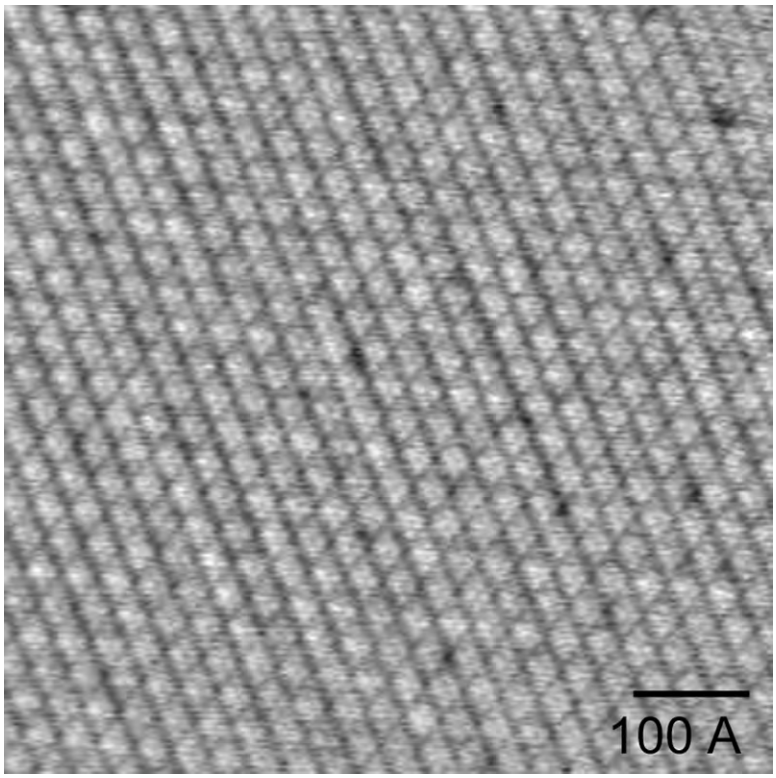

Figure 4.17. Dark-field image of the (6x6) reconstruction clearly showing the 33.12 Åunit cell. Note the low density of point defects in this image.

4.4.1. Scaleable Structures

An $SrTiO_3$(111)-(4x4) reconstruction was observed on two different TEM samples following annealing for 5 h in a furnace borrowed from a collaborator. The termocouple reading was 1050 °C, however, this experiment was never able to be reproduced in the Carbolite furnace used for all of the other samples in this study. We believe this is due to differences in ramp rate and/or temperature calibration. Nevertheless, as seen in Figure 4.18, this reconstruction shows prominent α spots

as well as faint spots indicative of an α-(3x3) reconstruction in the exact same way as the $SrTiO_3$-(3x3). In this case, however, the alpha phase (1x1) spacing is slightly reduced (a=3.15 Å), indicating that the TiO_y phase lattice parameter changes slightly with the unit cell size (which presumably is a function of annealing conditions and therefore composition although there is at present no direct evidence of this). Similar to the (3x3), (6x6), and $\frac{9}{5}$x$\frac{9}{5}$, the (4x4) can be thought of as a reconstruction of a TiO_y-like phase. Specifically, the $SrTiO_3$-(4x4) is equivalent to a (7x7) reconstruction of the TiO_y phase. In fact, we propose that all of the $SrTiO_3$ reconstructions observed in this study can be thought of in terms of reconstructions of TiO_y, and we believe it is likely that all of them are scaleable structures similar to the way that the dimer-adatom-stacking fault (DAS) structure of Si(111)-(7x7) is scaleable (Zhao et al., 1998, 2000).

Research is ongoing to determine the exact surface structure and therefore the scalability of all of the observed reconstructions, however the initial scattering potential maps from direct methods are promising in that all of the structures show the archetype motif of a central titanium atom surrounded by 3-fold symmetric oxygen which are presumed to be tetrahedral units viewed on end in three dimensions when bonding to the bulk is considered. This indicates that unlike the non-polar (001) surface (Erdman et al., 2002, 2003), octahedra do not move as a cohesive unit upon surface reconstruction on the (111) polar surface of $SrTiO_3$.

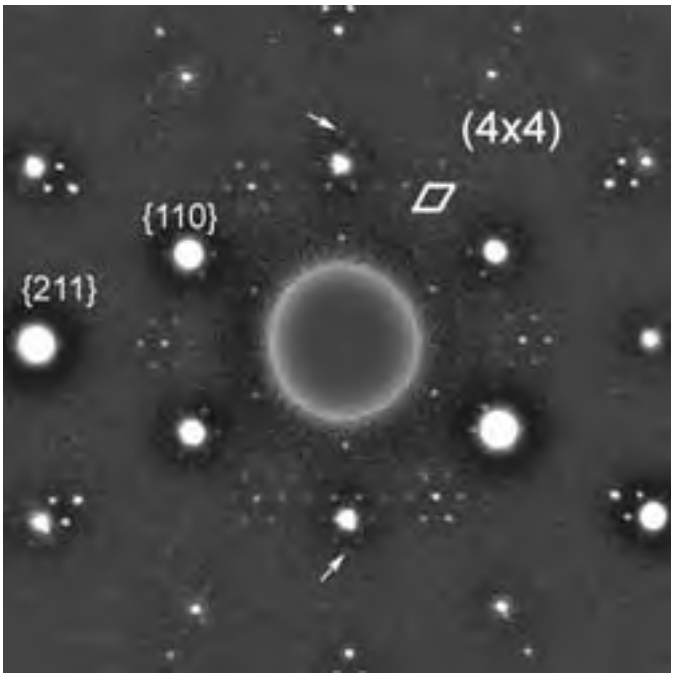

Figure 4.18. Experimental diffraction pattern for the (4x4) structure. The (3x3) alpha-phase spots have been indicated with an arrow.

4.5. Thermodynamics and Kinetics

The temperatures, oxygen partial pressures, and annealing times reported for the various reconstructions in the previous section were not the only conditions where these reconstructions were observed. Rather, the reported temperatures and times were those used to collect the diffraction data sets used in solving the surface structure. All of the structures are observed over a wide range of temperatures, oxygen partial pressures, and even annealing times, hinting at the thermodynamic stability of the structures and also the kinetics of the phase transformations. The

experimental data is summarized in Table 4.2 and discussed in detail in the following sections. For simplicity sake, the (3x3)+($\frac{9}{5}$x$\frac{9}{5}$) will hereafter be referred to as (3x3) except in cases where mention of the ($\frac{9}{5}$x$\frac{9}{5}$) is explicitly necessary for understanding.

Table 4.2. Summary of the current annealing studies of $SrTiO_3$(111).

Time	Temperature	Atmosphere	Observed Reconstruction
5 h	1050 °C	pO_2=1.0	(6x6)
5 h	1050 °C	pO_2=0.8	(6x6)
5 h	1050 °C	pO_2=0.6	(6x6), (3x3)
5 h	1050 °C	pO_2=0.4	(3x3)
5 h	1050 °C	pO_2=0.2	(3x3)
5 h	850 °C	pO_2=0.2	(6x6)
5 h	900 °C	pO_2=0.2	(6x6), (4x4)
5 h	925 °C	pO_2=0.2	(6x6), (3x3)
5 h	950 °C	pO_2=0.2	(3x3)
5 h	1125 °C	pO_2=0.2	(3x3)
5 h	1000 °C	pO_2=0.5	(6x6)
5 h	1100 °C	pO_2=1.0	(6x6)
5 h	1150 °C	pO_2=1.0	(6x6), (3x3)
0.5 h	1050 °C	pO_2=0.0	(6x6)
10h	1050 °C	pO_2=1.0	(3x3)

4.5.1. Equilibrium Structures, Phase Stability, and Thermodynamics

All of the diffraction data sets mentioned previously were collected following annealing for 5 h at 1050 °C, with varying oxygen partial pressure. Since the structures had in fact been observed over a wide range of temperatures and oxygen partial pressures (following annealing for 5 h), an experimental surface phase diagram could be constructed. A requirement for constructing an equilibrium phase diagram is that one must verify that thermodynamic equilibrium has been achieved. If equilibrium has been reached, a sample with a given structure should transform to another structure simply by changing the conditions (temperature or the oxygen partial pressure) of the anneal. This process should be reversible, and true if approached from either direction (in other words, approached from both high and low temperatures). Our results are as follows:

- The (6x6) formed after 5 h at 1050 °C in O_2 flow transforms readily to the (3x3) following annealing for only 2.5 h in air.
- The (3x3) formed after 5 h at 1050 °C in air does not transform to the (6x6), even following annealing at 1 atm of pure oxygen for 7.5 h.

These results indicate that the (6x6) and (3x3) structures may not be in equilibrium despite the fact that they were treated at nearly 1/2 T_m for 5 h. This is an interesting contrast to the previous studies on the (001) surface, where the observed structures were assumed (based on their reproducibility) to be in thermodynamic equilibrium following annealing at 1/3 - 1/2 T_m for 0.5-5 h (Erdman et al, 2002).

In order to further investigate the stability of the structures, several samples were treated at the same temperature (1050 °C) but the annealing times were changed (Figure 4.19). It was found following annealing in an argon flow for 30 min a (6x6) reconstruction was formed (whereas annealing for 5 h in air produces the (3x3)). Following annealing for 10 h in a flow of oxygen, the (3x3) was observed (whereas annealing for only 5 h under the same conditions produces the (6x6)). These three experiments indicate that the (6x6) is actually a metastable structure which transforms to the (3x3) with time, where the rate of the transformation is dictated by the partial pressure of oxygen and the temperature. Figure 4.19 shows the transformation rate from the (6x6) to the (3x3) is proportional to temperature and *inversely proportional* to oxygen partial pressure.

The experimental phase diagram (Figure 4.20) to be constructed from the 5 h annealing data in Table 4.2 is therefore a *metastable phase diagram* which can nevertheless provide useful information on the interpretation of this complex system. The pertinent axes in this case are temperature and oxygen partial pressure, as the compositions of all of the phases are unknown at this point. The phase boundary has been indicated and the areas of (3x3) and (6x6) phase stability have been shaded for clarity. Worthy of note are:

(1) Phase boundaries have been narrowly defined in temperature and oxygen partial pressure.

(2) Phase boundary represents a coexistence between (6x6), (3x3), and $\frac{9}{5}$x$\frac{9}{5}$.

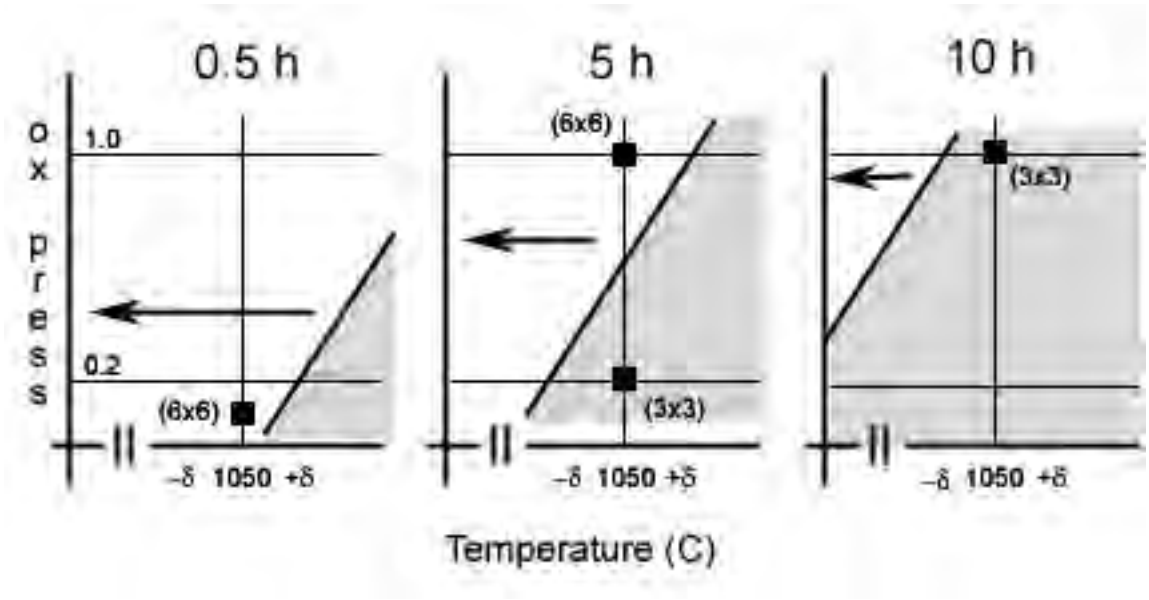

Figure 4.19. Plot of Temperature versus partial pressure of oxygen for three different annealing times. Black squares represent measured experimental data. The boundary between the (6x6) and (3x3) phases in the 5 h anneal is the experimental value; for the 30 min and 10 h anneal the line has been extrapolated. For a given oxygen partial pressure, the phase transition occurs more rapidly at higher temperatures, indicating the current experimental temperatures are in the diffusion-rate limited regime.

(3) For a given temperature (850 °C $\leq$ T $\leq$ 1125 °C) and fixed annealing time (5 h), the (6x6) is stable at higher oxygen partial pressures.

(4) For a given partial pressure (0.2 $\leq$ pO_2 $\leq$ 1.0) and fixed annealing time (5 h), the (6x6) is stable at lower temperatures

Together with the information on the rate of structural transformation as a function of oxygen partial pressure and temperature (rate is inversely proportional to oxygen partial pressure, and proportional to temperature), we interpret (3) and (4) to

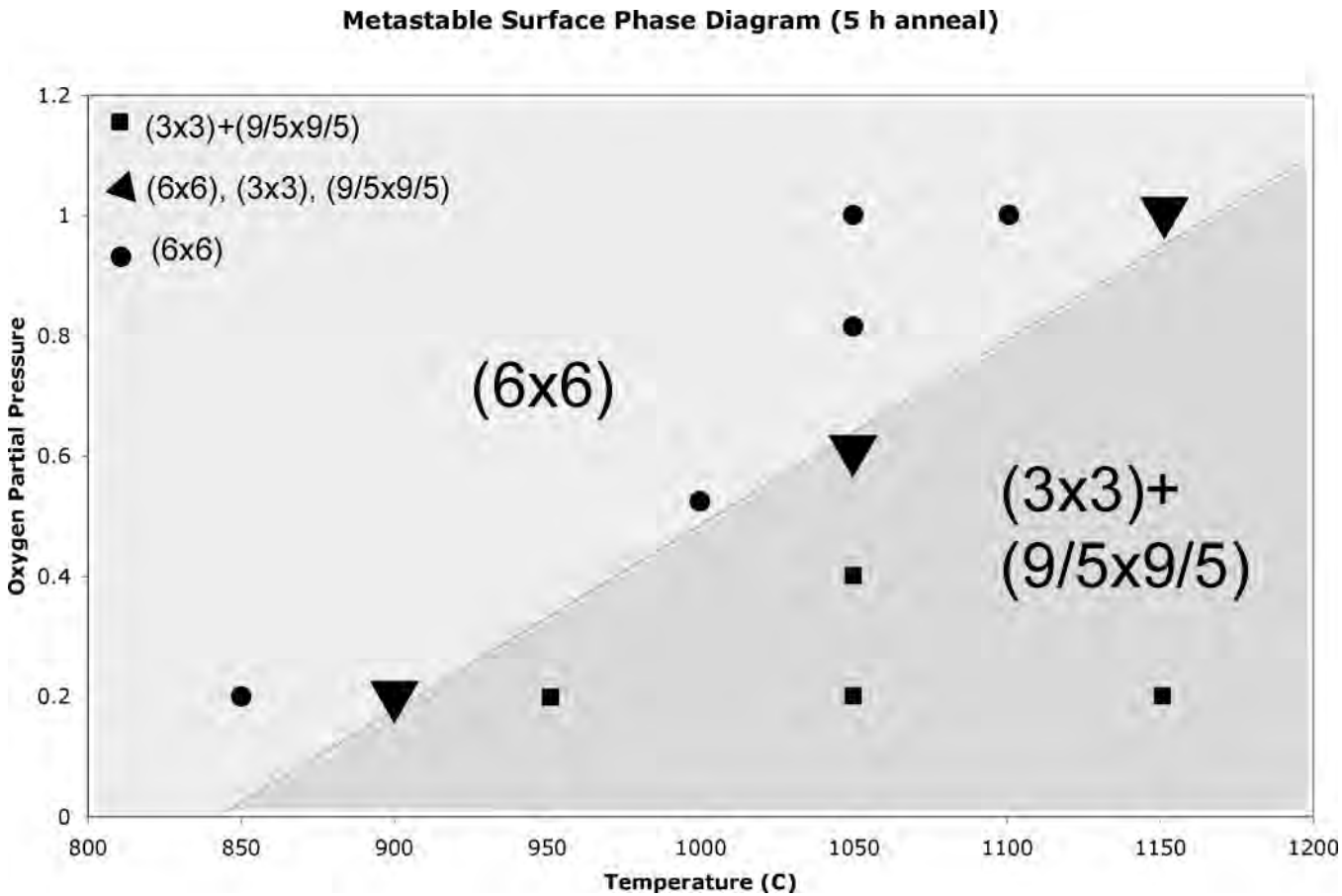

Figure 4.20. An experimental metastable surface phase diagram for $SrTiO_3$ (111) following annealing for 5 h. Small circles indicate the (6x6) reconstruction; small squares indicate coexistance of (3x3) and ($\frac{9}{5}$x$\frac{9}{5}$) reconstructions. The small triangles indicate a three phase coexistance between (6x6), (3x3), and ($\frac{9}{5}$x$\frac{9}{5}$).

mean that the (6x6) is a more oxygen-rich structure and its transformation to the (3x3) is a reduction which occurs by loss of oxygen and is diffusion rate limited. This is consistent with observations of other transition metal oxide systems. For example, Fe_3O_4(magnetite) is more reduced than Fe_2O_3(hematite). In an open thermodynamic system (such as a tube furnace anneal where the pressure of oxygen is constant), Fe_3O_4 is always the high temperature phase except for pressures near 50 atm of oxygen. The reduction of hematite to magnetite at high temperatures was exactly the problem encountered in the optical floating zone furnace for the growth of single crystal hematite from the melt (Section 3.3.3).

This is somewhat counterintuitive when one considers the effect of the initial starting point, that is to say, directly following argon ion bombardment. It is well documented that following argon ion bombardment, transition metal oxides (including $SrTiO_3$) are nonstoichiometric and oxygen deficient (Adachi et al., 1999; Lo and Somorjai, 1978). The samples come out of the PIPS reduced, and our results indicate they are oxidized to (6x6), and then reduced to (3x3) with time. These counter-intuitive observations can be explained by comparing the current results with those of a similar system, TiO_2, and making use of a concept known as "bulk-assisted reoxidation".

Following argon ion bombardment, rutile (TiO_2) samples are well known to be oxygen deficient on the surface. In other words, the surfaces are reduced and therefore Ti-rich relative to the bulk. When heated in oxygen, argon flow, or even UHV (e.g. invariant of atmosphere), a (1x1) surface diffraction pattern is observed

with LEED or TEM (Henderson, 1999; Wang, 2005), indicating that the surface has reoxidized to the bulk stoichiometry. This observation has been explained on the basis of a process known as "bulk-assisted reoxidation", which is where Ti species at the surface of TiO_2 diffuse very rapidly into the bulk driven by a large concentration gradient (Henderson, 1999). In other words, the oxidation occurs not from the gas phase oxygen in the ambient atmosphere but rather from the bulk, where Ti is diffusing away from the surface thereby enriching it in oxygen. The very interesting and convincing study by Henderson shows that the Ti diffusion occurs very rapidly above 700K, and that the surface of TiO_2 can be self-reoxidized in an order of minutes. In terms of $SrTiO_3$, these studies may explain why the (6x6) structure forms initially upon annealing from a reduced sample, invariant of the ambient oxygen partial pressure. Coming out of the PIPS, $SrTiO_3$ samples are reduced and the surfaces Ti-rich. Upon heating, at least in the range $0.2 \leq pO_2 \leq 1.0$, the near surface region is oxidized by self diffusion of either the Ti or O species to form the (6x6) structure. Then, upon further annealing (where there is no longer a huge concentration gradient driving diffusion in the bulk) the structure reduces to the (3x3) at a rate determined by the partial pressure of oxygen in the ambient atmosphere and the temperature. We postulate that the reduction from the (6x6) to the (3x3) involves a net loss of oxygen from the surface and not a gain of titanium since bulk $SrTiO_3$ is stable at the temperatures and oxygen pressures used in this experiment and therefore not a Ti source. Since the rate of

transformation increases with temperature (Figure 4.19), the phase transition is diffusion-rate limited.

While there is no evidence titanium is the rapidly diffusing species in $SrTiO_3$ at low temperatures, our argument would still be valid if the oxygen in the bulk was the rapidly diffusing species. In any case, we posit that the samples are initially oxidized by diffusion from the bulk (independent of atmosphere) in a process known as "bulk-assisted reoxidation", and then reduced in time by loss of oxygen from the surface. A very recent study by Gömann et al. (2005) found that the metastable impact electron spectra (MEIS) for the (111) surface of $SrTiO_3$ annealed in UHV or air for 1 h at 900 °C were nearly invariant, supporting the claim that the ambient atmosphere has little if any effect on the initial annealing behavior.

4.5.2. Kinetics of Phase Transformations

The (6x6) reconstruction is air stable for periods of time on the order of months or longer, so it appears that there is a minumim tempearture for the transformation to the (3x3) to occur in a finite period of time. Together with the data for the samples annealed for 0.5 h and 5 h, this can lead to the construction of an isopressure time-temperature-transformation (TTT) diagram, for example Figure 4.21. This figure qualitatively describes the transformation kinetics of the reaction from the (6x6) to the (3x3)+($\frac{9}{5}$x$\frac{9}{5}$) for a fixed partial pressure of oxygen, although the general shape is valid for any oxygen partial pressures investigated in this study. In fact, many such TTT diagrams could be constructed for all of the oxygen partial pressures

used in this study to create a three-dimensional TTT surface which would describe the reaction kinetics of the system in terms of all of the independent variables.

Figure 4.19 helps to understand whether the current conditions are above or below the "nose" of the TTT diagram. The nose indicates the temperature of the fastest transition as well as defines the border between nucleation controlled regime (above) and diffusion controlled regime (below). If the hypothesis is correct, that is to say the reduction is limited by the loss of oxygen from the surface and is diffusion rate controlled, then the temperatures used in the current study are on the lower side of the nose of the TTT diagram. Experimental evidence in Figure 4.19 agrees, in that it predicts a faster transition time at higher temperatures for a given oxygen partial pressure.

4.6. Phase Coexistence

In order to rule out the possibility of a large supercell on the samples in which (3x3) and (6x6) phases have been observed to coexist (Figure 4.22), imaging of the domain structure is necessary. Figure 4.23a shows a dark field TEM image of a sample annealed at 1050 °C for 5 h in a 50 ccm flow of 60% oxygen and 40% argon. The image represents a sample on which the (3x3) and (6x6) reconstructions have been observed concurrently in the diffraction pattern and are shown in the image to coexist next to each other. The figure clearly shows two domains with different periodicity. Figure 4.23b is an enlargement of the left domain, and clearly shows the 16.56 Å (3x3) lattice. Similarly, Figure 4.23c is an enlargement of the right

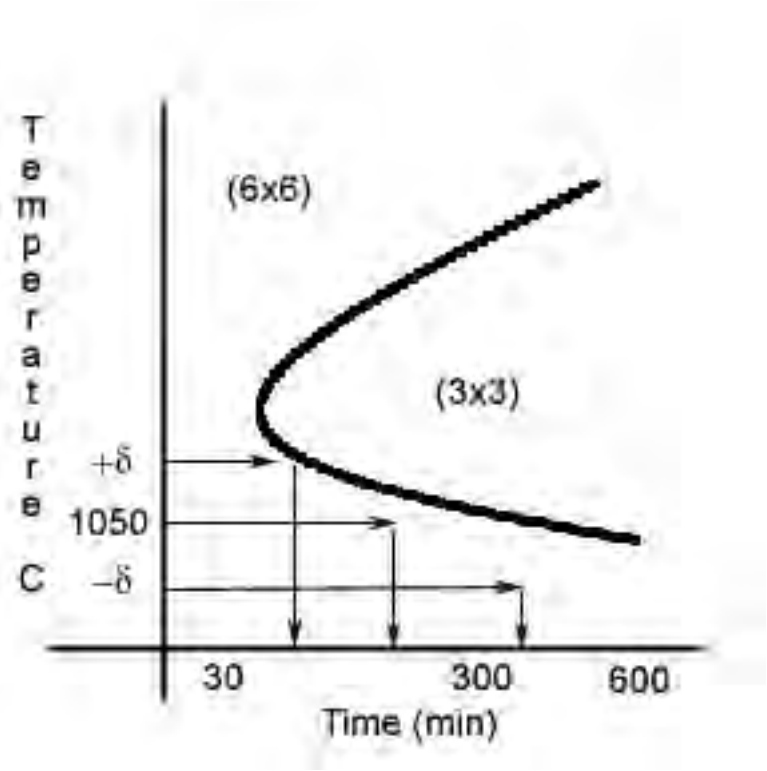

Figure 4.21. Time-temperature-transformation (TTT) diagram for the (6x6) to (3x3) phase transformation.

domain, and clearly shows the 33.12 Å (6x6) unit cell. There is no experimental evidence of a large supercell. In order to remove random (shot) noise and enhance the quality of the image, a soft circular mask was applied (which is why the images seem to have a circle around them) followed by a Weiner filter. From Figure 4.23a, it appears the average domain size of each structure is approximately 50 nm x 50 nm, although this is likely a minimum number as it is difficult to distinguish the edge of the domain in the image because of the transmission geometry (it is difficult to distinguish a domain boundary on the top surface from one on the bottom).

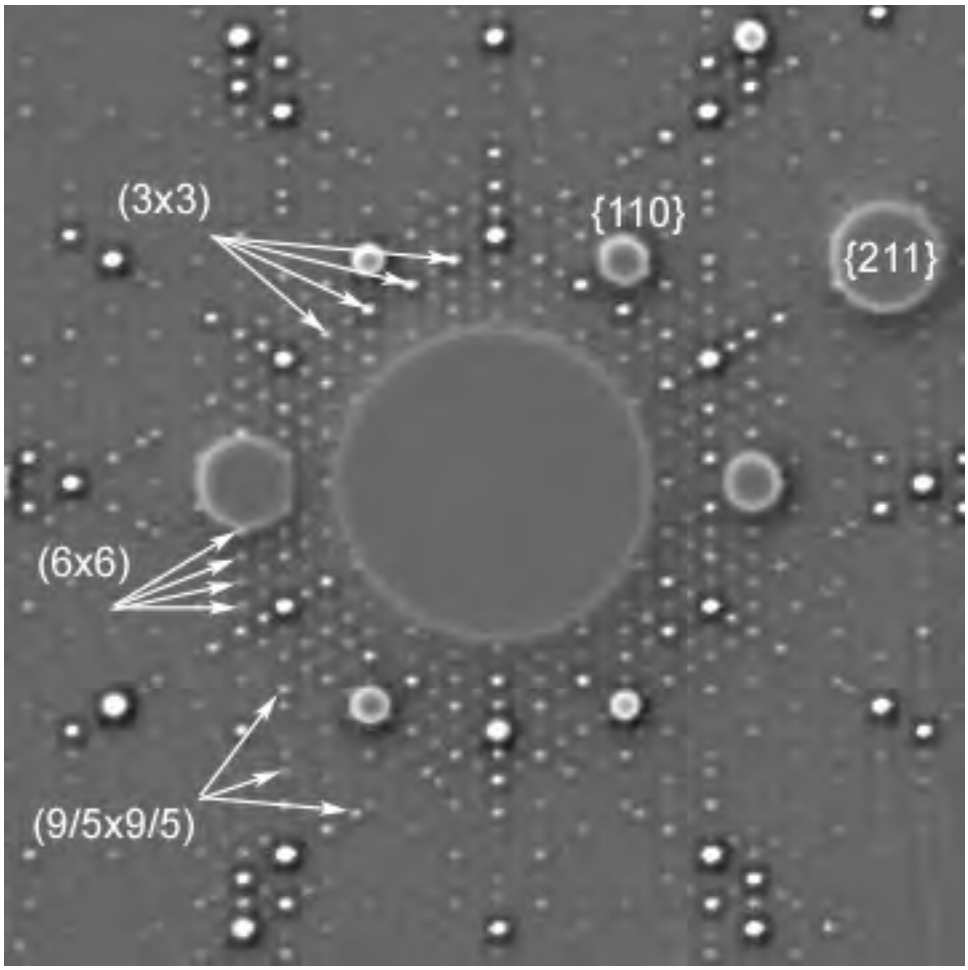

Figure 4.22. Diffraction pattern from a sample annealed in the three-phase region on the metastable phase diagram. Specifically, this sample was treated for 5 h at 1050 °C in a mixture of 60% oxygen and 40% argon. Spots corresponding to (3x3), (6x6), and $\frac{9}{5}$x$\frac{9}{5}$ reconstructions are present.

Since this image is essentially a 5 h time slice for the transformation, it would be interesting to compare domain sizes for the phase coexistence at different annealing times in order to attempt to further understand the transformation kinetics. A

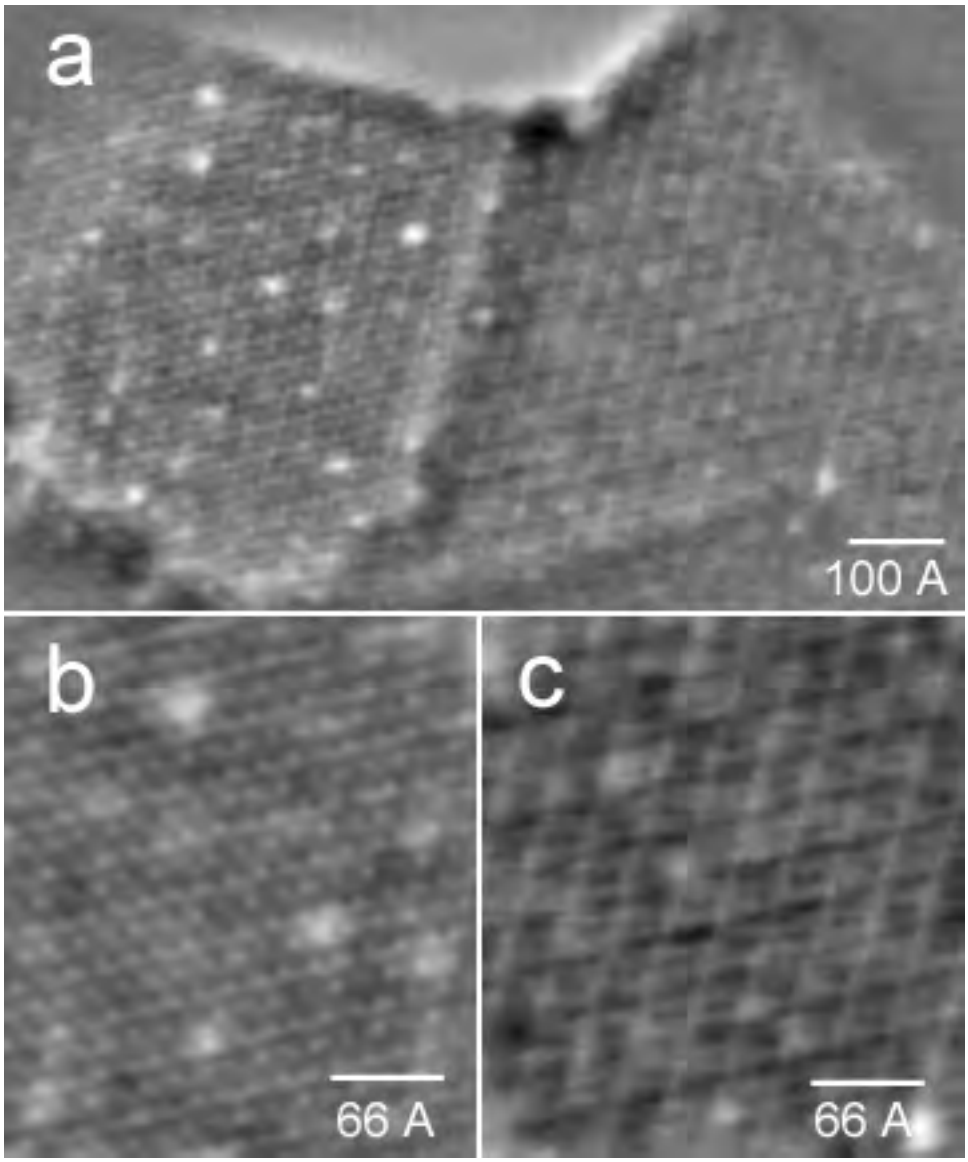

Figure 4.23. (a) Dark-field TEM image of coexisting domains of $SrTiO_3$(111)-3x3 and 6x6 reconstructions. The average domain size is ∼50 nm. Close-up views of the (3x3) domain (b) and (6x6) domain (c) are shown for clarity.

closer look at the images in Figure 4.23b and c shows that the (6x6) domain clearly has less defects than the (3x3) domain (defects are manifested as the small bright spots in the image). It is also interesting to note that in this particular image, there is no evidence of the ($\frac{9}{5}$ x $\frac{9}{5}$) domain which always coexists with the (3x3). As mentioned previously, a supercell has been ruled out for the (3x3)+($\frac{9}{5}$ x $\frac{9}{5}$) structure. One reason for this may be that the image is not in the proper diffraction condition or not of sufficient quality and resolution to be able to resolve the much smaller 9.93 Å domains of the ($\frac{9}{5}$ x $\frac{9}{5}$) reconstruction. Another possibility is that the domains are very small and/or exist only in certain areas of the sample (for example step edges).

CHAPTER 5

Conclusions and Suggestions for Future Work

The present work has served to enhance the understanding of model transition metal catalytic oxide surfaces following argon ion bombardment and annealing treatments. In addition to providing reliable recipes for the preparation of various reconstructions on polar oxide surfaces, this work has served to further the understanding of crystal growth in the optical floating zone furnace, a technique which has great potential for providing catalysis researchers with large high quality single crystals needed for model studies.

Specifically, a new flux system ($CaFe_4O_7$) for the single crystal growth of α-Fe_2O_3 has been discovered which makes use of the optical floating zone furnace and peritectic reaction in a new way. For the first time, a single crystal has been grown using a flux containing an adventitious component (Ca) which was not incorporated into the final crystal and did not require the "twice scanning" technique. This understanding of thermodynamic phase diagrams, the methods for pressurizing the furnace, as well as the use of a flux could be extended to the growth of other atmospherically sensitive materials. The techniques developed could even be extended to systems where oxidation (rather than reduction) is to be prevented.

The availability of large, high quality, pure single crystals has allowed for the comparison of synthetic (pure) to mineralogical (impure) hematite. For example, this work has shown that following argon ion bombardment crystals containing impurity species have a near-surface spinel phase and pure crystals do not. This impurity stabilized near-surface phase is stable over a much broader range of conditions than has been observed in the literature for a simple Fe_3O_4 termination (reconstruction) of hematite. Following high temperature annealing in oxygen-rich environments, all samples invariant of their purity show (1x1) diffraction spots indicative of a bulk-terminated surface. However, differences in the samples manifest after annealing in oxygen poor ($1x10^{-6}$ Torr) conditions. Samples which contain impurity species appear to be "locked" in a reduced state where the Fe_3O_4 surface phase persists even after annealing in conditions where the so-called "biphase" structure should be observed. Because an interesting result was obtained for hematite, the effect of impurity species on other oxides should be investigated. For example, it is common to dope $SrTiO_3$ with Nb to enhance conductivity for STM studies. Are the results obtained for doped crystals, with their associated dopant-induced defects (Rahmati et al., 2005), valid for those obtained on pure crystals? Also, the possibility of adatom-induced reconstructions similar to those seen in the Au/Si (Marks and Plass, 1995; Plass and Marks, 1995), In/Si (Collazo-Davila et al., 1997), and Ag/Ge (Collazo-Davila et al, 1998) systems must be considered whenever a foreign species is introduced.

An open question in the surface science community is the applicability of comparing experiments performed on TEM-ready samples to those performed on samples prepared using traditional surface science techniques. For example, in order to reproduce TEM results on a surface science sample, is a specific type (energy, time, angle of incidence) of ion milling required? Is the miscut inherent in a TEM sample necessary to observe a particular structure or morphology? Additionally, it is unknown whether the reverse is true: can experiments performed on a surface science sample (little or no miscut) be performed directly on TEM-ready (inherently stepped) samples? The present work has begun to address these questions. We have found in order to reproduce observed surface science results for the biphase structure of α-$Fe_3O_3(0001)$, TEM-ready hematite samples must be given a preanneal in oxygen-rich conditions in order to at least partially restore the surface stoichiometry, otherwise they remain locked in a reduced state. The biphase structure can not be reached from an already reduced state. Does this imply that it (the biphase) is not an equilibrium structure or that the kinetics are slow for the given annealing conditions? Answering these questions would be useful in understanding that very interesting and complicated structure.

Further investigation is needed to qualify the differences between TEM and surface science milling techniques and the effect they have on final surface composition. For example, it would be useful to understand the full extent of the nonstoichiometry, disorder, and reduction. An interesting experiment would compare the annealing behavior of samples which are thinned via argon ion bombardment

to those thinned using chemical etchants or tripod polishing which is a method of thinning that preserves surface stoichiometry. In fact, there is already a body of work for comparison on the (111) surface of $SrTiO_3$ where samples have been annealed in 200 mTorr of oxygen at 850 °C for 1 - 60 min following chemical etching with a 3:1 mixture of HCl:HNO_3 (Doan et al., 2001). Etching and annealing under these conditions appears to be a way of achieving bulk-terminated surfaces, which have never been observed in the current study.

As far as addressing the influence of sample miscut, it has been shown recently by the author and others (Greene et al., 2005) that very flat (RMS roughness of 0.4 Å) and well oriented hematite surfaces show a very interesting "swiss cheese-like" morphology that has not been observed on any other type of hematite sample. Is this an effect of the thermal history, preparation conditions, etc. or is it simply a function of the sample miscut and roughness? The answer to this question will help in determining the validity of comparing TEM to surface science experiments.

This work has also provided insight into the nature of the polar (111) surface of $SrTiO_3$, a prototypical example of an oxide with perovskite structure. Several new surface reconstructions with (3x3), (4x4), (6x6), and ($\frac{9}{5}$x$\frac{9}{5}$) unit cells have been discovered. The 2-dimensional (stand alone) structure of the (3x3) surface consists of a regular tiling of titanium surrounded by 3-fold symmetric oxygen arranged in a pattern of self-similar space filling triangles similar to the fractal known as Sierpinski's gasket. In three dimensions, when bonding to the bulk is considered, it becomes obvious that the structural units of the (3x3) surface are

actually tetrahedrally coordinated titanium viewed on end, as they are each bonded to a single oxygen in the layer below. In contrast to reconstructions observed on the (001) surface (Erdman et al., 2002, 2003), it appears that the octahedral units do not remain in fact to simply move as cohesive units upon reconstruction. The (3x3) surface is oxygen terminated, and titanium in the surface layer are 4-coordinate with an oxidation state of +3.44 from valence charge analysis. The (3x3) surface is always observed concurrently with the ($\frac{9}{5}$x$\frac{9}{5}$), and each can alternatively be indexed as (5x5) and (3x3) reconstructons of nonstoichiometric rock-salt-like TiO_y, respectively. This complicated relationship is explained on the basis of a commensurate interface between the perovskite $SrTiO_3$ (111) surface and the rock salt TiO_y (111) surface. In other words, the $SrTiO_3$-(3x3) reconstruction is the commensurate interface between $SrTiO_3$(111) and TiO_y(111). While the $SrTiO_3$-(3x3) reconstruction is readily observed in a dark field image, the TiO_y-(3x3) is not. This is interpreted to mean that the TiO_y exists over small areas and may be concentrated at step edges or other defect sites. The exact relationship between these two phases is unknown at this point. Although the commensurate interface argument presented here makes sense based on the experimental observations, the possibility that the (3x3) and $\frac{9}{5}$x$\frac{9}{5}$ phases coexist on the sample as a means to lower the surface free energy and are stabilized by the long range interactions of domain boundaries can not be ruled out. An interesting experiment to help answer this question would probe the fractional coverage of the ($\frac{9}{5}$x$\frac{9}{5}$) phase (via diffraction spot intensity) as a function of temperature and oxygen pressure.

There is no structure solution for the $\frac{9}{5}$x$\frac{9}{5}$ phase. The spots are faint and intensity measurement results in large errors. Furthermore, when symmetry averaged there are only 3 independent reflections. These two facts mean that this structure is not able to be solved by Direct Methods and must be determined some other way, for example by atomic resolution STM.

The spots consistent with a TiO_y phase are present in all of the diffraction patterns observed on the (111) surface of $SrTiO_3$ in this study. In fact, we propose that all of the structures observed can be thought of alternatively as reconstructions of TiO_y and are scaleable structures similar to the Si(111)-(7x7) DAS structure. Larger or smaller unit cells can be accommodated by adding or removing truncated octopolar units (in 2-dimensions) in a regular way.

Thermodynamics and kinetics on $SrTiO_3$(111) have been investigated by probing the surface structure as a function of annealing time, temperature, and oxygen partial pressure. It was determined that the (6x6) is a metastable structure that transforms upon reduction to the (3x3) structure. This reduction is diffusion rate controlled (proportional to temperature) and presumably occurs by the loss of oxygen from the surface. In order to verify this hypothesis, the atomic structure of the (6x6) phase needs to be determined in order to fully understand how it might transform to the (3x3). This is currently underway.

A metastable surface phase diagram has been constructed for a 5 h anneal, and areas of phase stability as well as coexistence have been narrowly determined. Images of the coexisting domains have been obtained and following annealing for

5 h, they are approximately 50 nm in size. If the same kinds of studies could be performed on a system in equilibrium where a true thermodynamic surface phase diagram could be constructed, several interesting fundamental thermodynamic parameters could be relatively easily backed out (see Appendix A for a worked example of the (6x6) to (3x3) transition).

The current work shows the $SrTiO_3(111)$ surface is not in equilibrium even following annealing at close to 1/2 the melting temperature for 5 h. The metastable state has many of the same properties that have previously been attributed to only thermodynamically equilibrated surfaces, such as faceting of the sample surface, microfaceting of the sample edge, air stability for months, as well as high reproducibility. The present work shows that while these factors are strong indicators of a thermally restored surface, they can not be taken as proof of a thermodynamically equilibrated surface. To determine whether surface structures are equilibrium structures, the phase boundary must be able to be *reversibly* crossed from *both* high and low values of temperature and oxygen partial pressure.

In terms of understanding the (if any) heterogeneous catalysis that occurs in this system, the important metric is the local atomic arrangement that any reactant molecule would see upon interaction with the surface. For the (3x3) structure, this local structure or molecular unit is the titanium tetrahedron (Figure 4.13). In the full 3-dimensional structure solution, 13 of these tetrahedra are corner sharing and sit with the 3-fold symmetric oxygen in the plane of the surface and a directional Ti-O bond normal to the surface. Three more are corner sharing but are rotated

approximately 90° and sit in the plane of the surface. The remaining 2 are slightly tilted edge-sharing tetrahedra.

One of the most important contributions this study has made to the understanding of heterogeneous catalysis is that we have shown for even simple systems, oxide surfaces are complex chemical entities unto themselves and behave in ways that could have never been imagined prior to this work and others like it.

References

Adachi, Y., Kohiki, S., Wagatsuma, K., and Oku, M. (1999) Changes in the chemical state of monocrystalline $SrTiO_3$ surface by argon ion bombardment. Applied Surface Science, 143, 272-276.

Agrawal, V., Chandrasekhar, N., Zhang, Y.J., Achutharaman, V.S., Mecartney, M.L., and Goldman, A.M. (1992) Nucleation and growth of $DyBa_2Cu_3O_{7x}$ thin films on $SrTiO_3$ substrates studied by transmission electron microscopy and atomic force microscopy. Journal of Vacuum Science and Technology A, 10(5), 1531-1536.

Ahdjoudj, J., Martinsky, C., Minot, C., Van Hove, M.A., and Somorjai, G.A. (1999) Theoretical Study of the termination of the $Fe_3O_4(111)$ surface. Surface Science, 443, 133-153.

Asthagiri, A., Niederberger, C., Francis, A.J., Porter, L.M., Salvador, P.A., and Shool, D.S. (2003) Thin Pt films on the polar $SrTiO_3(111)$ surface: An experimental and theoretical study. Suface Science, 537, 134-152.

Balbashov, A.M., and Egorov, S.K. (1981) Apparatus for growth of single crystals of oxide compounds by floating zone melting with radiation heating. Journal of Crystal Growth, 52, 498-504.

Balbashov, A.M., Lebedev, A.Y., Pavlova, S.G., and Bakhteuzov, V.E. (1985) Crystal growth nad the properties of α-Fe_2O_3 single crystal. Acta Physica Polonica, A68(3), 457-66.

Bandera, J., Tannakone, K., and Kiwi, J. (2001) Surface mechanism of molecular recognition between aminophenols and iron oxide surfaces. Langmuir, 17, 3964-3969.

Barbieri, A., Weiss, W., Van Hove, M.A., and Somorjai, G.A. (1994) Magnetite Fe_3O_4 (111): Surface structure by LEED crystallography and energetics. Surface Science, 302, 259-279.

Barks, R.E., and Roy, D.M. (1967) Single crystal growth of R_2O_3 (Corundum Structure) oxides by the flux method. Journal of Physics and Chemistry of Solids, Suppliment 1, 497-504.

Bengu, E., Plass, R., Marks, L.D., Ichihashi, T., Ajayan, P.M., and Iijima, S. (1996) Imaging the dimers on Si(111)-7x7. Physical Review Letters, 77(20), 4226-4228.

Berthon, J., Revcolevschi, A., Morikawa, H., and Touzelin, B. (1979) Growth of wustite($Fe_{1-x}O$) crystals of various stoichiometries. Journal of Crystal Growth, 47, 736-738.

Boyes, E.D., and Gai, P.L. (1997) Environmental high resolution electron microscopy and applications to chemical science. Ultramicroscopy, 67(4), 219.

Bozso, F., Ertl, G., and Weiss, M. (1977) Interaction of nitrogen with iron surfaces II: Fe(110). Journal of Catalysis, 50(3), 519-529.

Brewer, L. (1953) The thermodynamic properties of the oxides and their vaporization processes. Chemical Reviews, 52, 1-75.

Brundle, C.R., Chuang, T.J., and Wandelt, K. (1977) Core and valence level photoemission studies of iron oxide surfaces and the oxidation of iron. Surface Science, 68, 459-468.

Buckett, M. (1991) Electron Radiation Damage in Transition Metal Oxides. Materials Science and Engineering. Northwestern University, Evanston.

Carrasco, J., Illas, F., Kotomin, E.A., Zhukovskii, Y.Z., Piskunov, S., Maier, J., and Hermansson, K. (2005) First principles simulations of F centers in cubic $SrTiO_3$. Phys. Stat. Sol., 2(1), 153-158.

Cherns, D. (1974) Direct resolution of surface atomic steps by transmission electron microscopy. Philosophical Magazine, 30, 549-556.

Chiaramonti, A.N., Pless, J.D., Lui, L., Smit, J.P., Lanier, C.H., Poeppelmeier, K.R., Stair, P.C., and Marks, L.D. (2004) Growth of single crystal α-Fe_2O_3 from a $CaFe_4O_7$-based solvent. Journal of Crystal Growth and Design, 4(4), 749-753.

Chuang, T.J., Brundle, C.R., and Wandelt, K. (1978) An X-ray photoelectron spectroscopy study of the chemical changes in oxide and hydroxide surfaces induced by Ar+ ion bombardment. Thin Solid Films, 53, 19-27.

Collazo-Davila, C., Landree, E., Grozea, D., Jayaram, G., Plass, R., Stair, P.C., and Marks, L.D. (1995) Design and initial performance of an ultrahigh vacuum sample preparation evaluation analysis and reaction (SPEAR) system. Journal of the Microscopy Society of America, 1(6), 267-279.

Collazo-Davila, C., Marks, L.D., Nishii, K., and Tanishiro, Y. (1997) Atomic structure of the In on Si(111) (4x1) surface. Surface Review and Letters, 4(1), 65-70.

Collazo-Davila, C., Grozea, D., Marks, L.D., Feidenhans'l, R., Nielsen, M., Seehofer, L., Lottermoser, L., Falkenberg, G., Johnson, R.L., Göthelid, M., Karlsson, U. (1998) Solution of Ge(111)-(4x4)-Ag structure using direct methods applied to X-ray diffraction data. Surface Science, 418, 395-406.

Condon, N.G., Murray, P.W., Leibsle, F.M., Thornton, G., Lennie, A.R., and Vaughan, D.J. (1994) Fe_3O_4(111) termination of α-Fe_2O_3(0001). Surface Science, 310, L609-L613.

Condon, N.G., Leibsle, F.M., Lennie, A.R., Murray, P.W., Vaughan, D.J., and Thornton, G. (1995) Biphase ordering of iron oxides. Physical Review Letters, 75(10), 1961-1964.

Condon, N.G., Leibsle, F.M., Parker, T., Lennie, A.R.V., D.J., and Thornton, G. (1997) Biphase ordering on Fe_3O_4 (111). Physical Review B, 55(23), 15885-15894.

Cowley, J.M. (1986) Electron microscopy of surface structure. Progress in Surface Science, 21(3), 209-250.

Doan, T-.D., Giocondi, J.L., Rohrer, G.S., Salvador, P.A. (2001) Surface engineering along the close-packed direction of $SrTiO_3$. Journal of Crystal Growth, 225, 178-182.

Edington, J.W. (1974) Electron Diffraction in the Electron Microscope. The Macmillan Press, LTD., London.

Elwell, D., and Scheel, H.J. (1975) Crystal Growth from High Temperature Solutions. Academic Press, New York.

Erdman, N. (2002) Structure, morphology, and chemistry of catalytic transition metal oxides. Materials Science and Engineering, p. 132. Northwestern University, Evanston.

Erdman, N., Poeppelmeier, K.R., Asta, M., Warschkow, O., Ellis, D.E., and Marks, L.D. (2002) The structure and chemisty of the TiO_2-rich surface of $SrTiO_3$(001). Nature (419), 55-58.

Erdman, N., Warschkow, O., Asta, M., Poeppelmeier, K.R., Ellis, D.E., and Marks, L.D. (2003) Surface structures of $SrTiO_3$(001): a TiO_2-rich reconstruction with a c(4x2) unit cell. Journal of the American Chemical Society, 125(33), 10050-10056.

Ewald, P.P. (1921) Die Berechnung optischer und elektrostatischer Gitterpotentiale. Annals of Physics (Leipzig), 64, 253-287.

Flanders, P.J., and Remeika, J.P. (1965) Magnetic properties of hematite single crystals. Philosophical Magazine, 11, 1271-1288.

Garton, G., Smith, S.H., and Wanklyn, B.M. (1972) Crystal growth from the flux systems PbO-V_2O_5 and Bi_2O_3-V_2O_5. Journal of Crystal Growth, 13/14, 588-592.

Garvie, L.A.J., and Buseck, P.R. (1998) Ratios of ferrous to ferric iron from nanometre-sized areas in minerals. Nature, 396, 667-670.

Gaskell, D.R. (1995) Introduction to the Thermodynamics of Materials. Taylor and Francis, Washington, D.C.

Gennari, F.C., and Pasquevich, D.M. (1996) Crystal growth of α-Fe_2O_3 in chlorine atmosphere. Journal of Materials Science Letters, 15, 1847-1850.

Giacovazzo, C. (1998) Direct Phasing in Crystallography: Fundamentals and Applications. Oxford Unversity Press, New York.

Gömann, A., Gömann, K., Frerichs, M., Kempter, V., Borchardt, G., and Maus-Friedrichs, W. (2005) Electronic structure and topography of annealed $SrTiO_3$(111) surfaces studied with MEIS and STM. Surface and Interface Analysis, submitted.

Greene, M.E., Chiaramonti, A.N., Christensen, S.T., Cao, L.X., Bedzyk, M.J., and Hersam, M.C. (2005) Controlled nanoscale morphology of hematite (0001) surfaces grown by chemical vapor transport. Advanced Materials, in press.

Grozea, D., Landree, E., Marks, L.D., Feidenhans'l, R., Nielsen, M., and Johnson, R.L. (1998) Direct methods determination of the Si(111)-(6x6)Au surface structure. Surface Science, 418, 32-45.

Haider, M., Uhlemann, S., Schwan, E., Rose, H., Kabius, B., and Urban, K. (1998) Electron microscopy image enhanced. Nature, 392(6678), 768-769.

Heizmann, J.J., Becker, P., and Baro, R. (1981) The influence of crystallite orientation on the chemical reactivity of hematite α-Fe_2O_3 and Magnetite Fe_3O_4. Journal of Applied Crystallography, 14, 270-273.

Henderson, M.A. (1999) A surface perspective on self-diffusion in rutile TiO_2. Surface Science, 419, 174-187.

Hillert, M., Selleby, M., and Sundman, B. (1990) An assesment of the Ca-Fe-O system. Metallurgical Transactions A, 21A(10), 2759-2776.

Hirsch, P., Howie, A., Nicholson, R., Pashley, D.W., and Whelan, M.J. (1977) Electron Microscopy of Thin Crystals. Krieger Publishing Co., Malabar.

Hochella, M., and White, A. (1990) Mineral-Water Interface Geochemistry. P.H. Ribbe, Ed. Reviews in Mineralogy, 23. Mineralogical Society of America, Washington, D.C.

Hurlbut, C.S. (1971) Dana's Manual of Mineralogy. Wiley and Sons, New York.

Jacobs, P., and Somorjai, G.A. (1998) Conversion of heterogeneous catalysis from art to science: The surface science of heterogeneous catalysis. Journal of Molecular Catalysis A: Chemical, 131, 5-18.

Jayaram, G., Plass, R., and Marks, L.D. (1995) UHV-HREM and diffraction of surfaces. Interface Science, 2, 379-395.

Joshi, S., Bilurkar, P.G., Chaudhari, S.M., Kanetkar, S.M., and Ogale, S.B. (1989) Medium-energy ion-beam-induced microstructural modifications in α-Fe_2O_3. Physical Review B, 40(15), 10635-10638.

Junta-Russo, J., and Hochella, M. (1996) The chemistry of hematite (001) surfaces. Geochimica et Cosmochimica Acta, 60(2), 305-314.

Ketteler, G., Weiss, W., and Ranke, W. (2001a) Surface structures of α-Fe_2O_3 (0001) phases determined by LEED crystallography. Surface Review and Letters, 8(6), 661-683.

Ketteler, G., Weiss, W., Ranke, W., and Schlogl, R. (2001b) Bulk and surface phases of iron oxides in an oxygen and water atmosphere at low pressure. Physical Chemistry Chemical Physics, 3, 1114-1122.

Kimura, S., and Shindo, I. (1977) Single crystal growth of YIG by the floating zone method. Journal of Crystal Growth, 41, 192-198.

Kimura, S., and Kitamura, K. (1992) Floating zone crystal growth and phase equilibria: A review. Journal of the American Ceramic Society, 75(6), 1440-1446.

Lad, R.J., and Henrich, V.E. (1988) Strucutre of α-Fe_2O_3 single crystal surfaces following Ar^+ ion bombardment and annealing in O_2. Surface Science, 193, 81-93.

Landree, E., Collazo-Davila, C., and Marks, L.D. (1997) Multi-solution genetic algorithm approach to surface structure determination using direct methods. Acta Crystallographica, B53, 916-922.

Lehmpfuhl, G., and Warble, C.E. (1986) Direct electrom microscopic imaging of surface topography by diffraction and phase contrast. Ultramicroscopy, 19, 135-146.

Lennie, A.R., Condon, N.G., Leibsle, F.M., Murray, P.W., Thornton, G., and Vaughan, D.J. (1996) Structures of Fe_3O_4 (111) surfaces observed by scanning tunneling microscopy. Physical Review B, 53(15), 10244-10253.

Lin, T.S. (1961) Remanent magnetization of a synthetic hematite single crystal. Journal of Applied Physics, 32(3), 394S-395S.

Liu, L., and Chiaramonti, A.N. (2004) Unpublished work.

Liu, L. (2005) Methyl radical chemistry on single crystal hematite surfaces and UO_3 supported on single crystal hematite. Chemistry, p. 179. Northwestern University, Evanston.

Lo, W.J., and Somorjai, G.A. (1978) Temperature dependent surface structure, composition and electronic properties of the clean $SrTiO_3$(111) surface: Low energy electron diffraction, Auger-electron spectroscopy, electron energy loss, and ultraviolet -photoelectron spectroscopy studies. Physical Review B, 17(12), 4942-4950.

Lu, P., and Smith, D.J. (1991) Direct imaging of CdTe(001) surface reconstructions by high resolution electron microscopy. Surface Science, 254, 119-124.

Marks, L.D. (1983) Direct imaging of carbon-covered and clean gold (110) surfaces. Physical Review Letters, 51, 1000-1002.

Marks, L.D., and Smith, D.J. (1983) Direct surface imaging in small metal particles. Nature, 303, 316-317.

Marks, L.D. (1984) Direct imaging of solid surfaces. I. Image simulation and interpretation. Surface Science, 139(1), 281-298.

Marks, L.D., Xu, P., Dunn, D.N., and Zhang, J.P. (1992) Atomic imaging of surfaces in plan view. Electron Microscopy Society of America, 22(3), 65-69.

Marks, L.D., and Plass, R. (1995) Atomic structure of Si(111)-(5x2)-Au from high resolution electron microscopy and heavy-atom holography. Physical Review Letters, 75(11), 2172-2175.

Marks, L.D., Bengu, E., Collazo-Davila, C., Grozea, D., Landree, E., Leslie, C., and Sinkler, W. (1998) Direct methods for surfaces. Surface Review and Letters, 5(5), 1087-1106.

Marks, L.D. (2004). Private communication.

-. (2005). Private communication.

Maurice, P., Hochella, M., Parks, G.A., Sposito, G., and Schwertmann, U. (1995) Evolution of hematite surface microtopgraphy upon dissolution by simple organic acids. Clays and Clay Minerals, 43(1), 29-38.

Millon, E., Malaman, B., Bonazebi, A., Brice, J.F., Gerardin, R., and Evrard, O. (1986) Structure crystalline du ferrite hemicalcique $CaFe_4O_7$. Material Research Society Bulletin., 21, 985-994.

Mishima, T., and Osaka, T. (1998) Profile imaging of the InSb{111}A,B-(2x2) surfaces. Surface Science, 395, L256-L260.

Misono, M., and Mizuno, N. (1997) Design of catalysts based on perovskite-type mixed oxides. Ceramic Transactions, 73, 67-83.

Muan, A., and Osborn, E.F. (1965) Phase Equilibria Among Oxides in Steelmaking. Addison-Wesley, Reading.

Nishino, D., Nakafuji, A., Yang, J., and Shindo, D. (1998) Precise morphology analysis of platelet type hematite particles by transmission electron microscopy. ISIJ, 1369-1373.

Noguera, C. (2000) Polar oxide surfaces. Journal of Physics: Condensed Matter, 12, R367-R410.

Oka, K., Shibata, H., and Kashiwaya, S. (2002) Crystal Growth of ZnO. Journal of Crystal Growth, 237-239, 509-513.

Park, B.H., and Kim, D.S. (1999) Coupled Substitution of NiO and TiO_2 in Hematite. Bulletin of the Korean Chemical Society, 20(2), 195-198.

Payling, R. (2003) The ICP Laboratory. http://icp-oes.com. Accessed April, 2005.

Pfann, W.G. (1966) Zone Melting. 310 p. John Wiley and Sons, Inc., New York.

Phillips, B., and Arnulf, M. (1958) Phase equilibria in the system CaO-iron oxide in air and at 1 atm. O_2 pressure. Journal of the American Ceramic Society, 41(11), 445-454.

Phillips, B., and Muan, A. (1960) Stability relations of iron oxides: Phase equilibria in the system Fe_3O_4-Fe_2O_3 at oxygen pressures up to 45 atmospheres. Journal of Physical Chemistry, 64.

Plass, R. and Marks, L.D. (1995) UHV transmission electron microscopy structure determination of the Si(111)-($\sqrt{3}$x$\sqrt{3}$)R30° Au surface. Surface Science, 342, 233-249.

Pless, J., Erdman, N., Ko, D., Marks, L., Stair, P., and Poeppelmeier, K. (2003) Single-crystal growth of magnesium orthovanadate, $Mg_3(VO_4)_2$, by the optical floating zone technique. Journal of Crystal Growth and Design, 3(4), 615-619.

Pojani, A., Finocchi, F., and Noguera, C. (1999) Polarity on the $SrTiO_3$ (111) and (110) surfaces. Surface Science, 442, 179-198.

Rahmati, B., Fleig, J., Sigle, W., Bischoff, E., Maier, J., and Rühle, M. (2005) Oxidation behavior of reduced polycrystalline Nb-doped $SrTiO_3$. Surface Science, submitted.

Reed, T.B. (1971) Free Energy of Formation of Binary Compounds. An Atlas of Charts for High-Temperature Chemical Calculations. MIT Press, Cambridge.

Revcolevschi, A., and Jegoudez, J. (1997) Growth of large high-T_c single crystals by the floating zone method: A review. Progress in Materials Science, 42, 321-339.

Ritter, M., and Weiss, W. (1999) Fe_3O_4(111) surface structure determined by LEED crystallography. Surface Science, 432, 81-94.

Rudd, D.F., Fathi-Afshar, S., Trevino, A.A., and Stadtherr, M.A. (1981) Petrochemical Technology Assesment. Wiley, New York.

Sadykov, V.A., Isupova, L.A., Zolotarskii, I.A., Bobrova, L.N., Noskov, A.S., Parmon, V.N., Brushtein, E.A., Telyatnikova, T.V., Chernyshev, V.I., and Lunun, V.V. (2000) Oxide catalysts for ammonia oxidation in nitric acid production: Properties and perspectives. Applied Catalysis A, 201, 59-87.

Sahu, K.K., Rath, C., Mishra, N.C., Anand, S., and Das, R.P. (1997) Microstructural and magnetic studies on hydrothermally prepared hematite. Journal of Colloid and Interface Science, 185, 402-410.

Sanchez, C., Hendewerk, M., Sieber, K.D., and Somorjai, G.A. (1986) Synthesis, bulk, and surface characterization of niobium-doped Fe_2O_3 single crystals. Journal of Solid State Chemistry, 61, 47-55.

Sekiguchi, S., Fujimoto, M., Kang, M., Koizumi, S., Cho, S., and Tanaka, J. (1998a) Structure analysis of $SrTiO_3$ (111) polar surfaces. Japanese Journal of Applied Physics, 37, 4140-4143.

Sekiguchi, S., Fujimoto, M., Nomura, M., Cho, S., Tanaka, J., Nishihara, T., Kang, M., and Hyoung-Ho, P. (1998b) Atomic force microscopic observation of $SrTiO_3$ polar surface. Solid State Ionics, 108, 73-79.

Shaikhutdinov, S.K., and Weiss, W. (1999) Oxygen pressure dependence of the α-Fe_2O_3 (0001) surface structure. Surface Science, 432, L627-634.

Shannon, R.D. (1976) Revised effective ionic radii and systematic studies of interatomic distances in halides and chalcogenides. Acta Crystallographica, A32, 751-767.

Sharma, R. (2001) Design and applications of environmental cell transmission electron microscope for in situ observations of gas-solid reactions. Microscopy and Microanalysis, 7, 494-506.

Shibuya, K., Ohnishi, T., Lippmaa, M., Kawasaki, M., and Koinuma, H. (2004) Single crystal $SrTiO_3$ field-effect transistor with an atomically flat amorphous $CaHfO_3$ gate insulator. Applied Physics Letters, 85(3), 425-427.

Sigmund, W.M., Rotov, M., Jiang, Q.D., Brunen, J., Zegenhagen, J., and Aldinger, F. (1997) A titanium-rich (111) surface of $StRiO_3$ single crystals by thermal annealing. Applied Physics A, 64, 219-220.

Sorescu, M., Brand, R.A., Mihaila, D., and Diamandescu, L. (1999) The crucial role of particle morphology in the magnetic properties of haematite. Journal of Applied Physics, 85(8), 5546-5548.

Subramanian, A., and Marks, L.D. (2004a) Surface crystallography via electron microscopy. Ultramicroscopy, 98, 151-157.

-. (2004b) Direct observation of charge transfer at a MgO(111) surface. Physical Review Letters, 92, 26101.

Subramanian, A. (2005) Transmission electron microscopy studies of surface phenomena in polar oxides. Materials Science and Engineering, p. 113. Northwestern University, Evanston.

Takayanagi, K., Tanishiro, Y., Takahashi, M., and Takahashi, S. (1985a) Structural analysis of silicon(111)-7x7 by UHV-transmission electron diffraction and microscopy. Journal of Vacuum Science and Technology A, 3(3, part 2), 1502-1506.

Takayanagi, K., Tanishiro, Y., Takahshi, S., and Takahashi, M. (1985b) Structure analysis of silicon(111)-7x7 reconstructed surface by transmission electron diffraction. Surface Science, 164(2-3), 367-392.

Takekawa, S., and Nozaki, H. (1988) Single crystal growth of the superconductor $Bi_{2.0}(Bi_{0.2}Sr_{1.8}Ca_{1.0})Cu_{2.0}O_8$. Journal of Crystal Growth, 92, 687-690.

Tanaka, H., and Kawai, T. (1996) Surface structure of reduced $SrTiO_3(111)$ observed by scanning tunneling microscopy. Surface Science, 365, 437-442.

Tasaki, A., and Iida, S. (1963) Magnetic properties of synthetic single crystal of α-Fe_2O_3. Journal of the Physical Society of Japan, 18(8), 1148-1154.

Toledano, D.S., and Henrich, V.E. (2001) Kinetics of SO_2 adsorption on photoexcited α-Fe_2O_3. Physical Chemistry B, 105(18), 3872-3877.

Venables, J., Smith, D.J., and Cowley, J.M. (1987) HREM, STEM, REM, SEM - and STM. Surface Science, 181, 235-249.

Wang, X.G., Weiss, W., Shaikhutdinov, S.K., Ritter, M., Peterson, M., Wagner, F., Schlogl, R., and Scheffler, M. (1998) The hematite (α-Fe_2O_3) (0001) surface: Evidence for domains of distinct chemistry. Physical Review Letters, 81(5), 1038-1041.

Wang, Y.M. (2005). Unpublished work.

Wanklyn, B.M. (1970) Two new flux systems, PbO-V_2O_5 and Bi_2O_3-V_2O_5. Journal of Crystal Growth, 7, 368-370.

Warschkow, O., Ellis, D., Hwang, J., Mansourian-Hadavi, N., and Mason, T.O. (2002) Defects and charge transport near the hematite (0001) surface: An atomistic study of oxygen vacancies. Journal of the American Ceramic Society, 85(1), 213-220.

Warschkow, O. (2003). Private communication.

Williams, D.B., and Carter, C.B. (1996) Transmission Electron Microscopy: A Textbook for Materials Science. Plenum Press, New York.

Xu, P., and Marks, L.D. (1992) Intensities of surface diffraction spots in plan view. Ultramicroscopy, 45, 155-157.

Xu, P., Dunn, D., Zhang, J.P., and Marks, L.D. (1993) Atomic imaging of surfaces in plan view. Surface Science Letters, 285, L479-L485.

Xu, P., Jayaram, G., and Marks, L.D. (1994) Cross-correlation method for intensity measurement of transmission electron diffraction patterns. Ultramicroscopy, 53, 15-18.

Yagi, K., Takayanagi, K., Kobayashi, K., Osakabe, N., Tanishiro, Y., and Honjo, G. (1979) Surface study by an UHV electron microscope. Surface Science, 86, 174-181.

Zhang, J.P. (1989) Unpublished work.

Zhao, Y.F., Yang, H.Q., Gao, J.N., Xue, Z.Q., and Pang, S.J. (1998) Local dimer-adatom stacking fault structures from 3x3 to 13x13 along Si(111)-7x7 domain boundaries. Physical Review B, 58(20), 13824-13829.

Zhao, Y.F., Zhang, Z.H., Yang, H.Q., Xue, Z.Q., and Pang, S.J. (2000) Structure analysis of Si(111)-7x7 domain boundaries with Takayanagi cores. Journal of Vacuum Science and Technology A, 18(2), 320-324.

Zhou, W., Xin, Y., and Jefferson, D.A. (2000) HRTEM surface profile imaging of superconducting $YBa_2Cu_4O_8$. Journal of Solid State Chemistry, 149(2), 327-332.

Zurbuchen, M.A., Lettieri, J., Jia, Y., Schlom, D.G., Streiffer, S.K., and Hawley, M.E. (2001) Transmission electron microscopy study of the (103)-oriented epitaxial $SrBi_2Nb_2O_9$ films grown on (111) $SrTiO_3$ and (111) $SrRuO_3$/(111) $SrTiO_3$. Journal of Materials Research, 16(2), 489-502.

APPENDIX A

Experimental Determination of Fundamental Thermodynamic Parameters for Surfaces

A plot of $\log(pO_2)$ versus (1/T) for the phase transition would yield a straight line whose equation would give the standard Gibbs free energy change of the reaction (ΔG°) as well as the standard enthalpy and entropy changes. Such a plot has been created for the *metastable* equilibrium observed on $SrTiO_3(111)$ after 5 h annealing and is shown in Figure A.1. The experimental data lie on a straight line ($R^2 = 0.9983$) whose equation is given by:

$$\log p_{O2} = -\frac{4699.6}{T} + 3.3135$$

From Gaskell (1995)

$$\ln p_{O2} = \frac{\Delta G^\circ}{RT}$$

therefore

$$\begin{aligned} \Delta G^\circ_{6x6\rightarrow 3x3} &= 2.303RT\left[-\frac{4699.6}{T} + 3.3135\right] \\ &= -89,983 + 63T\ (J) \end{aligned}$$

Assuming for simplification $\Delta c_p = 0$ (a good approximation when no change in state occurs). Then,

$$\begin{aligned} \Delta G^\circ &= \Delta H^\circ - T\Delta S^\circ \\ \Delta S^\circ &= -63\ J(mol)^{-1} \\ \Delta H^\circ &= -89,983\ J(mol)^{-1} \end{aligned}$$

This means at room temperature, $\Delta G^\circ_{298} = -71\ kJ$ and at the reaction temperature, ΔG°_{1323}=-7 kJ. Note that the actual values are meaningless because the reaction is not in equilibrium but the exercise above serves two purposes: (1) demonstrate how to extrapolate fundamental thermodynamic information from surfaces experimentally and (2) gives a rough estimate (on the order) of the true value of the standard entropy change ΔS° for a phase transition on an oxide surface.

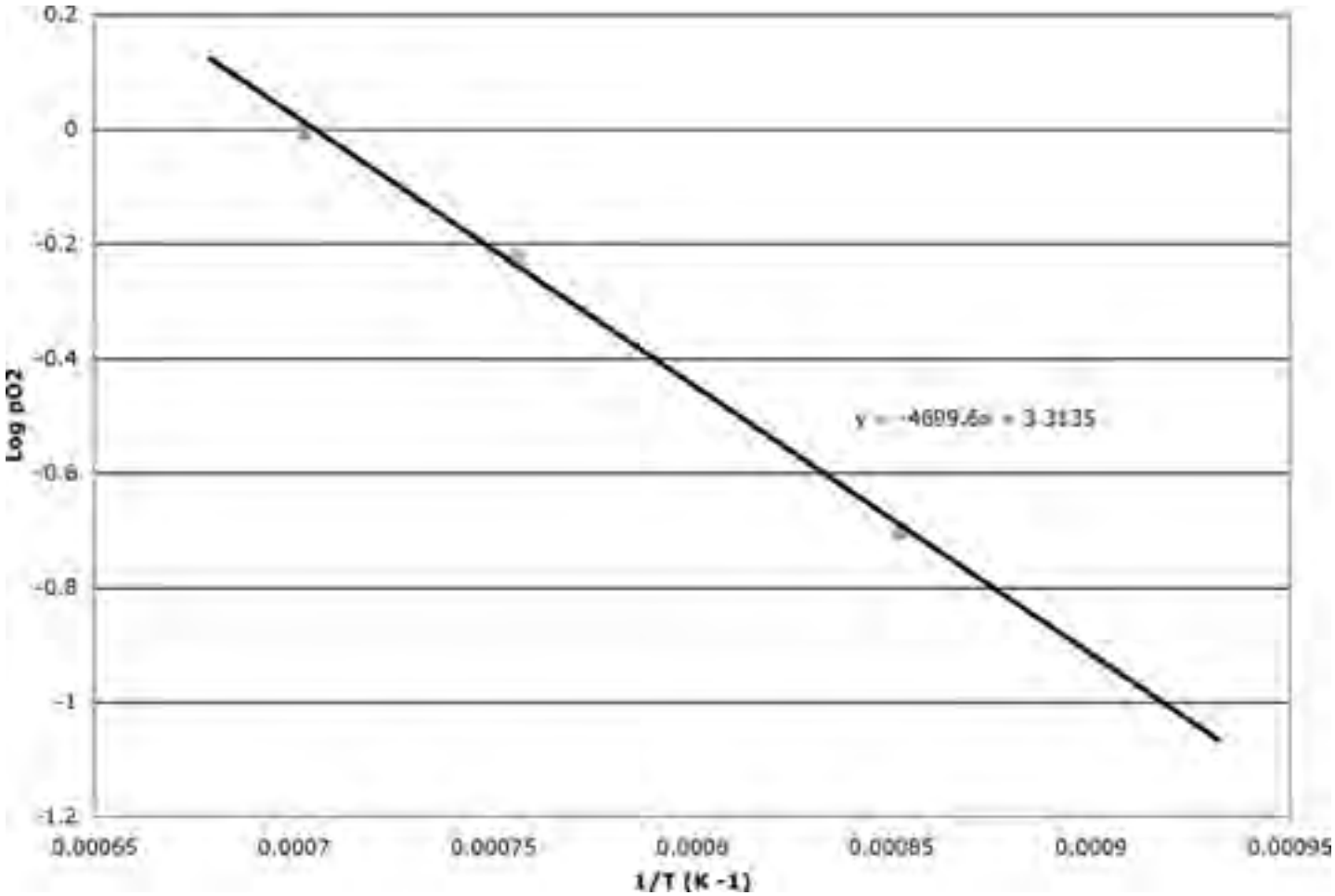

Figure A.1. Plot of Log pO_2 versus (1/T) for the metastable phase transition (6x6) $\rightarrow$ (3x3). A plot of this type for an equilibrium surface phase transition can yield experimentally determined values of $\Delta G^\circ, \Delta H^\circ$ and ΔS° for a surface phase transition.

APPENDIX B

Truncated Octahedral, Truncated Octopolar, and Tetrahedral Units in Projection

Whenever a reconstruction of $SrTiO_3$ is discussed in this text, the archetype motif of a titanium atom surrounded by three oxygen is referred to as a truncated octahedral unit. Whenever a reconstruction of TiO_y is discussed, the same motif is referred to as an octopolar unit. I will show why even though their origins are very different, in the case of a 2-layer surface reconstruction (e.g. a single layer of Ti and a single layer of O) they look the same in projection. Further, I will show how a tetrahedrally coordinated central atom (such as the titanium in the full 3-dimensional (3x3) structure solution) can appear in projection to look similar to both a truncated octahedra and truncated octopolar unit, and is distinguished only by the bonding to the bulk layers underneath. This is why in the 2-dimensional (3x3) structure solution the structural motif is referred to as a truncated octahedra but the titanium atoms in the full 3-dimensional solution are actually 4-coordinate.

An octahedral unit is defined as a central atom coordinated to six others forming a polyhedron having eight faces, hence the name. $SrTiO_3$ has a central Ti octahedron in every unit cell (Figure B.1a). If this octahedral unit is viewed along

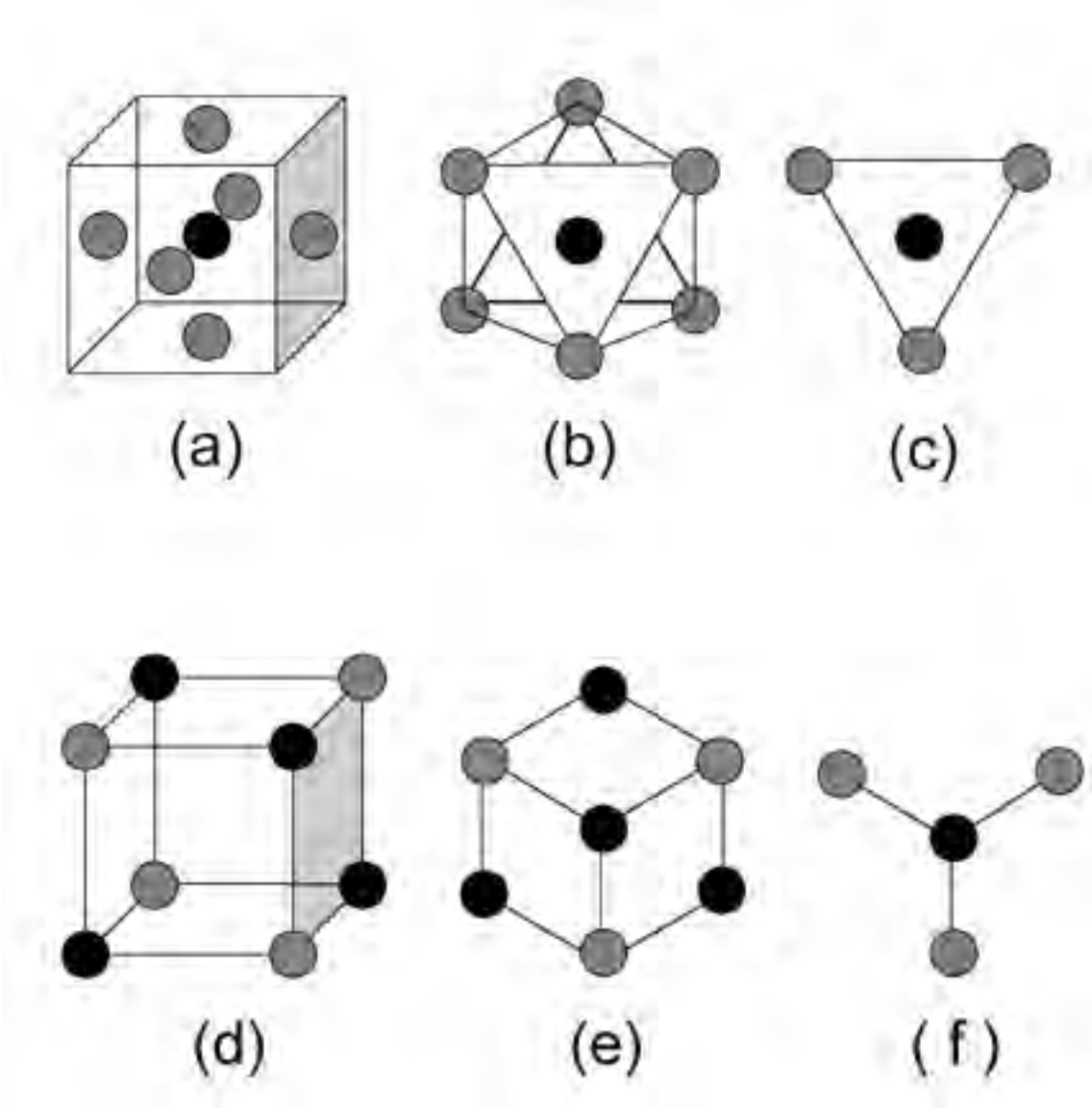

Figure B.1. Schematic diagram comparing truncated octahedra in $SrTiO_3(111)$ (a-c) to truncated octopolar units in $TiO_y(111)$ (d-f).

the close packed [111] direction in projection (Figure B.1b), it appears as a titanium surrounded by 6-fold symmetric oxygen. If one half of this octahedron is removed,

the resulting truncated octahedron appears as a central titanium surrounded by 3-fold symmetric oxygen (Figure B.1c). The Ti-O distance in projection for this structure is $\sqrt{6}$a/6, or 1.59 Å.

If a cube is populated with cubic close packed anions and a cation in every octahedral interstitial site, 8 octopolar units with side length a/2 are formed per unit cell, one of which is shown in Figure B.1d. Octopolar units are the structural motif in all rock salt oxides including NaCl, MgO, and TiO_y. If this TiO_y octopolar unit is viewed along the close packed [111] direction in projection, it appears as a central titanium surrounded by three oxygen with 3-fold symmetry, and 3 titanium in 3-fold symmetry (Figure B.1e). If the bottom half of this octopolar unit is removed, the resulting truncated octopolar unit appears as a central titanium atom surrounded by 3-fold symmetric oxygen (Figure B.1f). The Ti-O distance for this structure is $\sqrt{6}$a/6, or 1.75 Å.

A tetrahedron is a regular polygon composed of four vertices, six edges, and four equivalent equilateral triangular faces. A tetrahedrally coordinated central atom is an atom bonded to four ligands with bond angles of 109.5° (Figure B.2a). Tetrahedral units are the structural motif in most silicates and also a host of other oxide compounds, therefore the central atom will be referred to as the cation (titanium in this case) and the ligands will be referred to as the anions (oxygen in this case). When viewed along one of four equivalent oxygen-titanium directions (Figure B.2b), the structure appears as an oxygen atom surrounded by three others with 3-fold symmetry. Since directly underneath of this top oxygen atom is the

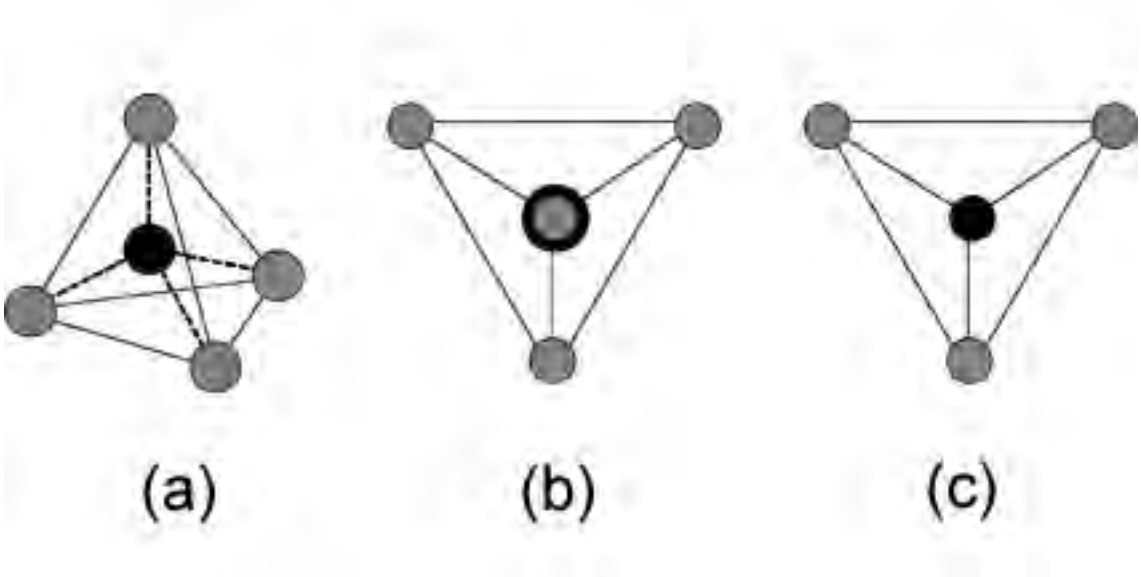

Figure B.2. Schematic diagram demonstrating how a tetrahedrally coordinated cation can appear similar to both a truncated octahedra and truncated octopolar unit in projection.

central titanium atom, truncating this tetrahedron results in the projected structure of a central titanium atom surrounded by 3-fold symmetric oxygen (Figure B.2c).